2008

Noninvasive acoustical image reconstruction of a static object through a simulated human skull bone

Kiyanoosh Shapoori
University of Windsor

Noninvasive Acoustical Image Reconstruction of a Static Object through a Simulated Human Skull Bone

By

Kiyanoosh Shapoori

A Thesis
Submitted to the Faculty of Graduate Studies
Through the Department of Physics
In Partial Fulfillment of the Requirements for
The Degree of Master of Science at the
University of Windsor

Windsor, Ontario, Canada
2008

Your file Votre référence
ISBN: 978-0-494-47071-8
Our file Notre référence
ISBN: 978-0-494-47071-8

Author's Declaration of Originality

I hereby certify that I am the sole author of this thesis and that no part of this thesis has been published or submitted for publication.

I certify that, to the best of my knowledge, my thesis does not infringe upon anyone's copyright nor violate any proprietary rights and that any ideas, techniques, quotations, or any other material from the work of other people included in my thesis, published or otherwise, are fully acknowledged in accordance with the standard referencing practices. Furthermore, to the extent that I have included copyrighted material that surpasses the bounds of fair dealing within the meaning of the Canada Copyright Act, I certify that I have obtained a written permission from the copyright owner(s) to include such material(s) in my thesis and have included copies of such copyright clearances to my appendix.

I declare that this is a true copy of my thesis, including any final revisions, as approved by my thesis committee and the Graduate Studies office, and that this thesis has not been submitted for a higher degree to any other University or Institution.

ABSTRACT

A new method for image reconstruction of a foreign object, i.e. any reflector which somehow could be inserted into the brain tissue, such as a bullet or a piece of shrapnel, is investigated. The method is based on noninvasive transcranial ultrasound propagation through skull bone and brain tissue. A simulation has been developed during the study to process the experimental results and reconstruct an image showing the position of the foreign object. The algorithm is designed for use with a linear array of 128 receivers and a source of ultrasound as the reflector (all at the optimized frequency of 1.7MHz). A simplified simulated skull bone (scattering medium) was also added to the program to distinguish how it affects passing through ultrasonic fields in different circumstances. From an experimental point of view, to check the effectiveness of the algorithm, a simplified skull bone phantom was made and used in data acquisition at the array of receivers. When passed through phantom layer, the ultrasound field (initially generated at the reflector) reaches the array of receivers, and after being saved, the distribution on the array is processed to compensate for the distortion and reconstruct an image which contains data about the reflector's position. Due to high attenuation in scattering medium (which represents skull bone's acoustical properties) and brain tissue, it has been determined that the method can reconstruct the reflector's position roughly at a maximum distance of 15cm from the array of receivers in presence of the phantom which is far enough to cover all inside of a typical skull.

To my wonderful wife

ACKNOWLEDGEMENTS

I want to express my sincere thanks to the people who gave me direct or indirect support during my graduate study and research at the University of Windsor.

My sincere appreciation first goes to Dr. Roman Maev for his constant and continued support which brought me the peace of mind to freely think, study and research. His guidance both with respect to the science behind this project and academic pursuit as a whole has been indispensable.

I would also like to thank Dr. Tatiana Kondratieva, who initiated the idea and kept me in the right direction during my first year. I would especially like to thank Dr. Fedar Seviaryn and Dr. Jeffrey Sadler for their great help with regards to theory and experiment.

Furthermore, the role of Dr. Chowdhury, Dr. Atkinson and Dr. Kim as my committee members is also greatly appreciated.

As well, I would like to thank Sarah Beneteau and Marie Jeannette for many times they have come to my aid.

This work was supported by ONR Grant No. N00014-06-30-0088 from Biocentric Technology Program. The role of the University of Windsor was also of great importance in conducting this study.

And finally, I would like to thank my wonderful wife and parents for their great support and inspiration.

TABLE OF CONTENTS

LIST OF TABLES

LIST OF FIGURES

Chapter1

INTRODUCTION

The ability to reconstruct ultrasonic images of internal brain structures (soft tissues and blood vessels) through the thick skull bone is without question very beneficial for biomedical purposes. The main obstacles that stand in the way of reliable ultrasonic imaging arise from strong destructive effects due to the thickness of skull bones.

The wave front distortion is primarily caused by the irregularity of the lower boundary of the skull bone; in other words, the lower bone boundary is not flat. The compound, multi layered structure of the skull bone also influences the acoustical field characteristics, leading to distortion. Further, the heterogeneity scales vary considerably between individuals, ranging from millimeters to centimeters (Fig.1.1). The inhomogeneities are for the most part smooth, save for a few small sections.

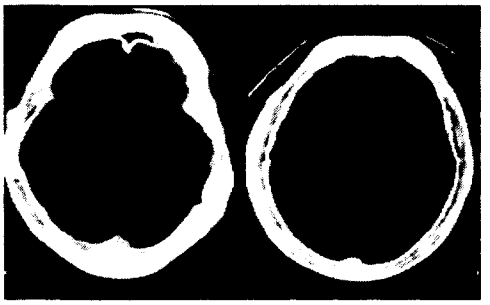

Fig.1.1 MRI transversal images of skull bone[1]

A side view of the acoustical field after propagation through the skull bone is presented in Fig1.2. These images were reconstructed by means of an optical shading method. The top image was recorded at a frequency of 700 kHz; the bottom image corresponded to a frequency of 2 MHz. As can be seen by comparing the first image with the second, the increase in frequency causes inhomogeneities within the skull bone to

have a more pronounced effect, causing the acoustical field to become distorted and unfocused.

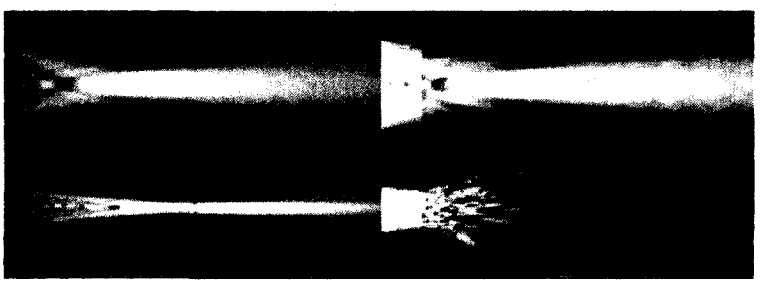

Fig.1.2. Optical images of the acoustical fields after their propagation through the thick skull bones[33].

1.1. Historical Notes

Signal propagation through the skull bone can be presented as the product of a convolution function representing the initial signal with some unknown function referred to as the *pulse transfer characteristic* which itself is constant in time [10]:

$$s_{out}(x) = s_{in}(x) \otimes h(x - x_0) \tag{1.1}$$

Therefore, if this pulse transfer characteristic can be estimated, a matched filter can be created, which may in turn be used to reconstruct the initial signal shape. This procedure is named 'matched filtering process' and has been widely used in radio and sonar systems for more the 60 years.

Due to the fact that it is impossible to calculate the pulse transfer characteristic of a complex filter like skull bone, it must be obtained through direct measurement. Various methods and approaches for determining the pulse transfer characteristic have been presented over the years. Some of them include obtaining skull bone profiles via X-Ray or MRI (K.Hynynen) [1-3], the reference source method (M.Fink) [4-9], and directly measuring the skull bone profile by means of an ultrasound sensor (V.Svet, A.Molotilov, S.Baykov) [10,11]. Each of these methods has both advantages and restrictions as follows

- The Hyhynen's method (via X-Ray or MRI) measures the skull bone profile with high precision; it does not, however, yield information about its acoustical properties [1-3].

- The Fink's method (the reference source method) is another unique method with high accuracy. However, it is not clear how this method can be practical due to the fact that the reference source must be placed within the soft brain tissue [4-9].

- The Svet-Molotilov-Baykov's method enables a less accurate reconstruction of the complex pulse transfer characteristic but, the advantage of this method is that it measures the skull bone profile with the same sensor that is used for visualization which makes it a noninvasive method [10-11].

Over last twenty years, as a result of the development of phased array technologies, novel qualitative ultrasonic transcranial techniques have also been introduced for both diagnostics and therapy. As such, two primary investigation methods were put into practice at nearly the same time. Although these techniques are somewhat similar in nature, as will be shown below, they are certainly distinct.

The first method was developed at the University of Paris VI under the direction of Professor M. Fink [4-9]. This method is commonly referred to as Time Reversal Mirror (TRM) method. As a matter of fact, TRM is a modification of wavefront inversion methods which had previously been established in radiolocation and hydroacoustics. This method takes advantage of the remarkable properties of piezoelectric transducers. In particular, transducers are reversible (they may both transmit and receive acoustic signals), highly linear, and permit immediate measurement of sound wave parameters [4-6]. According to this method, the acoustic pressure field $p(r_i,t)$ is recorded by each receiving array element, with respect to both position r_i and time t. The recorded data are digitized and kept during the T time interval. Then the acoustic pressure field is

reradiated by the same array elements in the inverse time order (i.e. from last to first signals), that is equivalently the $p(r_i, T-t)$ acoustic field radiation.

This procedure transforms the divergent source acoustic field into a converging wave which is focused on the initial source. Unlike standard mirrors which produce a virtual image of acoustical object, this method produces a real acoustical image of the original source. This method, realized through the use of 1D or 2D transducer arrays, remains efficient even if an inhomogeneous media is present between the target and the mirror. Here each transducer is connected with its own electronic circuit which consists of an amplifier (for received signals), analog-digital converter (ADC), memory block and programmable radiator. The radiator is able to synthesize a time-inverse version of the retained signal [4-6].

This method had initially been developed for a well-defined medical task; namely an attempt to determine the stone location during lithotripsy [4-6]. Under such conditions focusing the destructive ultrasound waves is a difficult task due to sound velocity heterogeneity and ultrasound beam distortion. Furthermore, sometimes stone dislocation can happen up to 2 cm. Hence it is necessary to achieve highly precise ultrasound beam focusing on the stone. To do this it is necessary to pick out the reflected target against the reflections of other stones and organs walls. Thus, the interested area is irradiated by an ultrasound array. The same array is used to record the reflected signal before it is time inversed and reradiated. After this set of iterations the ultrasound beam is focused on the most reflective target and a high amplitude wave is used to destroy the stone.

Additionally, the same method has been used by J.-L.Thomas and M.Fink [7], M.Tanter et al. [8], J.-L.Aubry et al. [12] and M.Pernot et al. [13] for the investigation of focused ultrasound propagation through an intact human skull. J.-L.Thomas and M.Fink [7] used a single element of size 1x10 mm as the source. The linear array consisted of 128 elements, approximately 1x25 mm in size with a central frequency of 1.5 MHz. The elements were placed on a concave surface with a radius of 100 mm. The acoustic pressure field was then created by a single element and in turn written to the entire array.

As the next step, the recorded signals were inverted in time and started to radiate simultaneously by all the 128 elements. In this mode the single element was used as a receiver to scan the acoustical field.

J.-L.Aubry et al. also accomplished the TRM procedure in a similar way [12]. During a biopsy, aimed at estimating cancerous growth, a tiny hydrophone was placed in immediate proximity to the growth. The hydrophone was then used as a point source. The radiated ultrasound pulse that passed through the media (including the skull bone) was recorded by a linear array. The hydrophone was then removed and the time inversed signal with amplitude compensation was reradiated. This procedure allowed for phase and amplitude corrections of the aberrations caused by the skull bone. Through focus shifting in space [8], the entire growth could be heated on a point by point basis.

Furthermore, another method called space-time inverse filtering technique [9] represents a further development of this approach. Here the biopsy allows one to place a series of transducers in tissues within a particular area of interest. Thus, the received signals for the pulse response of all transducers can be used to precisely focus on an established point. This experiment demonstrated that the focusing quality after ultrasound propagation through human skull bone was the same as that which can be achieved in water. Furthermore, it is possible to compensate for both the phase distortions and attenuation due to the skull.

The distinguishing feature of the investigation conducted by the aforementioned group is that the skull bone was assumed to be a heterogeneous structure with variant local acoustical parameters within each region of the skull. Furthermore, the possibility of estimating the acoustical properties of the skull bone from MRI and CT (Computer Tomography) during this study had significant impact on the development of this method. In fact, the CT method is more informative because it reveals the parameters of internal skull bone structure [9]. In fact, J.-L.Aubry et al. [12] demonstrated how local sound velocity, absorption and density could be estimated from CT data. This data was later used in the numeric simulation of a three dimensional wave equation by the finite

difference method [15]. The simulated wave fronts passing through the skull were found not to differ from experimental wave fronts passed through the same region of the real skull bone [12]. Moreover, the wave front created by the virtual point source placed within the brain after propagating through the skull bone could be recorded by a set of receivers. These same conditions can be set up experimentally with a simulated wave front inversed in time and experimentally radiated by a real array. Hence, the ultrasound focusing problem can be solved without the necessity of having a physical sound source inside the brain. Thus, the phase and amplitude aberrations due to the skull bone can be non-invasively corrected. This method is promising for brain hyperthermia [12].

However, the essential problem that remained unsolved was the necessity of focused electronic scanning from a point that was within immediate proximity to the growth. The reason was that all previously developed powerful therapeutic arrays utilized regular element positions. Those arrays did not allow focused scanning for the necessary distance without the formation of sizeable side lobes within the directional pattern. A successful attempt to overcome this problem was undertaken in an investigation by M.Pernot et al. [13]. The authors used an idea which had been previously put forth by S.Goss et al. [14], where it was suggested that a hemispherical array of transducers/receivers with random element positions on the array's surface be used. These arrays consisted of 200 unit elements, each 8 mm in diameter, working at a frequency of 0.9 MHz. The total array's diameter was 180 mm with a radius of curvature of 120 mm. The application of this array and the aforementioned method of signal correction on the array's elements allowed for the sound pressure to be both increased and focused even after propagation through the skull bone. In fact, the sound pressure in the focal area was raised 4.5 times which was equivalent to a temperature increase of approximately 20 times at the focal point. The experiments were conducted at several skull bone positions and they all yielded in sharp focal points. The distortions were found to be significant. Due to their reported data [14] the sound velocity in the skull bone was 3500 m/s and also the absorption coefficient in some bone parts reached values of about 8 dB/mm. It was interesting that the parts of skull bone with high or low absorption were quite non-coincident with regions having high or low phase shifts.

In spite of all advantages of the method developed by mentioned French specialists, it is not without its shortcomings. The primary fault is that in the TRM method an ideal point source is needed. In fact, the point source or the scattering object must be the brightest part of the extensive target [7]. The authors suggested that this condition can be easily fulfilled if a tiny hydrophone is placed within the brain tissues [12,13]. Unfortunately, the practical realization of this solution is extremely complicated. As such, the authors suggest that a virtual sound source be used in the tissue as an ideal scattering object before conducting simulations [12]. Naturally, the efficiency of this method must be confirmed during further investigations.

Another technique, based on matched filtering processing and analogous to TRM, has also been suggested by Svet-Molotilov-Baykov [10,11]. In this method, the inverse wave front procedure for wideband probe signals is used and information about skull bone structure has been extracted from the ultrasound field. Before matched filter processing, the phase array has been used to measure the local skull bone thickness under each array element. During ultrasound pulse propagation the complex amplitude is measured and, as a result, the skull bone transfer function is formed. The complex transfer coefficients contain information about both local thickness and local absorption. Certainly this method has a great advantage as it does not require either a local sound source (virtual or physical) or another imaging method (MRI or X-ray) to determine the skull bone's profile. As such, this method has been suggested not only for ultrasound therapy but also for the acoustical imaging of brain structures. The major disadvantage of this technique is that a linear ultrasound array must be used; the 1D phase arrays are limited due to the 2D skull bone curvature. As a matter of fact, our study is also closest to this method as will be discussed in details during the following chapters.

From an experimental point of view, this method has been tested *"in vivo"*. The first acoustical images of internal brain structures were obtained during the experiment and compared with X-ray images [10,11] (Fig.1.3).

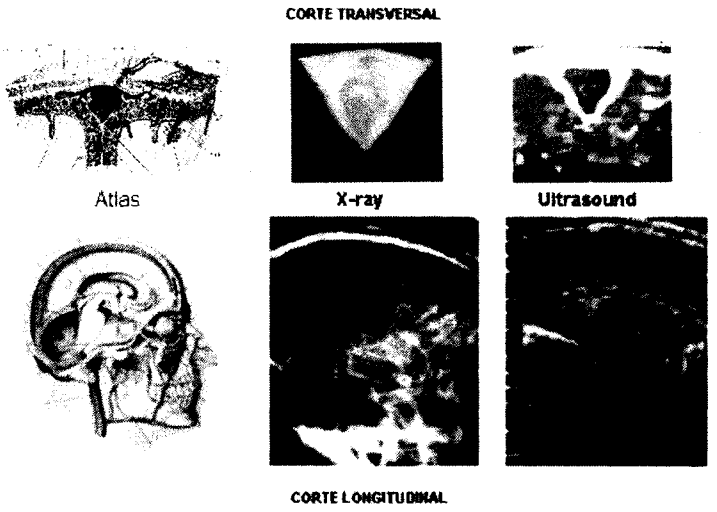

Fig1.3. Acoustical image of the venous sinus[34].

A great number of papers concerning the investigation of the potential for noninvasive brain therapy through the intact skull were performed by K.Hynynen. The distinguishing feature of his investigations was the use of homogeneous human skull bone. Here it was assumed that the main contribution to distortions during focused ultrasound propagation through the skull was due to irregularities in bone thickness. Also, the sound velocity and density for the skull bone were considered to be twice that of water and brain tissue. This unreal assumption considerably simplified the calculations which could then be completed only having to take into account geometrical beams distortions.

In J.-L.Aubry's study, [12], the importance of heterogeneous skull bone structure was noted and numeric simulations were undertaken. The wave front from the virtual point source passed through the skull and the source position reconstruction were considered in the following structures as the skull bone

I) A heterogeneous structure

II) A homogeneous structure

and

III) A model without any correction

Corresponding intensity (pressure squared) distributions versus the distance from the focal point are presented in Fig.1.4 (in relative units).

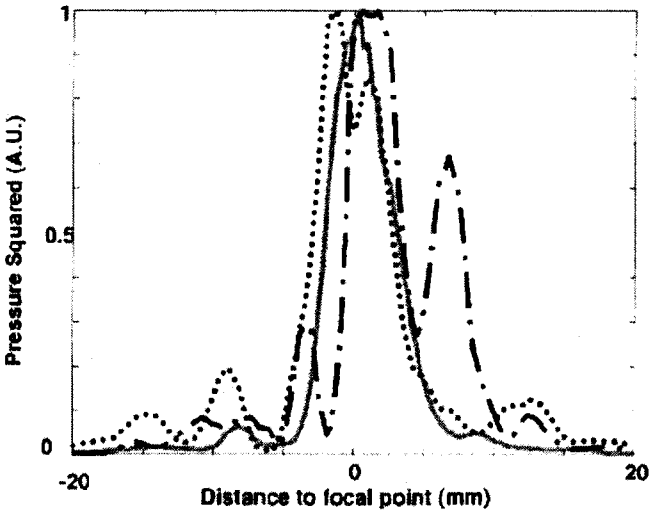

Fig1.4. Power distribution versus distance form the focal point. i) The gray line represents calculation results by the TRM method for a heterogeneous skull bone model. ii) The dotted line represents a homogeneous model. iii) The dash-dot line represents power distribution without correction. [12].

Obviously, the homogeneous model (dot line) essentially improved the focusing quality in comparison with the absence of correction calculations (dash-dot line). At the same time, the level of the side lobes was 10 dB less. Besides, the homogeneous model distribution curve line is more symmetric with respect to the focus. On the other hand, the focusing quality of the heterogeneous model is better than that of the homogeneous model. In addition, the distribution curve is absolutely symmetric relative to the focus and the side lobes are very small. Thus, according to the authors [12], the heterogeneous model is more precise with respect to hypothermia of brain tissue.

The investigations by K.Hynynen's laboratory in the field of focused ultrasound propagation through the intact skull began a couple years later than the French scientists. Despite this delayed start, their work soon proved equally fruitful. The goal of their work was to demonstrate the possibility to destroy deep internal brain structures through the

intact skull bones not by traditional heat coagulatory necrosis, but by tissue cavitational destruction [17]. Because cavitational thresholds in tissues are only weakly dependent on the effect duration, the same destruction can be obtained through the use of several short, high intensity ultrasound pulses. In this way the damage to the bone tissue due to the heat, produced in the emitting area, could be avoided. For acoustical field measurements a tiny hydrophone was used. Using this hydrophone the phase shift at each element of the array could be measured. These phase shifts were used to compensate for the distortion resulting from the human skull bone. The destructions were produced in rabbit brain tissues *in vivo* after the ultrasound propagated through their skull bone. It turned out that destruction could be achieved by a single transducer only if its frequency was no more than 1 MHz. An array of transducers was also used in a similar case. The phase measurements from the 60 elements on the 2D array demonstrated that at a frequency of 0.6 MHz (wavelength 2.5 mm) 80% of the phase shifts, caused by the skull bone, were less than 90^0. In the other words, most of the elements caused an acoustical pressure increase within the area of focus. If the frequency was increased to 1.58 MHz (wavelength less then 1 mm) the number of such elements decreased to 50%, resulting in reduced focusing quality. In short, the use of phased arrays permitted phase correction for the elements, allowing satisfactory focus quality even at a frequency of 1.58 MHz. Also, the destructions in the brain tissue were not accompanied by heat injuries in skull bone.

Also, in their theoretical investigation, J.Sun and K.Hynynen [15] developed an effective numerical model. Here the whole experimental apparatus was considered as a three layered structure; i.e. water, bone and brain. The geometrical characteristics were presented in numerical form according to an MRI analysis of the skull. This model permitted the simulation of focused ultrasound propagation through the skull by taking into account wave absorption, diffraction, refraction and scattering. During this study, the focusing was achieved using a 2D phased array, 10 cm in diameter, with a radius of curvature of 10 cm. The array's surface was divided into various numbers of square (in projection) elements (from 4×4 to 16×16) and the frequency was varied from 0.5 to 1.5 MHz. In the absence of phase correction on the array elements the quality of focusing was diminished. However, in spite of high attenuation in the skull bone, complicated

skull shape and varying skull thickness, the phase correction of the array elements minimized focus shift at the calculated position, reduced side lobe levels and raised the focus intensity. According to the authors, the optimal size of the elements was approximately 5 to 6 wavelengths. On the other hand, for the 1 MHz frequency, the optimum array had 10x10 elements, each having an individual size of 1×1 cm^2. Finally, due to the potential for skull heating, it is suggested that the ultrasound frequency during surgery through an intact skull should not exceed 1 MHz.

The double layer model (bone, brain) was described in the next theoretical paper by the same authors [16, 17]. Here it was supposed that the ultrasound sources (phase array elements) were placed in contact with skull. In order to sufficiently increase the sound pressure at a fixed point within the brain, the surface of the array, and hence the surface of the skull under radiation, was maximized (actually 6 times more than for a typical single focused radiator). This allowed the pressure in the brain to be increased by three times, greatly reducing the potential for local skull heating. A frequency of approximately 0.6 MHz was optimal to bring about maximal acoustic pressure and, in turn, maximal heating at the focus. According to the authors there also are some restrictions in this method. First, the numerical refractions, the stationary waves and the shear modes were absent in the skull bone. Also, the skull bone was assumed to be a homogeneous structure; which means that individual variations in both shape and thickness were not taken into account.

The experimental testing of the theoretical conceptions described above was conducted and reported in a paper by the same research group in 1999 [16]. A skull segment had been preserved in formaldehyde before experiment. The array was made of a single transducer with a frequency of 1.1 MHz, having a diameter of 10 cm and a radius of curvature of 8 cm which was divided into 76 equal in size elements. The elements were acoustically separated by a silicon mastic and power was supplied using a 256 channel power amplifier which permitted digital amplitude and phase adjustments in each channel. The array and skull bone were placed in a tank of degassed water and the hydrophone was used for acoustical field control. Two methods were used for the phase

correction of the array elements. The first was based on the above described calculations regarding the geometrical characteristics of skull using the MRI data; the second method, on the other hand, was based on measuring the phase shifts at each array element, where a hydrophone was placed at a set point under the skull bone and served as a point source. The experiment demonstrated that the first method of phase correction resulted in an increase of sound pressure at the focus point up to 95% (as compared to the case when phases at all elements were equal, i.e. without correction). With this correction the pressure at the focus was 9% of that which was measured in water without the skull. The phase correction conducted with the hydrophone allowed a sound pressure increase of only 3% more than the pressure in the first correction method. Thus, according to the authors, the method for phase calculation using MRI data for the skull shape and thickness is acceptable for ultrasound brain therapy through the intact skull. However, for clinical use it is necessary to also overcome a set of other difficulties associated with this method. These difficulties are

1. Phase distortions are due to skull bone but not brain tissues and skin.
2. The measurements with bone tissues were conducted *in vitro* but not *in vivo*.
3. The phase error was not considered to influence the focus depth in the brain.
4. The power levels that were used were considerably less than that which is expected for brain tissue destruction.
5. The larger element size limited the possibility of utilizing electrical scanning outside the geometrical focus where the maximum intensity occurred. Thus, scanning can only be obtained via a mechanical method.

Further, G.Clement et al. [18] investigated the possibility of effectively reducing the number of array elements and subsequent power channels. In fact, this was achieved by rotating simple arrays around some axis of skull symmetry. Two examples of these kind of arrays are shown in Fig.1.5.

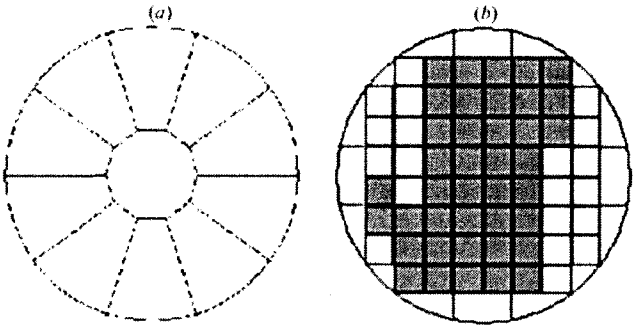

Fig.1.5. The geometry of simple arrays which were used for simulating multi-element arrays with (a) 11 elements and (b) 64-elements 40 of which are active [18].

The first array in Fig.1.5 was optimized for 0.6 MHz and had a diameter of 10 cm and a radius of curvature of 8cm. This array consists of 11 similar elements. The second array (0.5 MHz in frequency) consisted of 64 square (in projection) radiators, each $1cm^2$ in size; only 40 (black-outs at the Fig.1.5) of these elements were active. These arrays were placed at four different positions to reproduce the effect of a large array (Fig.1.6). In reality, it was more appropriate to rotate the skull relative to the array.

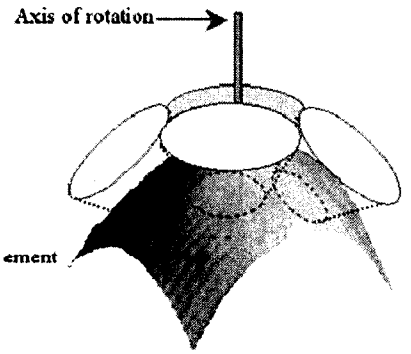

Fig.1.6. Experimental scheme of a small array placed at 4 different positions to reproduce the field of a large array [18].

The mentioned series of investigations was conducted using two virtual arrays with 40 and 160 number of elements respectively. The field measurements were accomplished via a tiny hydrophone. The phase corrections corresponding to the above described method led to increased focusing quality for the 44-element array. After phase correction the acoustical pressure increased from 26% to 42% of the value in water. The maximum mechanical displacement of the array relative to skull was ±15 mm. The authors estimated the possibility of electrical scanning using the 160-elements array to be ± 10 mm. The last number seems rather conservative because the acoustical field measurements, conducted with the hydrophone, were most likely out of the area where the powered secondary intensity maximum should occur.

K. Hynynen et al. also designed another array of transducers to make destruction in a soft tissue through human skull [19]. The array had a central frequency of 0.6 MHz and was arranged as a hemisphere with a radius of 15 cm. The array consists of 64 elements. A picture of the array is shown in Fig.1.7 and presented schematically in Fig.1.8. The field, produced by the array, was then measured with a tiny hydrophone (0.2 mm in diameter). The hydrophone was also used for phase correction using the same above described method.

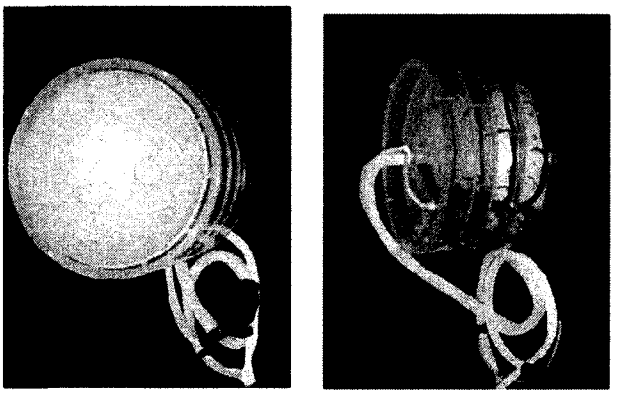

Fig1.7. Photo of a 64-elements hemispherical array [19].

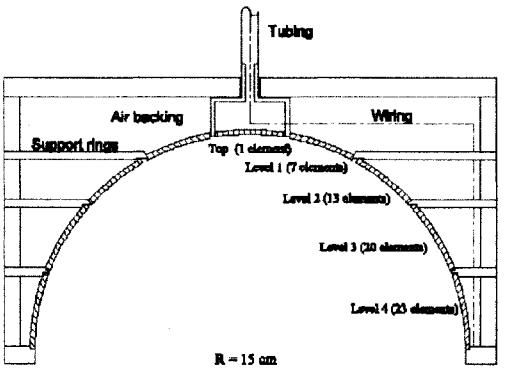

Fig.1.8. Schematic configuration of a 64-elements hemispherical array [19].

As mentioned, the tissue destruction was undertaken in rabbit muscular tissue after ultrasound propagation through a human skull. It was produced at the maximum possible power of the array (2624 Watt, 41 W/channel) with an 8 Sec exposure. The temperature of the skull surface exceeded the room temperature (24°C) by 12.4°C to 18.6°C during several tries. The authors also conducted numerical simulations for arrays of the same number of elements and also for those having 8, 11, 64, 228 and 501 elements. The ultrasound field was calculated at the geometrical centers of the mentioned arrays. The results are presented in Fig.1.9. It can be seen from the plot that the square of the sound pressures (intensity), normalized to the correspondence value for the 64-element array, were 0.52, 0.56, 1.0, 1.4, and 1.52, respectively.

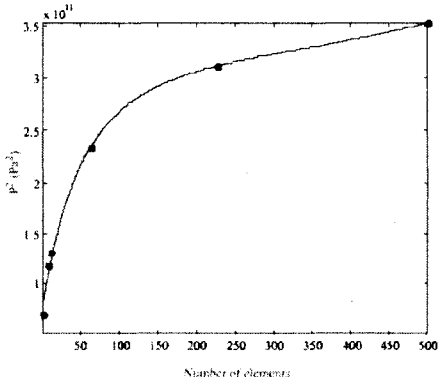

Fig.1.9. Sound pressure squared (after propagation through the skull) as a function of the number of array elements [19].

Therefore the 64-elements array noticeably exceeds the characteristics of the arrays with a larger number of elements. The authors conclude that the mean focus intensity, although important, is not the single criterion for estimating optimal array characteristics. No less important are the levels of the secondary intensity maximums during electronic scanning outside the geometrical focus. In fact, this criterion is of considerable help in determining how safe it is to use a particular array. As mentioned earlier, it was demonstrated that each element should not exceed a particular size, for example 5 wavelengths. This fact inevitably leads to an increase in the necessary number of array elements.

This set of laboratory investigations is concerned with the study of particular problems related to those described above. The numerical calculation of tilted sound wave absorption and propagation through skull bones was accomplished by [20] – all previous calculations were restricted to waves of normal incidence. Here it was demonstrated that the inner reflections of the wave within the skull have less of an influence on phase distortions at small incidence angels to the skull bone.

Two different methods for brain surgery and therapy with focused ultrasound through the intact skull were developed in the K.Hynynen laboratory around 2002. The first of these methods is minimally invasive, the second completely noninvasive. The main feature of the first method [2] is that flexible tiny hydrophones are introduced into the blood vessels to control the focusing quality. In contrast to the methods developed by M. Fink et al., here it is not necessary to place the hydrophone within a particular region of the tissue. The hydrophone should, however, be placed near the suspected area. The position of the hydrophone can be controlled by MRI imaging. The means by which the tissues are affected are described as follows. Here, the powerless signal was transmitted to the each of the therapeutic array elements. The signal was recorded by a hydrophone and the necessary phase offset for each element was determined so that the received signals were in phase. This phase correction was then utilized to move the focus from the position of the hydrophone to the region that should be destroyed. Only then is the

powerful ultrasound technique utilized. Two arrays were used in these experiments for focus scanning: a 104-element array at 1.1 MHz with a radius of curvature of 16 cm and a 120-element array at 0.81 MHz with a diameter of 19.2 cm. The 64-element hemisphere array (0.6 MHz frequency) was then used for destruction of some muscular tissue from a pig placed behind a human skull bone. All arrays developed by the authors consisted of regularly placed elements at the array surface. The destructions were produced at a distance of 10 mm from the hydrophone using 1900 Watts of power for 30 Sec.

The principal results concerning the development of a completely noninvasive method of focused ultrasound were also developed later [3]. Here an improved calculation model of ultrasound propagation through the skull bone, method of measurements (particularly with respect to determining the geometrical parameters of the skull), the instruments for focused ultrasound that were developed by authors, as well as the results of experimental investigations are reviewed in detail. The focusing system was comprised of a 2D array. The array was arranged as a 30 cm diameter hemisphere (0.74 MHz frequency) consisting of 1-3 piezoelectric elements divided into 500 separate sections, of which 320 were active. A 500-channel amplifier with 1800 Watts of power was used to supply the array. The calculation of the phases and amplitudes of the array elements was conducted by taking into account all data concerning the thickness and inner structure of the skull bone. For the focusing quality a PVDF-hydrophone, 0.2 mm in diameter was used. The hydrophone was placed in the water tank and was moved by means of a 3D-positioning system with stepper motor. The hydrophone measurements were used to optimize the 2D array and to compare this method with the phase calculation results. The calculation methods enabled an intensity of 45-46% of the intensity after the hydrophone phase correction (the average of 10 specimens with individual dispersion 22%-59%). According to the authors, the results of investigations demonstrate the ability to use the offered method for completely noninvasive surgery and therapy by affecting the tissues through the intact skull.

One of the interesting results obtained in afore mentioned study, [3], was that the focus intensity produced by the hemisphere array was considerably reduced if the focus

was moved mechanically from the geometrical center of skull towards the skull surface. At the same time it was observed that at distances less than 40 mm from the surface, the intensity was significantly reduced (by more then 4 times) and the field distortions were considerably increased. The authors further suggested that for small target depths their assumption that refraction effects in the skull bone are negligible is no longer valid. In this case a special method should be developed to achieve destruction (multiple reflection effect in the skull bone was one of the main research areas of this thesis as will be discussed in chapter 2 and chapter 3).

The mentioned problem was completely investigated and tried to be solved later by the same group (K. Hynynen et al. [22]). Here the authors noted that the assumption that ultrasound propagating through the skull bone consists only of longitudinal mode, enables good results for small angles of inclination beams. On the other hand, this assumption is not valid if the inclination angle exceeds 25^0 and approaches the first critical angle. The above description explains the amplitude reduction by means of a longitudinal wave model. According to the authors, the transformation of longitudinal waves (in the skin) into shear waves (in bone) and then again into longitudinal waves (in brain) is not responsible for the strong signal distortion and sharp amplitude decrease. In reality the amplitude of the signal in the focused beam is increased in comparison with the case where purely longitudinal waves propagate through the same region of the skull bone. In fact, there exists a potential advantage in the propagation of longitudinal-shear-longitudinal waves in comparison with purely longitudinal waves as there is only a small difference in the sound velocity of shear waves in skull bone (about 1400 m/s) and longitudinal waves in water, skin and brain (about 1500 m/s). On the other hand the longitudinal wave velocity in skull bone is twice as high. Thus, shear waves in skull bone are characterized by the best impedance agreement between the mediums, bringing about less refraction and phase distortions. The authors investigated the role of shear waves as a mechanism to increase the effectiveness of ultrasound propagation through the skull bone. The authors first theoretically and then experimentally investigated the process of wave transformation in a test specimen (plastic parallel-plane) and in a human skull bone using a converging ultrasound beam.

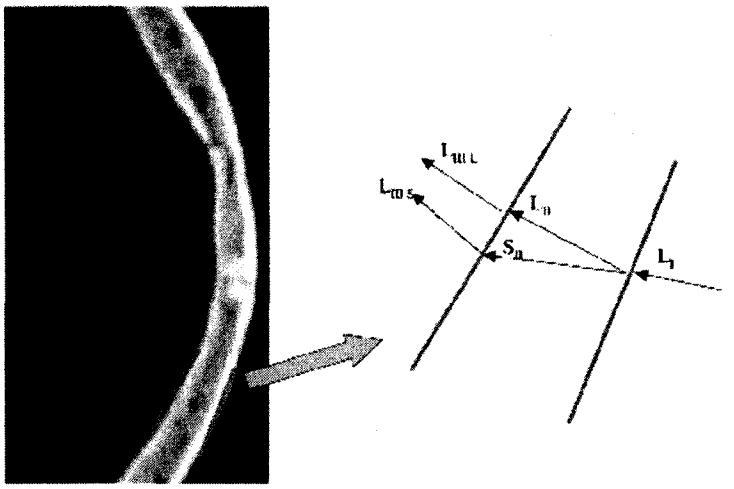

Fig.1.10. The CT images are divided into sections containing 3D unparallel planes and the shear mode appearance was investigated in each section [22]. The symbols I, II, III denote the different mediums: skin, bone and brain. L - longitudinal waves, S - shear waves.

A schematic image of the wave propagation is presented in Fig.1.10. The waves reflected from the boundaries are not shown in the image. The theoretical investigations conducted by authors allowed them to consider the effect of shear waves within the previously developed model of sound propagation through the skull bone. The experiment was conducted with single focused transducers (for plastic 1.5 MHz in frequency, 12 cm diameter, 16 cm radius of curvature; for bone 0.74 MHz in frequency , 8 cm diameter, 15 cm radius of curvature). The plastic plane (11.8 mm thickness) and skull bone segment (5.3 mm thickness in the center) were rotated at various angles relative to the converging ultrasound beam. The calculated results were in good agreement with experiments results up until the first angle approached the critical angle ($26\text{-}32^0$ for the bone). In fact, at these angles and, in particular at larger angles, these results strongly differ from the previous ones and only agreed with calculations which accounted for the shear wave mechanisms. The peak pressure amplitude of the shear waves was 35-55% of peak amplitude of longitudinal waves. However the effect of the share waves on the brain tissues can be great due to the small variation between the velocities of the two wave modes, as described earlier. The authors suggest that this

method can be useful not only for noninvasive neurosurgery and brain therapy, but especially for focusing at lesser depths below the skull surface.

Further, acoustical analysis of the human skull bone and brain tissue will be discussed in this chapter as the information is of a great importance for the rest of this report.

1.2 Acoustical analysis of the human head tissues

The human skull bone is inhomogeneous and consists of three layers [27, 28] as shown in Fig.1.11.a. The top and bottom layers are composed of compact bone, while the middle layer, the *diploe*, is only present in the skull bone of an adult (Fig.1.11.b); It is absent in both children and animals. The diploe layer is composed of spongy bone tissue filled with cavities of liquid. Inside the diploe there are numerous diploic canals within which there are blood vessels which keep the bone tissue alive.

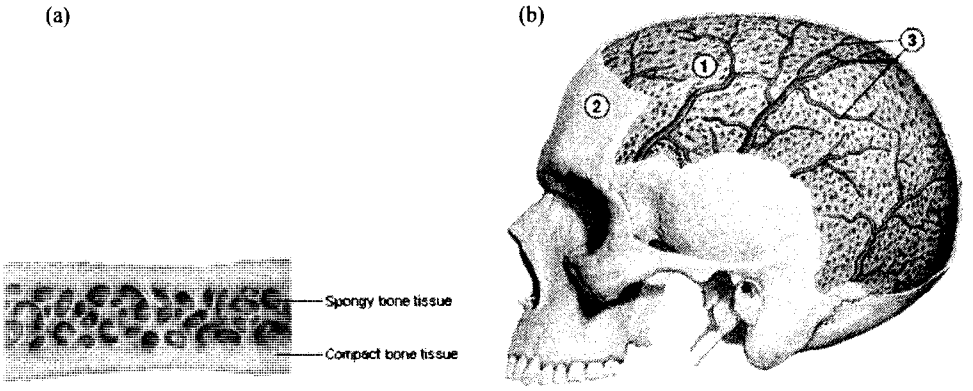

Fig1.11 (a) Bone Tissue (b) Human skull: 1-diploe (spongy bone tissue); 2-compact bone tissue. 3-diploic canals.

Total skull bone thickness of an adult human defers from 15 to 20mm [27, 28]. The bottom surface of skull bone is irregular with the magnitude of irregularity ranging from 8-15 mm through 100 mm. In fact, the skull bone can be effectively represented as a curved plate with a smooth top surface and curved bottom surface. The acoustic parameters of the skull bone are presented in Table 1. These data fully describe the ultrasonic properties of the various tissues found within the human head [29-31]. The acoustical properties of brain tissue are close to that of water.

Table 1.1. Ultrasonic properties of human head tissues [29-31].

	Skull bone, Full skull	Skull outer ivory table	Skull inner ivory table	Skull diploi	Brain	Blood	Blood vessel, walls
Sound velocity, m/s	2060-4100	2920-2960	2590-3098	2240-2870	1460-1570	1530-1600	1490-1580
Density, kg/m^3	1800-2000	1930	1970	1770	900-950	1060	
Sound attenuation, dB/m; frequency, MHz							
0.3	200-230				85-90		
0.6	450-520						
0.8	750-1500						
0.87					140		
1.0		1450	1870	1300			
1.2	1450-1700						
1.6	2800-3200						
1.7	3300-3550				180		
1.8	3600-4300				120		
2.0						34	
2.25	4700-5300						
2.9					240		
3.3					270		
3.4					365-370		
3.5	7800-8000					69	
5.0						110	
6.0							150
7.0						170	
10						250	

The main difficulty that must be overcome in transcranial brain ultrasonic medical diagnostics is the relatively high ultrasonic attenuation that occurs in the skull bone. Furthermore, the probing signal brings about multi-reflections from the upper and inner bone surfaces. In fact, the skull bone can be presented as a parallel-sided plate. If a pulse signal is transmitted, the received signal can be represented as a time related to consecutive signals with reduced amplitudes. The useful signal, reflected from the object of interest is often masked by the multi-reflected signals, limiting and complicating the possibility for detection and identification (Fig.1.12)[33].

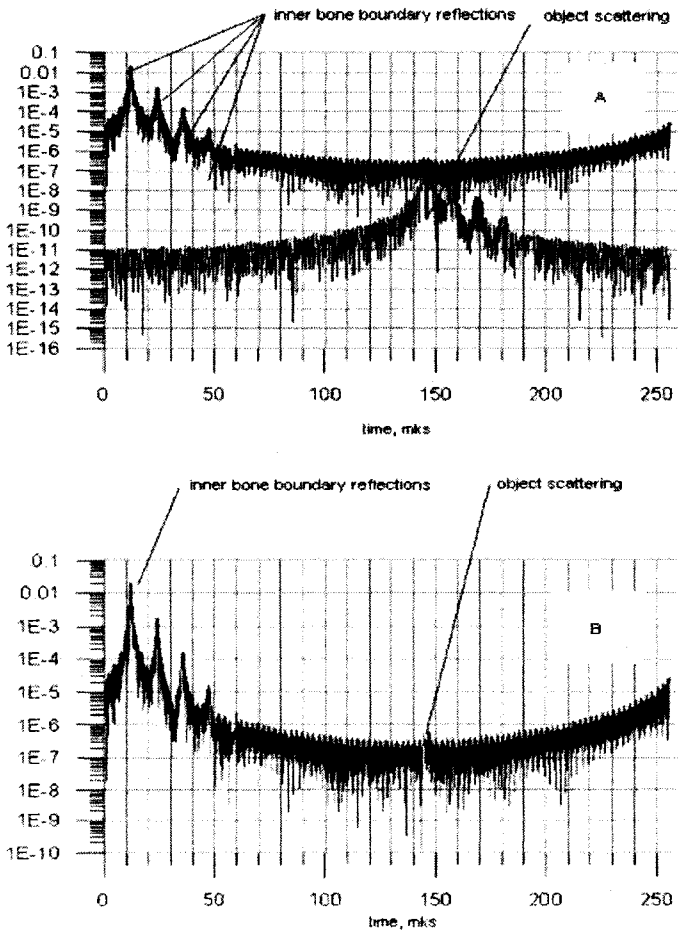

Fig.1.12. (a) Reflected signals scattered from the object, as well as multi-reflection signal from the inner bone boundary. (b) The signals at the receiving array.

Finally, because the skull bone is a heterogeneous media with an irregular inner surface, the skull bone model is more accurately modeled as a parallel-sided plate with an inhomogeneous layer adjacent to it. The ultrasonic wave which passes through the layer is transformed into a spectrum of waves refracted in different directions.

The medical standards governing the allowable intensity of ultrasound are determined according to skull bone overheating and liquid cavitations. As such, the allowable transmitted intensity in ultrasonic diagnostics is restricted to 150-300 mW/cm^2. In fact, the ultrasound used in diagnostics has a lesser intensity than that used in other medical procedures [32]. For example, ultrasound used in physiotherapy heats tissue no more than 1^0C. This correlates to an acoustical transmitting intensity of $1W/ cm^2$ for a time of 10 min. For treatment of hyperthermia, unfocused ultrasound with $10W/cm^2$ is used for 1-2 hours. The tissue temperature is held at $42\text{-}43^0C$.

Hence there are high restrictions regarding the intensity of signal that can be used as well as considerable power losses to the ultrasonic signal due to attenuation as it passes through the skull bone. Both of these problems can be addressed by using multi-element phased arrays with electronic scanning.

1.3. Conclusion

According to the reviewed materials, the majority of the articles concerning matched-filtering process are devoted to the therapeutic effect of ultrasound or ultrasound surgery. There are considerably less articles discussing ultrasonic imaging of the brain structure through the intact skull. This is most likely due to the fact that ultrasound therapy requires rather low frequencies (not higher than 1 MHz), which effectively reduces spatial resolution. As such, frequencies higher than 1.5 MHz are required for ultrasound diagnostics.

However, during this thesis I tried to develop a new theory and simulation for noninvasive *image reconstruction* through a simplified simulated skull bone. The goal of this study was to reconstruct the position of a static object places somewhere behind a scattering medium (simplified human skull bone). My study was based on the previously explained matched filtering process and more specifically TRM. The main difference between my theory and the TRM was that instead of having the array elements reradiating the signals in the inverse time order, as used in TRM [4-9], the phase information was saved on either a simulated or real array of receivers and the simulated re-radiation happened in inverse direction due to inversed previously saved phases to make the image reconstruction plane. The detailed explanations on the theory and experiment (my contribution to this study) are presented in chapters 3 and 4.

Chapter 2

ACOUSTIC WAVES IN ISOTROPIC MEDIA

In this chapter, the main acoustical principles and theoretical considerations used in developing the theory and algorithm will be briefly discussed. More detailed calculations are given in the references.

2.1. Acoustical wave modes in isotropic solid media

Unlike the fluids in which the acoustical waves only propagate in longitudinal (expansion/compression) mode, there could be both longitudinal and shear wave modes in solid media [37]. In *isotropic* solids, these two modes propagate independently and therefore they do not interfere. For each of the modes there exist a potential which the solutions for displacement in each mode is derived from its specific potential. For longitudinal mode this potential a scalar (ϕ) and, on the other hand, it is a vector potential ($\vec{\psi}$) for shear mode [37]. The displacement vectors ($\vec{u}_l$ and $\vec{u}_s$) can be obtained when the potentials are know in a solid medium

$$\vec{u}_l = \nabla\phi, \qquad \vec{u}_s = \vec{\nabla}\times\vec{\psi} \tag{2.1}$$

The displacement equations are then expressed by

$$\vec{u}_l = \vec{A}_l \exp j(\omega_l t - \vec{\mathbf{k}}_l.\vec{\mathbf{r}}) \tag{2.2}$$

$$\vec{u}_s = \vec{A}_s \exp j(\omega_s t - \vec{\mathbf{k}}_s.\vec{\mathbf{r}}) \tag{2.3}$$

Where A_l and A_s are the longitudinal and shear waves initial amplitudes respectively. $\vec{\mathbf{r}}$ is the path vector taken by the wave from the initial point. $\vec{\mathbf{k}}_l, \omega_l$ and $\vec{\mathbf{k}}_s, \omega_s$ are wave number vector and angular frequency of the longitudinal and shear waves respectively.

Having the displacement vector in hand, the other useful parameters such as velocity and pressure at each point can be easily derived [38].

2.2. Acoustic Impedance and Attenuation

As a direct analogy of impedance in electrical circuits, the absolute value of specific acoustic impedance [39], useful to characterize a bulk (infinite) medium, is defined as

$$Z = \rho V \tag{2.4}$$

Where ρ and V are density and sound velocity of the medium respectively. It is a highly useful concept in ultrasonic as will be used later in this chapter.

Another important parameter in acoustics is attenuation factor (α [dB/m]). It shows how attenuative a medium is [39]. As acoustical waves propagate through a medium their amplitude, and therefore their intensity, get damped as follows

$$\vec{u} = \vec{A}_0 \exp(-\alpha|\vec{\mathbf{r}}|)\exp j(\omega t - \vec{\mathbf{k}} \cdot \vec{\mathbf{r}}) \tag{2.5}$$

2.3. Reflection and Transmission at interfaces

Performing the majority of operations or experiments with ultrasonic waves means transmitting the waves from one medium to another where the measurement is to be performed. For this reason it is essential to have a good understanding of the principles of reflection and transmission of ultrasonic waves. As in our case the transmission is supposed to happen either from the brain tissue to the skull bone (fluid-solid interface) or in the skull, from one layer to another (solid-solid interface), these two cases are to be explained in the remaining part of this chapter.

When an ultrasonic wave is incident on an interface between to media, the resulting wave(s) have changed amplitudes and directions. Change of direction is ruled by Snell's Law and the amplitudes of the reflected and transmitted waves can be found by calculating the reflection and transmission coefficients.

2.3.1. Snell's Law and Slowness Surfaces

Consider a plane boundary between media with different acoustical properties (Fig.2.1), the boundary conditions state that the particle velocity and the normal components of the stress must be continuous at all point on the boundary [35]. This means that the incident and scattered waves must all have the same z component of $\vec{\mathbf{k}}$ tangential to the boundary. This is the basis for deriving Snell's Law.

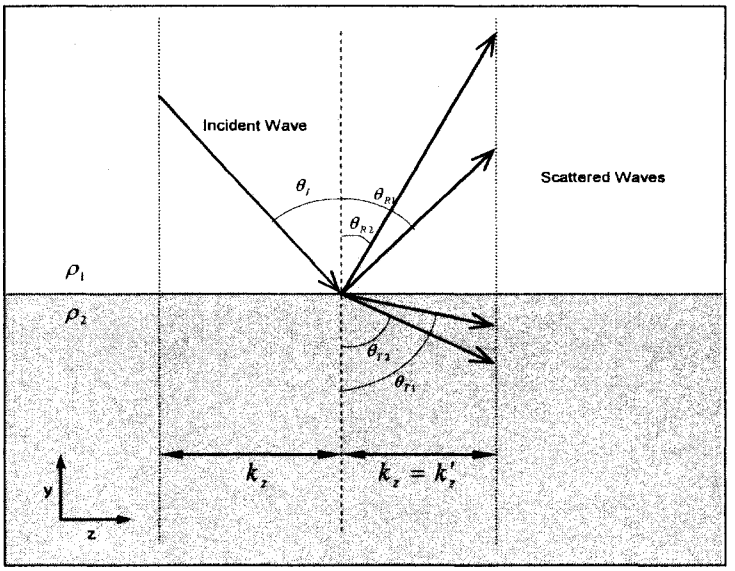

Fig.2.1. Acoustic wave scattering a plane boundary between two isotropic media.

The derivation can be performed most efficiently by using the slowness surfaces as shown in Fig.2.2. It can be seen from Fig.2.1 that the transmitted wave(s) is refracted away from the direction of the incident wave. As discussed before, in acoustic media,

there could be several refracted and reflected waves with the same value of k_{tan} as the incident wave. The slowness surface gives the magnitude of $\mathbf{k}/\omega$ as a function of its direction. From Fig.2.2 the isotropic acoustic Snell's Law for either shear or longitudinal incidence is therefore

$$\frac{\omega}{V_l}\sin\theta_l = \frac{\omega}{V_s}\sin\theta_s = \frac{\omega}{V_l'}\sin\theta_l' = \frac{\omega}{V_s'}\sin\theta_s' \tag{2.6}$$

Where $\theta_l, \theta_s, \theta_l', \theta_s'$ are the incident, reflected or transmitted angles as shown in Fig.2.2 and V_l, V_s, V_l', V_s' are the longitudinal and shear wave velocities in the first and second media respectively.

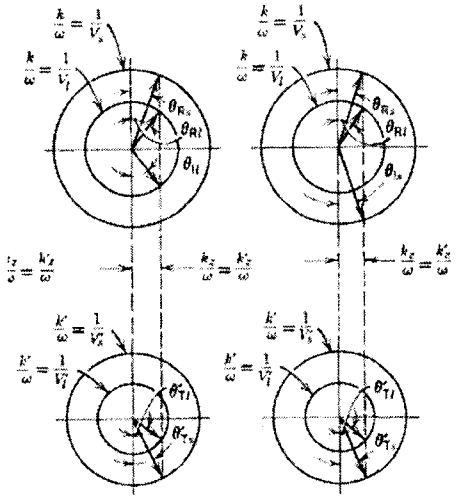

Fig.2.2. Acoustic wave scattering a plane boundary between two isotropic media [35].

2.3.2. Reflection and Transmission Coefficients at Solid-Solid Interface

2.3.2.1. Shear wave incidence

In this case both reflected and transmitted longitudinal waves are excited as shown in Fig.2.4.

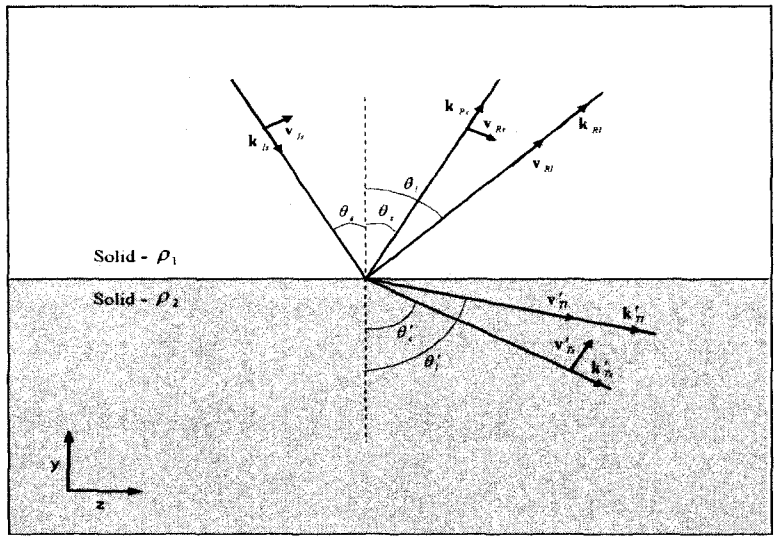

Fig.2.3. Acoustic wave scattering at a plane boundary between two solid isotropic media when the incident beam is a shear wave.

The particle velocity vectors shown in the figure can be written as

$$\mathbf{V}_{Is} = -\frac{\hat{\mathbf{x}} \times \mathbf{k}_{Is}}{k_s} A_s \exp(-i\mathbf{k}_{Is} \cdot \mathbf{r}) \qquad \text{(a)}$$

$$\mathbf{V}_{Rs} = \frac{\hat{\mathbf{x}} \times \mathbf{k}_{Rs}}{k_s} B_s \exp(-i\mathbf{k}_{Rs} \cdot \mathbf{r}) \qquad \text{(b)}$$

$$\mathbf{V}_{Rl} = \frac{\mathbf{k}_{Rl}}{k_l} B_l \exp(-i\mathbf{k}_{Rl} \cdot \mathbf{r}) \qquad \text{(c)} \qquad (2.6)$$

$$\mathbf{V}'_{Ts} = -\frac{\hat{\mathbf{x}} \times \mathbf{k}'_{Ts}}{k'_s} B'_s \exp(-i\mathbf{k}'_{Ts} \cdot \mathbf{r}) \qquad \text{(d)}$$

$$\mathbf{V}'_{Tl} = \frac{\mathbf{k}'_{Tl}}{k'_l} B'_l \exp(-i\mathbf{k}'_{Tl} \cdot \mathbf{r}) \qquad \text{(e)}$$

Applying the boundary conditions to the velocity and stress components [36] leads to the set of scattering equations

$$A_s \sin\theta_s = -B_l \cos\theta_l - B'_l \cos\theta'_l + B_s \sin\theta_s + B'_s \sin\theta'_s \qquad \text{(a)}$$

$$A_s \cos\theta_s = -B_l \sin\theta_l - B'_l \sin\theta'_l + B_s \cos\theta_s + B'_s \cos\theta'_s \qquad \text{(b)}$$

$$-A_s\mu k_s \sin 2\theta_s = -B_l(\lambda+2\mu)k_l \cos 2\theta_s + B_l'(\lambda'+2\mu')k_l' \cos 2\theta_l' + B_s\mu k_s \sin 2\theta_s - B_s'\mu' k_s' \sin 2\theta_s' \quad \text{(c)}$$

$$-A_s\mu k_s \cos 2\theta_s = -B_l\mu k_l \sin 2\theta_l - B_l'\mu' k_l' \sin 2\theta_l' - B_s\mu k_s \cos 2\theta_s - B_s'\mu' k_s' \cos 2\theta_s' \quad \text{(d)} \qquad (2.7)$$

In the above mentioned set of equations, μ, λ are Lame' coefficients of the first medium and μ', λ' are Lame' coefficients of the second medium [39]. According to above mentioned equations, the reflection and transmission coefficients are

$$R_{ls} = \frac{B_l}{A_s} = \frac{\Delta_{ls}}{\Delta} \quad \text{(a)}$$

$$T_{ls} = \frac{B_l'}{A_s} = \frac{\Delta_{ls}'}{\Delta} \quad \text{(b)}$$

$$R_{ss} = \frac{B_s}{A_s} = \frac{\Delta_{ss}}{\Delta} \quad \text{(c)}$$

$$T_{ss} = \frac{B_s'}{A_s} = \frac{\Delta_{ss}'}{\Delta} \quad \text{(d)} \qquad (2.8)$$

Where Δ is the determinant of the coefficients on the right-hand side of Eqs.(2.7) and Δ_{ls} is the determinant obtained by replacing the coefficients of B_l with those of A_s, etc. More conveniently, the determinant can be written in the following way

$$\Delta = k_z^2 \sin\theta_l \sin\theta_l' \sin\theta_s \sin\theta_s' \qquad (2.9)$$

$$\times \begin{vmatrix} -\cot\theta_l & -\cot\theta_l' & 1 & 1 \\ -1 & 1 & -\cot\theta_s & \cot\theta_s' \\ (\lambda+2\mu)\dfrac{(2\sin^2\theta_s - 1)}{\sin^2\theta_l} & \dfrac{-(\lambda'+2\mu')(2\sin^2\theta_s' - 1)}{\sin^2\theta_l'} & 2\mu\cot\theta_s & -2\mu'\cot\theta_s' \\ -2\mu\cot\theta_l & -2\mu'\cot\theta_l' & \mu(2-\csc^2\theta_s) & \mu'(2-\csc^2\theta_s') \end{vmatrix}$$

2.3.2.2. Longitudinal Wave Incidence

The case is shown schematically in Fig.2.4. The only difference from the previous part (Fig.2.3) is that the incident wave is changed from shear wave to longitudinal wave. Since the scattered wave polarizations and angles are the same in both figures, only the terms on the left hand side of Eqs.(2.7) need to be changed [36]. These terms become

$$
\begin{aligned}
&-A_l \cos\theta_l && \text{(a)} \\
&A_l \sin\theta_l && \text{(b)} \\
&A_l(\lambda + 2\mu)k_l \cos 2\theta_l && \text{(c)} \\
&-A_l \mu k_l \sin 2\theta_l && \text{(d)} \qquad (2.10)
\end{aligned}
$$

And the reflection and transmission coefficients are found to be

$$
\begin{aligned}
&R_{ll} = \frac{B_l}{A_s} = \frac{\Delta_{ll}}{\Delta} && \text{(a)} \\
&T_{ll} = \frac{B'_l}{A_s} = \frac{\Delta'_{ll}}{\Delta} && \text{(b)} \\
&R_{sl} = \frac{B_s}{A_l} = \frac{\Delta_{sl}}{\Delta} && \text{(c)} \\
&T_{sl} = \frac{B'_s}{A_l} = \frac{\Delta'_{sl}}{\Delta} && \text{(d)} \qquad (2.11)
\end{aligned}
$$

Where again Δ is the determinant of the coefficients on the right-hand side of Eqs.(2.7) and Δ_{ls} is the determinant obtained by replacing the coefficients of B_l with those of A_s, etc.

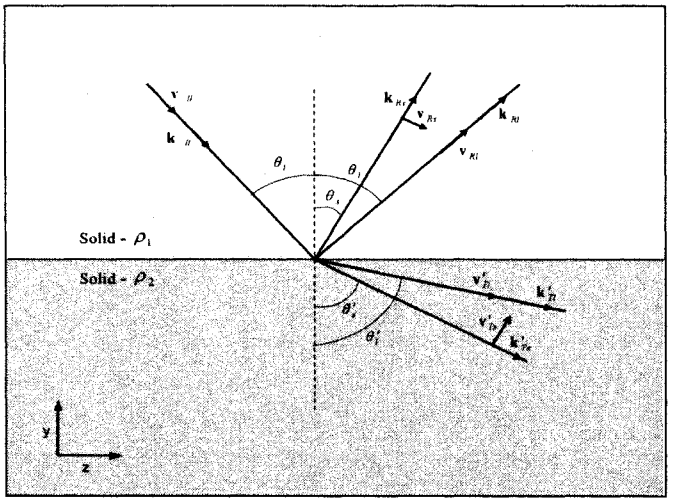

Fig.2.4. Acoustic wave scattering at a plane boundary between two solid isotropic media when the incident beam is a Longitudinal wave.

2.3.2.3. Reflection and Transmission Coefficients at Fluid-Solid Interface

As explained before, the only allowed mode in fluid media is longitudinal wave mode. Whenever a longitudinal beam reaches a solid interface, it gets partially reflected and transmitted. The case is shown in Fig.2.5. The reflected wave is also of longitudinal polarization as it propagates in fluid medium. On the other hand both longitudinal and shear modes can be excited in the second medium [39].

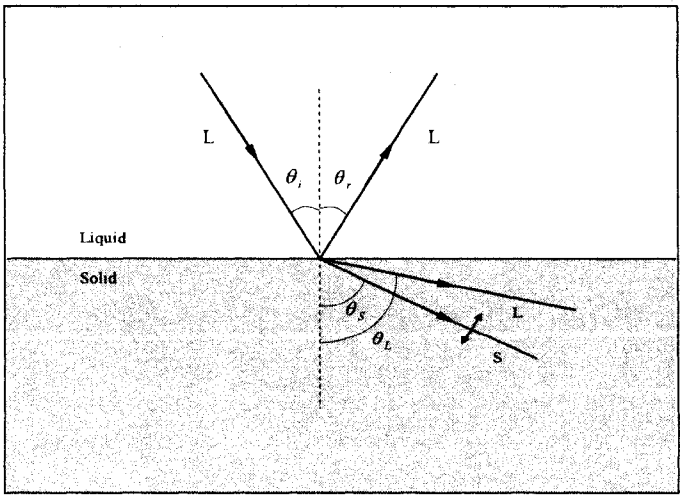

Fig.2.5. Acoustic wave scattering at a plane boundary between a liquid and a solid medium. The incident beam is of longitudinal kind.

Applying the boundary conditions to the tangential and normal components of velocity and stress respectively and following the same procedure as last section [39], the reflection and transmission coefficients for wave's displacement are derived as

$$R = \frac{Z_l \cos^2 2\theta_s + Z_s \sin^2 2\theta_s - Z_1}{Z_l \cos^2 2\theta_s + Z_s \sin^2 2\theta_s + Z_1} \tag{2.12}$$

$$T_l = \left(\frac{\rho_1}{\rho_2}\right) \frac{2Z_l \cos 2\theta_s}{Z_l \cos^2 2\theta_s + Z_s \sin^2 2\theta_s + Z_1} \tag{2.13}$$

$$T_s = -\left(\frac{\rho_1}{\rho_2}\right) \frac{2Z_s \sin 2\theta_s}{Z_l \cos^2 2\theta_s + Z_s \sin^2 2\theta_s + Z_1} \tag{2.14}$$

Where

$$Z_1 = \left(\frac{\rho_1 V_1}{\cos\theta_i}\right), \qquad Z_l = \left(\frac{\rho_2 V_l}{\cos\theta_l}\right), \qquad Z_s = \left(\frac{\rho_1 V_s}{\cos\theta_s}\right) \tag{2.15}$$

The equations derived for reflection and transmission coefficients in this chapter will be used in next chapter in order to find the effect of the simulated skull bone on any incident ultrasonic wave.

During the next chapter, the main theory of this study and the simulation developed according to the theory will be discussed and the results of the simulation will be presented.

Chapter 3

SIMULATION

3.1. General apparatus and Mechanism

As mentioned in the introduction part, the long term goal of the *Brain Project* was to reconstruct the image of a foreign static object (reflector of any kind) positioned somewhere inside the brain. The particular goal related to my research was to develop the project's theory and simulation to finish phase I. The main purpose on this phase had been defined as developing an algorithm to check the validity of the theory on a *simplified* theoretical and experimental setup as will be explained in this and the following chapter. More sophisticated and therefore realistic apparatuses remain to be studied in future after the theory showed enough accuracy and functionality. Therefore, at this point although the simulated skull bone had all its acoustical properties the same as real skull, its physical shape was simplified to be more convenient to be built and used in the experiment part; i.e. instead of a *curved* and *porous* three layered structure, a flat scattering multi-layer was simulated as will be discussed further in this chapter. Moreover, as the acoustical properties of *brain tissue* and *head skin* are very close to water, the whole apparatus in both simulation and experiment were immersed in water; just like most of the previous studies in this area ([5-9],[11-13], etc.).

The general configuration according to which the simulation has been developed is shown in Fig.3.1. The codes were developed in MATLAB 7.0.4 and a part of it, as an instance, has been included as Appendix A.

As can be seen in Fig.3.1, spherical ultrasound waves initiate from the static object which itself could be either a source of ultrasound or a sound reflector. The static object generates beams in all directions. Each beam gets attenuated due to distance as it propagates in water until it reaches the scattering medium (simulated skull bone). Scattering medium causes significant distortion to the passing through field. This

distortion includes high attenuation in skull bone layers, multiple reflections between the layers and refraction at boundaries (*skull layers* and *skull-Brain tissue* boundaries).

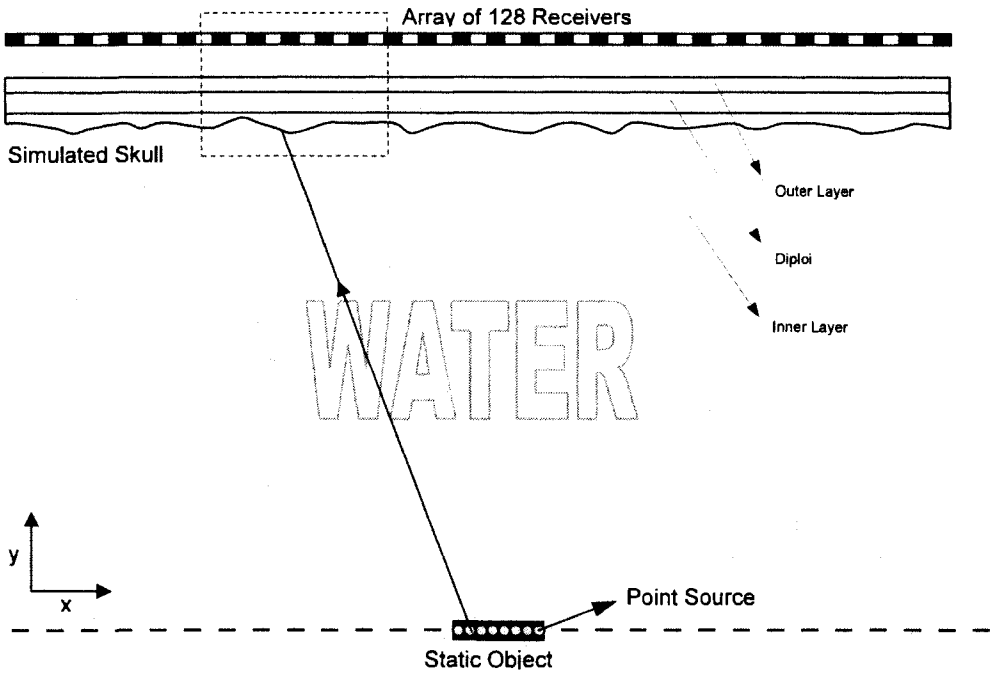

Fig.3.1. Extended source, Scattering medium (simulated skull) and array of receivers' apparatus.

3.2. Simulation Parts

Generally speaking, the simulation consisted of two main parts:

Part I

To find Intensity distribution of a propagating acoustical field, through the scattering medium, on the array of receivers as explained above.

Part II

To reconstruct the static object's position due to saved Intensity distribution on the array of receivers. As a matter of fact, this part was the practical part of the simulation as in real situation instead of the simulated intensity Distribution on the array of receivers, the real measured distribution was taken from the experiment and inserted in the

simulation to see how the software reconstructed the static object's position. More details on experimental data acquisition and relative image reconstruction are provided in chapter 4.

During this chapter, results from *part I* have being used in *part II* to get reconstruction's results. This allowed us to make sure about the primary availability of the developed algorithm before going to the experiment part.

Before developing the main body of the codes, it was necessary to formulate and simulate the main elements of the apparatus i.e. static object, scattering medium, and array of receivers with desired acoustical properties as follows.

3.3. Main Elements' Simulation

3.3.1. Static Object (Reflector)

Due to its size, the static object can be simulated as a point source or a combination of point sources. This means that any static object (also called as 'extended source' from now on) can be treated as a group of tiny elements, e.g. half of the wavelength wide as used in our study, each works as a point source of ultrasound simulated as

$$U_{i(obj)}(x_{io}, y_{io}) = U_{io} \exp(j\varphi_{io}) \qquad (3.1)$$

Where x_{io}, y_{io} are the coordinates of the i^{th} point source and U_{io}, φ_{io} are its corresponding amplitude and initial phase. The number of point sources and therefore the object's size is a matter of decision and could be set at any desired value.

3.3.2. Layered Skull Bone

According to its triple layered structure (Outer Layer, Diploi, and Inner Layer as shown in Fig.1.1), the simulated skull bone also consisted of three main layers. As mentioned before, a simplified model of skull, i.e. flat and nonporous, was used to check

the validity of the theory. Besides, as the final code needed to be examined by real experimental data, it was easier to make a flat nonporous Phantom layer than a curved porous one. Curved models and real *ex vivo* skull bone are planned to be studied in future.

Due to its randomly curved structure, the inner layer showed to be the most distorting layer. In addition, as the inner boundaries of a typical skull do not have significant change in slope, the other two layers were modeled as flat layers with different acoustical properties due to table 3.1. To develop the inner layer, two different techniques were suggested as discussed below.

Technique A: Random Phase Shifting Elements

Due to the fact that no matter how a beam penetrates and leaves a layer, in addition to attenuation, the layer introduces some phase shift to exponential part of the wave's equation, and also knowing that the inner layer's non-planar structure defers from person to person, it could have been modeled as a set of consecutive random phase shifting elements (Fig.3.1). Each element then possessed an arbitrary phase shift ($0-2\pi$) and introduced that amount to any transmitted beam. This technique was only good for the simulation part and not useful for experiment, as in the experiment the curvy structure of each physical scattering layer is known and should be considered in the reconstruction part (*part II*) of the simulation. We used this technique only to get a quick result for intensity distribution on the array of receivers and corresponding reconstruction as will be explained in section 3.4.

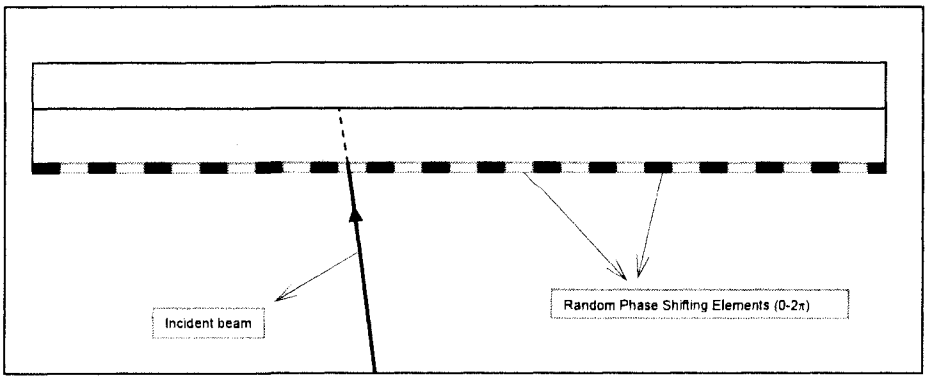

Fig.3.2. Scattering layer's simulation via technique A. Black and white elements in the picture are random phase shifting elements. Each element introduces a phase shift (0-2π) to any passing through beam.

Technique B: Ideal inner layer with inner curved boundary

To make the inner layer with a randomly curved boundary, first a 2D distribution of points ($\Delta x = 5-10mm$, $\Delta y = 1-4mm$) were chosen to make a rough view of the curved boundary. The next step was to fit the best curve possible (Smoothing Spline) to the points (Fig.3.2) and extract the function related to the curve. The function was then replaced in the main simulation as the curved boundary of the inner layer. When incident on its surface at any point, the beam would be refracted and partially reflected/transmitted due to the slope of the boundary at the point of incidence. This model represented a final and ideal simulation for scattering layer's inner boundary (Fig.3.3) and was used in both parts of the simulation (i.e. *part I* and *part II*) and experiment as will be discussed later.

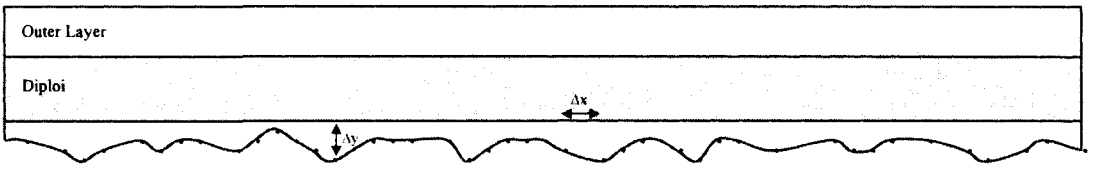

Fig.3.3. Final simulated skull layers. The inner boundary was developed as the best fitting curve to a dispersion of points randomly positioned in x and y direction ($\Delta x = 5-10mm$, $\Delta y = 1-4mm$). The fitting function then replaced in the main simulation as the inner boundary's equation to be able to find the slope at any point of incidence.

Acoustical properties of all elements used in final simulation are shown in Table 3.1 (all the values are taken for room temperature, i.e. 24°C).

Medium	Longitudinal Wave Velocity (m/s)	Transverse Wave Velocity (m/s)	Attenuation Factor (dB/m)	Density (kg/m^3)
Water	1489	N.A.*	180	1000
Inner layer	3098	2590	3400	1970
Diploi	2870	2240	3400	1770
Outer layer	2920	2960	3400	1930

Table3.1. Acoustical properties of water and scattering medium layers
*Shear waves do not exist in liquids.

	Element's Width	Total Size
Static object	$\lambda/2 = 0.44mm$	$6\lambda/2$=2.64mm
Random Phase Shifting Layer	$5\lambda - 7\lambda = 2.2 - 3.08mm$	$128\lambda/2$=56.32mm
Array of receivers	$\lambda/2 = 0.44mm$	56.32mm

Table.3.2. dimensional information on static object, random phase shifting layer and array of receivers

3.3.3. Array of Receivers

The array of receivers in Fig.3.1 was simulated as sequence of 128 small blocks (each $\lambda/2$=0.44mm in size, λ: wavelength in water). Each block is capable of saving the final phase and amplitude (and therefore Intensity) of the superposition of all incident beams.

3.4. Simulation Results for *part I*: Sound Intensity on the Array

Intensity Distribution on the array of receivers was calculated in absence and presence of the scattering medium.

3.4.1. Intensity Distribution *in Absence* of the Scattering Medium

To find the Intensity distribution on the array of receivers in absence of the scattering medium, an extended source (6 point sources separated by $\lambda/2$ along a straight line) was placed in the near field zone from the linear array of receivers. Each of the point sources on the static object then radiated a harmonic signal (frequency f=1.7 MHz) of unit amplitude. The linear receiving array consisted of 128 point receivers separated by $\lambda/2$ along a straight line. The acoustical field at the array could be calculated as a Frenel integral which in digital form can be written in a discrete form as

$$U_{array}(x_k)=\sum_{i=1}^{M}\frac{U_{i(obj)}(x_{io},y_{io})}{r_{ik}}\exp(jkr_{ik}+j\varphi_{io}-\alpha_w r_{ik}) \tag{3.2}$$

$$r_{ik}=\sqrt{(x_k-x_{io})^2+(y_k-y_{io}{}^2)} \tag{3.3}$$

Where M (=6) is the number of point sources used to make the extended source (static object); r_{ik} is the distance between the i^{th} element of the extended source and the k^{th} receiver on the array. x_k, y_k are the coordinates of the k^{th} receiver on the array, α_w is the attenuation coefficient in water, $k=\frac{2\pi}{\lambda}$ is the wave number ($\lambda=\frac{c}{f}$=0.88mm is the wavelength, $c=1500m/s$ is sound velocity in water and $f=1.7MHz$ is the signal frequency). Fig.3.4 shows the results of simulation for the extended source placed at the center of the array ($x_{10}=62\frac{\lambda}{2}-67\frac{\lambda}{2}=27.28-58.96mm$) at three different distances, i.e. half, same and twice the length of the receiving array.

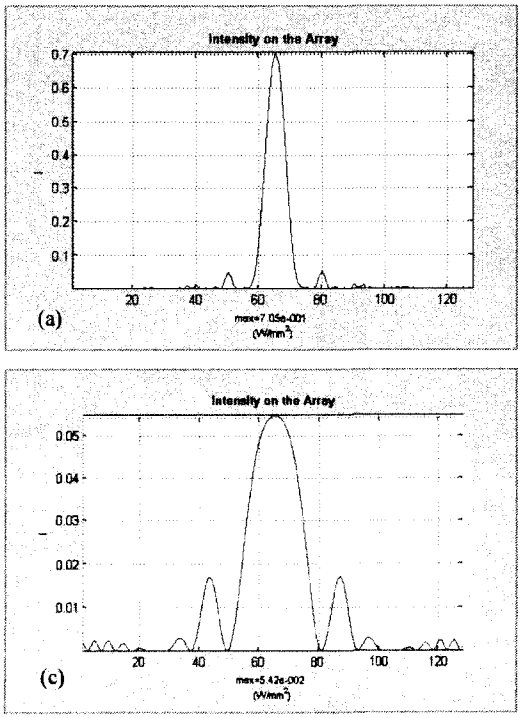

Fig3.4 Simulated intensity Distribution of received acoustical field on the array of receivers ***in absence*** of the scattering medium. The static object has been made by six point sources (separated by λ/2 along a straight line). The static object was placed at the center of the array in x direction, i.e. x_{io}=62λ/2-67λ/2. The distance between the static object and the array of receivers was a) y_o=64 λ/2=28.16mm, half of the length of the receiving array b) y_o=128 λ/2=56.32mm, the same as receiving array length, and c) y_o=256 λ/2=112.64mm, twice the length of the receiving array.

3.4.2. Intensity Distribution *in Presence* of the Scattering Medium

In the case in which the scattering medium was applied, two different algorithms were suggested to be used at the time. First algorithm assumed that there was no refraction in the scattering medium, which means that beams from static object reached the array of receivers in straight paths and only got attenuated due to the distance they take in water and each layer. Theoretical arrangements of a beam passes through the scattering medium (a close-up view of the area denoted by a dashed square in Fig.3.1) due to above mentioned algorithm for both inner layer techniques are shown in Fig.3.5.a and Fig.3.5.b.

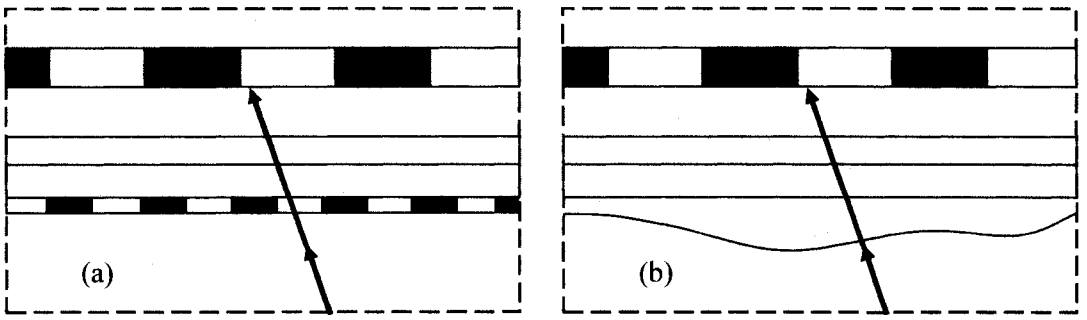

Fig.3.5 Theoretical arrangement of a beam transmits through the scattering medium (a close-up view of the area denoted by a dashed square in Fig.3.1) for (a) *Random phase shifting elements* technique and (b) *Ideal inner layer with inner curved boundary* technique

This time, in the same manner that Eq.(3.1) was calculated, the acoustical field at each element (subscripted by "k") on the array of receivers was calculated as

$$U_{array}(x_k)=\sum_{i=1}^{M}\frac{U_{i(obj)}(x_{io},y_{io})}{\sum_{l=1}^{L}r_{ik,l}}\exp\left[j\left(\sum_{l=1}^{L}(k_l r_{ik,l})+\varphi_{R.Layer}\right)-\sum_{l=1}^{L}(\alpha_l\cdot r_{ik,l})\right] \qquad (3.4)$$

For the *Random Phase Shifting Elements* technique, and

$$U_{array}(x_k)=\sum_{i=1}^{M}\frac{U_{i(obj)}(x_{io},y_{io})}{\sum_{l=1}^{L}r_{ik,l}}\exp\left[j\left(\sum_{l=1}^{L}(k_l r_{ik,l})\right)-\sum_{l=1}^{L}(\alpha_l\cdot r_{ik,l})\right] \qquad (3.5)$$

For the *Ideal inner layer with inner curved boundary* technique.

In Eq.(3.4) and Eq.(3.5) M is the number of point sources used to represent the static object, L is the number of possible mediums each could have propagated through, i.e. water and scattering medium layers, $r_{ik,l}$ is the path taken in water or any of the layers in the scattering medium when a beam initiates from the i^{th} point source on the static object and end in the k^{th} element on the array of receivers. α_l is the attenuation coefficient (Table 3.1) of either water or any of the flat layers in the scattering medium and $\varphi_{R.Layer}$ is the phase shift amount, in radians, of the phase shifting element through which a beam has been passed through. It is notable that in Eq.(3.4) $L=3$ ($l=1$: water, $l=2$: diploi, and $l=3$: outer layer in the scattering medium) and in Eq.(3.5) $L=4$ ($l=1$: water, $l=2$: Inner layer, $l=3$: diploi, and $l=4$: outer layer).

To get the intensity distribution on the array of receivers in presence of the scattering medium, the same apparatus of last part (where scattering medium had not been applied) was used. Scattering medium was then added to the apparatus in between the array of receivers and extended source ($3\lambda/2=1.32mm$ far from the array. This could be thought as the thickness of a human head skin) with its acoustical properties (Table 3.1) in the range of a real skull bone. The results for both inner layer techniques due to Eq.(3.4) and Eq.(3.5) are shown in Fig.3.6.a and Fig.3.6.b.

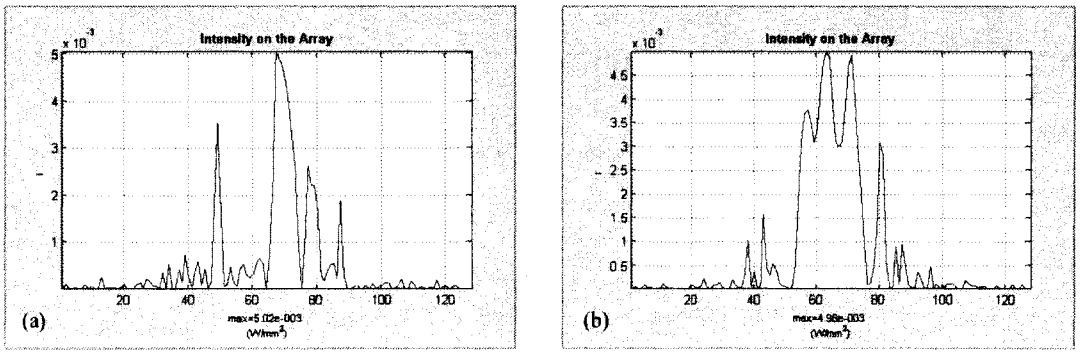

Fig.3.6 Simulated intensity distribution on the array of receivers ***in presence*** of the scattering medium using the ***refraction free*** algorithm for (a) *Random phase shifting elements* technique and (b) *Ideal inner layer with inner curved boundary* technique. The same extended source (static object) was placed at the center of the array of receivers ($x_{io}=62\lambda/2-67\lambda/2$) and $y_o=128\ \lambda/2=56.32$mm far from it.

On the other hand, the second algorithm was refraction included. A close-up view of the area denoted by a dashed square for this algorithm is shown in Fig.7. For clarity not all the possible beams inside the scattering medium and those who leave it are sketched.

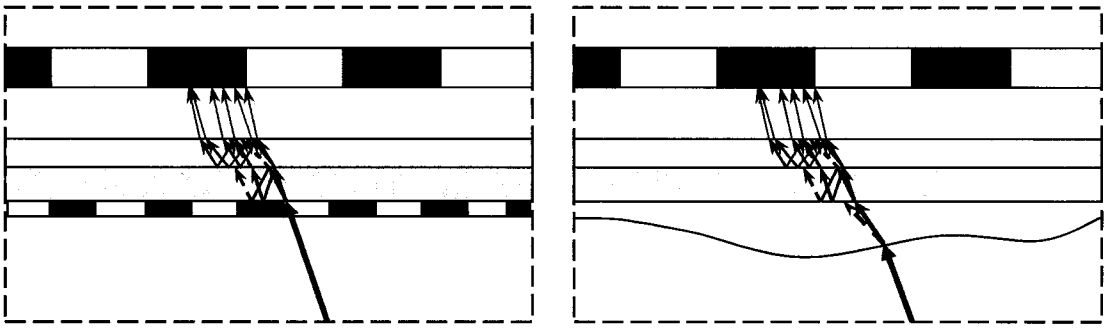

Fig.3.7. Theoretical arrangement of a beam passes through the scattering medium for refraction included algorithm (a close-up view of the area denoted by a dashed square in Fig.3.1) for (a) *Random phase shifting elements* technique and (b) *Ideal inner layer with inner curved boundary* technique. The red lines represent shear (transverse) beams and the blue lines represent longitudinal beams.

By taking into account refraction, transmission/reflection at the layers boundaries, distances each beam passes in the layer and attenuation loss at each layer, the acoustical field propagated through the scattering medium and received by the array was calculated. For each beam which reaches scattering medium surface, two modes could be generated in each layer if the incident angle (the angle between the norm and the direction of incident beam) had not been beyond their critical angles of incidence. Additionally, at each boundary, mode conversion could happen due to different transverse and longitudinal wave velocities in each layer. Snell's Law and critical angle restriction had been applied. Due to high attenuation in scattering medium, beams which had more than two reflections in each layer were too weak to be detected from the experimental point of view. Therefore only beams with maximum two reflections in each layer played role in the simulation. Again acoustical field on the array of receivers was calculated for both inner layer techniques. For instance, for a beam reflected twice in each of the layers the acoustical field distribution at each point (x_k) on the array derived from

$$U_{array}(x_k)=\sum_{i=1}^{M}\left(\prod_{l=1}^{L}(T_{l-1,l}\cdot R_{l+1,l}\cdot R_{l-1,l})\frac{U_{i(obj)}(x_{io},y_{io})}{\sum_{l=1}^{L}r_{ik,l}}\exp\left[j\left(\sum_{l=1}^{L}(k_l r_{ik,l})+\varphi_{R.Layer}\right)-\sum_{l=1}^{L}(\alpha_l\cdot r_{ik,l})\right]\right) \tag{3.6}$$

For the *Random Phase Shifting Elements* technique, and

$$U_{array}(x_k)=\sum_{i=1}^{M}\left(\prod_{l=1}^{L}(T_{l-1,l}\cdot R_{l+1,l}\cdot R_{l-1,l})\frac{U_{i(obj)}(x_{io},y_{io})}{\sum_{l=1}^{L}r_{ik,l}}\exp\left[j\left(\sum_{l=1}^{L}(k_l r_{ik,l})\right)-\sum_{l=1}^{L}(\alpha_l\cdot r_{ik,l})\right]\right) \tag{3.7}$$

For the *Ideal inner layer with inner curved boundary* technique.

Again, In Eq.(3.6) and Eq.(3.7), M is the number of point sources used to represent the static object, L is the number possible mediums for each propagating beam, i.e. water and scattering medium layers, $r_{ik,l}$ is the path taken in water or any of the layers in the scattering medium when a beam initiates from the i^{th} point source on the static object and end in the k^{th} element on the array of receivers. α_l is the attenuation factor of either water or any of the flat layers in the scattering medium and $\varphi_{R.Layer}$ is the phase shift amount, in radians, of the phase shifting element through which a beam has been passed. It is notable that $L=3$ in Eq.(3.6) ($l=1$: water, $l=2$: diploi, and $l=3$: outer layer in the scattering medium) and $L=4$ in Eq.(3.7) ($l=1$: water, $l=2$: Inner layer, $l=3$: diploi, and $l=4$: outer layer)., $T_{l-1,l}$ and $R_{l-1,l}$ are related transmission and reflection coefficients (taken from chapter 2 section 2.3) at the boundary of the $(l-1)^{th}$ and l^{th} layers. Z_l is the impedance of the l^{th} layer, c_l and ρ_l are sound velocity and density of the l^{th} layer respectively, and θ_l could be angle of incidence or refraction accordingly. The results for

both inner layer techniques due to Eq.(3.6) and Eq.(3.7) are shown in Fig.3.8.a and Fig.3.8.b.

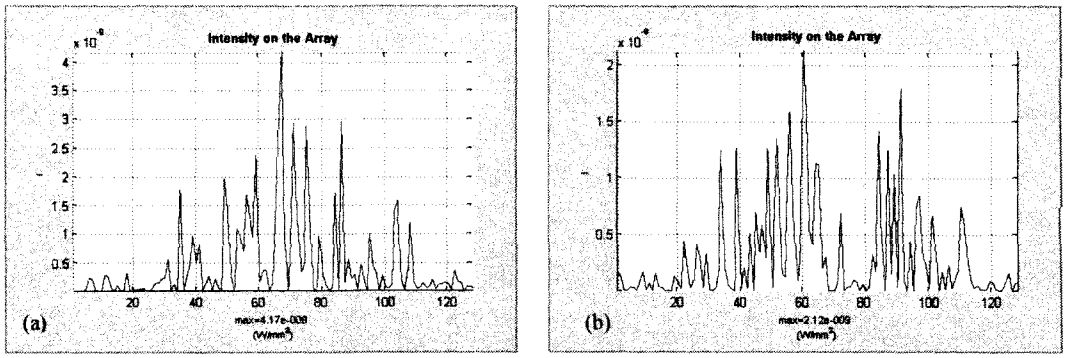

Fig.3.8 Simulated intensity distribution on the array of receivers ***in presence*** of the scattering medium using the ***refraction included*** algorithm for (a) *Random phase shifting elements* technique and (b) *Ideal inner layer with inner curved boundary* technique. ***Only twice reflected then transmitted*** beams in each layer played role in the simulation. Significant power loss, compared to other Intensity distribution graphs (~10^{-5} times), was observed due to multiple reflections in the layers. The same extended source (static object) was placed at the center of the array of receivers (x_{io}=62λ/2-67λ/2) and y_o=128 λ/2=56.32mm far from it.

By the same token, as another example, acoustical field (Fig.3.9.g and Fig.3.9.h) on the array of receivers for a beam directly reaches the array of receivers with no reflection in the layer (all way transmitted) was calculated as

$$U_{array}(x_k)=\sum_{i=1}^{M}\left(\prod_{l=1}^{L}(T_{l-1,l})\frac{U_{i(obj)}(x_{io},y_{io})}{\sum_{l=1}^{L}r_{ik,l}}\exp\left[j\left(\sum_{l=1}^{L}(k_l r_{ik,l})+\varphi_{R.Layer}\right)-\sum_{l=1}^{L}(\alpha_l\cdot r_{ki,l})\right]\right) \quad (3.8)$$

For the *Random Phase Shifting Elements* technique, and

$$U_{array}(x_k)=\sum_{i=1}^{M}\left(\prod_{l=1}^{L}(T_{l-1,l})\frac{U_{i(obj)}(x_{io},y_{io})}{\sum_{l=1}^{L}r_{ik,l}}\exp\left[j\left(\sum_{l=1}^{L}(k_l r_{ik,l})\right)-\sum_{l=1}^{L}(\alpha_l\cdot r_{ki,l})\right]\right) \quad (3.9)$$

For the *Ideal inner layer with inner curved boundary* technique. Results are shown in Fig3.9.a and Fig.3.9.b.

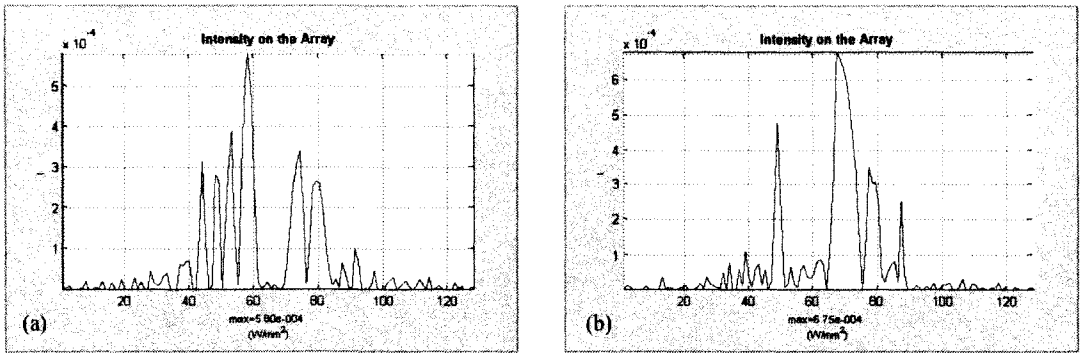

Fig.3.9 Simulated intensity distribution on the array of receivers ***in presence*** of the scattering medium using the ***refraction included*** algorithm for (a) *Random phase shifting elements* technique and (b) *Ideal inner layer with inner curved boundary* technique. ***Only all way transmitted*** beams in each layer played role in the simulation. The same extended source (static object) was placed at the center of the array of receivers (x_{io}=62λ/2-67λ/2) and y_o=128 λ/2=56.32mm far from it.

In the same way, all possible combinations of mode conversion and reflection/transmission (up to two reflections in each layer) have been found and applied into the simulation. Characteristic final calculated intensities on the array of receivers for both inner layer techniques are shown in Fig.3.10.a and Fig.310.b.

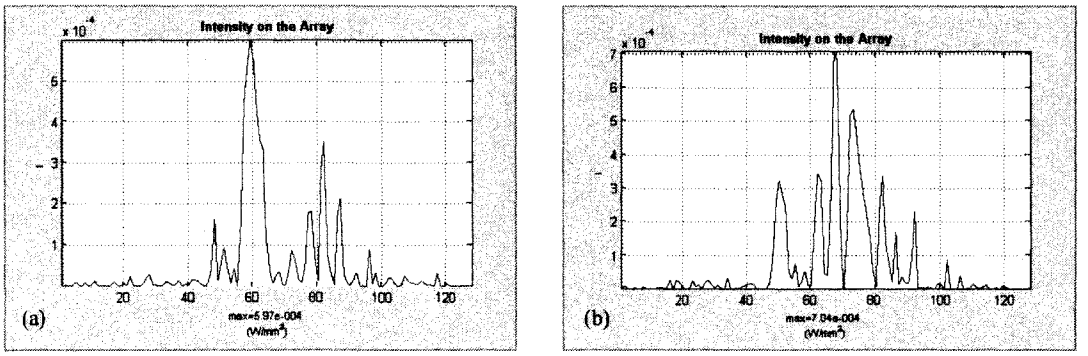

Fig.3.10 ***Final*** Simulated intensity distribution on the array of receivers ***in presence*** of the scattering medium using the ***refraction included*** algorithm for (a) *Random phase shifting elements* technique and (b) *Ideal inner layer with inner curved boundary* technique. The same extended source (static object) was placed at the center of the array of receivers (x_{io}=62λ/2-67λ/2) and y_o=128 λ/2=56.32mm far from it.

To see how multiple reflections in the layer affect the final distribution on the array, it was required to make a comparison between the maximum intensity level on the array of receivers for one of the final comprehensive distributions (Fig.3.10.a or Fig.3.10.b) and one of those which only were twice reflected then transmitted beams included (Fig3.8.a

or Fig3.8.b). As can be seen from the figures, multiple reflections caused enormous power loss in the field. A characteristic maximum intensity level of twice reflected beams was found to be 4.17×10^{-9} while it was measured 5.97×10^{-4} for the whole beams package. This means that, in future studies, multiple reflected beams can be safely neglected as they showed to be too small in final amplitude to have a significant affect on the intensity distribution.

3.5. Simulation results for *part II*: Image reconstruction

3.5.1. Theoretical Considerations

After finding the intensity distribution on the array of receivers, the next step was to reconstruct an image of the original source of the field. In addition to its size, the image should have contained information about the exact coordinates of the static object. As mentioned before, all elements on the array of receivers simulated in a way to be capable of recording the final amplitude and phase of superposition on the beams they had received. The main part of our theory developed at this stage due to Matched Filtering Method and, to be more precise, by taking advantage of Time Reversal Mirror (TRM) method as they explained in section 1.1.

To reconstruct the original acoustical field by only using the distorted field distribution on the array of receivers, we supposed that each receiver starts to generate its own field (like a point source) in the reversed direction with its initial phase and amplitude the same as what it had saved from *Part I.* So, this time instead of a small number of point sources, 128 point sources produce acoustical field at the same time in the reverse direction. A theoretical arrangement is shown in Fig.3.11. The field then penetrates into the scattering medium from the outer layer. Both the *refraction included* and *refraction free* algorithms were applied to the scattering medium. After leaving the scattering medium, a superposition of all incident waves at each point of a vertical mesh grid in the *array of receivers-simulated skull* plane was calculated and saved. As predicted in the theory, the superposition of the reverse propagating waves was in a way

that the final plot of the field intensity on the mentioned mesh plane, showed a major peak at the original static object's position. The preciseness, mathematical formulation and final results of each algorithm are discussed in the remainder of this chapter.

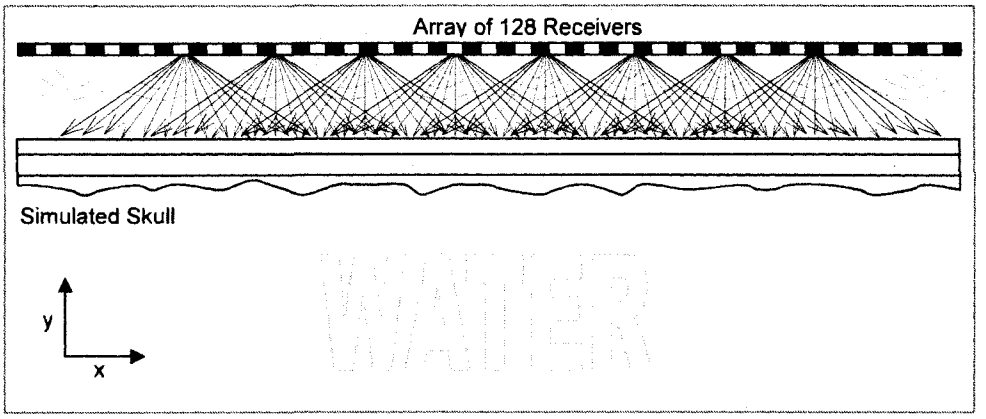

Fig.3.11. Theoretical arrangement of the *Image Reconstruction* part of the simulation.

Just as in *part I*, the results were generated in the absence and presence of the scattering medium.

3.5.2. Image Reconstruction *in Absence* of the Scattering Medium

In absence of the scattering medium, the reconstructed field at 128 by 300 discrete points (also called *image plane* from now on) was calculated in the same manner as Eq.(3.2) with a negative value for the angular part as the waves are propagation in the reverse direction

$$U_{image}(x',y') = \sum_{k=1}^{N} \frac{U_{array}(x_k, y_k)}{r_k'} \exp(-j\varphi_{0k} - jkr_k') \tag{3.10}$$

$$r_k' = \sqrt{(x_k - x')^2 + (y_k - y')^2} \tag{3.11}$$

In Eq.(3.10) and Eq.(3.11), (x', y') is the coordinate of the point in image plane in which the reversed field is being calculated. (x_k, y_k) is the coordinate of the k^{th} receiver on the

array of receivers. N(=128) is the number of receivers on the array of receivers. U_{array} and φ_{0k} are the saved amplitude and phase (from *part I*) of the k^{th} receiver on the array of receivers respectively which are now being used as its *initial* amplitude and phase.

The first reconstructions were done in absence of the scattering medium for the three intensity distributions from the previous section (Fig.3.4). The original static objects were placed at the center of the array ($x_{i0} = 62\frac{\lambda}{2} - 67\frac{\lambda}{2} = 27.28 - 58.96mm$) at three different distances, i.e. half, the same and twice the length of the receiving array. The results are shown in figures 3.12.a, 3.13.a and 3.14.a at the end of this chapter.

The "b" parts of the figures are the same as the graphs in Fig.3.4. The figures also contain two other graphs named as *Vertical and Horizontal Profiles.* Vertical and horizontal cross-sections of the main peak in Vertical Image Planes are shown in those parts of the figures. The peak's widths are also mentioned at the level of 0.7 of maximum intensity.

Comparing the "vertical image planes" of figures 3.12, 3.13 and 3.14, some other information about the resolution of the image can also be obtained. It can be seen that as the static object gets farther from the array of receivers, the resolution decreases in the reconstructed image plane. This could be explained due to change in resolution element size in y direction. The resolution element in y direction is defined as

$$dy'' = \frac{\lambda Y}{D} \qquad (3.12)$$

Where D is the size of the array and Y is the distance in between the resolution element and array of receivers. As Y increases, also dy'' increases which results in less final resolution. For example, in Fig.3.12 as $Y = D/2 = (128\lambda/2)/2 = 28.16mm$, $dy'' = \lambda/2 = 0.44mm$. By the same token, $dy'' = \lambda = 0.88mm$ in Fig.3.13, and $dy = 2\lambda'' = 1.76mm$ in Fig.3.14.

3.5.3. Image Reconstruction *in Presence* of the Scattering Medium

After applying the scattering medium, in the same manner that Eq.(3.10) was derived from Eq.(3.2), reconstruction fields' formulas were developed for all other cases mentioned in *part I.*

In *refraction free* algorithm (Fig.3. and Fig.3.) the reconstructed field at each point of the *image plane* due to Eq.(3.10) and Eq.(3.11) was calculated as

$$U_{image}(x',y')=\sum_{k=1}^{N}\frac{U_{k-array}(x_k,y_k)}{\sum_{l=1}^{L}r'_{k,l}}\exp\left[-j\left(\sum_{l=1}^{L}(k_l r'_{k,l})+\varphi_{R.Layer}\right)-j\varphi_{ok}+\sum_{l=1}^{L}(\alpha_l\cdot r'_{k,l})\right] \quad (3.13)$$

For the *Random Phase Shifting Elements* technique (Fig.3.2), and

$$U_{image}(x',y')=\sum_{k=1}^{N}\frac{U_{k-array}(x_k,y_k)}{\sum_{l=1}^{L}r'_{k,l}}\exp\left[-j\left(\sum_{l=1}^{L}(k_l r'_{k,l})\right)-j\varphi_{ok}+\sum_{l=1}^{L}(\alpha_l\cdot r'_{k,l})\right] \quad (3.14)$$

For the *Ideal inner layer with inner curved boundary* technique (Fig.3.3).

In Eq.(3.13) and Eq.(3.14), $r'_{k,l}$ is the path taken by each beam in the l^{th} medium (either water or any of the layers in the scattering medium). Again it should be noticed that in Eq.(3.13) $L=3$ and in Eq.(3.14) $L=4$. The results are shown in Fig.3.15 and Fig.3.16 (at the end of this chapter).

On the other hand, in *refraction Included* algorithm (Fig.3.7.a and Fig.3.7.b) the reconstructed field at each point of the *image plane* for only twice reflected beams in each layer (as an example) due to Eq.(3.6) and Eq.(3.7) was calculated as

$$U_{array}(x_k)=\sum_{k=1}^{N}\left(\prod_{l=1}^{L}(T_{l-1,l}\cdot R_{l+1,l}\cdot R_{l-1,l})\frac{U_{k-array}(x_k,y_k)}{\sum_{l=1}^{L}r'_{k,l}}\exp\left[-j\left(\sum_{l=1}^{L}(k_l r'_{k,l})+\varphi_{R\,Layer}\right)-j\varphi_{ok}+\sum_{l=1}^{L}(\alpha_l\cdot r'_{k,l})\right]\right) \tag{3.17}$$

For the *Random Phase Shifting Elements* technique (Fig.3.2), and

$$U_{array}(x_k)=\sum_{k=1}^{N}\left(\prod_{l=1}^{L}(T_{l-1,l}\cdot R_{l+1,l}\cdot R_{l-1,l})\frac{U_{k-array}(x_k,y_k)}{\sum_{l=1}^{L}r'_{k,l}}\exp\left[-j\left(\sum_{l=1}^{L}(k_l r'_{k,l})\right)-j\varphi_{ok}+\sum_{l=1}^{L}(\alpha_l\cdot r'_{k,l})\right]\right) \tag{3.18}$$

For the *Ideal inner layer with inner curved boundary* technique (Fig.3.3). The results are shown in Fig.3.17 and Fig.3.18.

Finally, following the same procedure, image reconstructions for the intensity distributions of only single reflected beams (Fig.3.19 and Fig.3.20) and also image reconstructions for the intensity distributions of the final comprehensive package of possible beams (Fig.3.21 and Fig.3.22) were executed in the program and the results are presented.

A comparison has been made between the original and reconstructed coordinates of the extended sources through all aforementioned algorithms and techniques in Table 3.3.

Distance from the array of receivers	Original Position	Maximum Position
In absence of the scattering medium (figures 3.12, 3.13 and 3.14)		
28.16 mm	x_{io}=62-67 pixs. y_o=64 pix.	x_{io}=64 pix. y_o=64 pix.
56.32 mm	x_{io}=62-67 pixs. y_o=128 pix.	x_{io}=64 pix. y_o=128 pix.
112.64 mm	x_{io}=62-67 pixs. y_o=256 pix	x_{io}=64 pix. y_o=255 pix.
In presence of the scattering medium- **refraction free** algorithm (figures 3.15 and 3.16)		
56.32 mm technique I	x_{io}=62-67 pixs. y_o=128 pix.	x_{io}=62 pix. y_o=130 pix.
56.32 mm technique II	x_{io}=62-67 pixs. y_o=128 pix.	x_{io}=61 pix. y_o=132 pix.
In presence of the scattering medium- **refraction included** algorithm only **all way transmitted** beams (figures 3.19 and 3.20)		
56.32 mm technique I	x_{io}=62-67 pixs. y_o=128 pix.	x_{io}=63 pix. y_o=127 pix.
56.32 mm technique II	x_{io}=62-67 pixs. y_o=128 pix.	x_{io}=65 pix. y_o=127 pix.
In presence of the scattering medium- **refraction included** algorithm only **twice** reflected beams (figures 3.17 and 3.18)		
56.32 mm technique I	x_{io}=62-67 pixs. y_o=128 pix.	x_{io}=65 pix. y_o=123 pix.
56.32 mm technique II	x_{io}=62-67 pixs. y_o=128 pix.	x_{io}=68 pix. y_o=134 pix.
In presence of the scattering medium- **refraction included** algorithm- **Final** (figures 3.21 and 3.22)		
56.32 mm technique I	x_{io}=62-67 pixs. y_o=128 pix.	x_{io}=62 pix. y_o=130 pix.
56.32 mm technique II	x_{io}=62-67 pixs. y_o=128 pix.	x_{io}=62 pix. y_o=130 pix.

Table3.3. Original and reconstructed coordinates of the extended source in all aforementioned conditions. 1pix.=$\lambda/2$=0.44mm. technique I: Random phase shifting elements. Technique II: Ideal inner layer with curved boundary.

3.6. Conclusion

It can be seen from the table.3.3 that in absence of the scattering medium the simulation predicted the static object's position with a high accuracy. The reconstructed coordinates are almost the same as original coordinates in all three cases.

It could also be concluded that between the refraction included methods the comprehensive *refraction included* algorithms made the most accurate predictions about the original position of the static object (2pixs=0.88mm deviation from the original position). The less accurate prediction was made when only twice reflected beam took part in the simulation. This was predictable as the majority of the beams were eliminated from the simulation.

Another interesting conclusion from the table.3.3 was that in the case that only all way transmitted beams were used in the simulation, the reconstruction results was reasonably accurate (~5pixs=2.2 mm). This could be explained by the fact that multiple reflected beams were much too week to be able to significantly affect the distribution on the array of receivers and the reconstruction results.

Furthermore, making decision about the preciseness of the two algorithms (*refraction free* and *refraction included*) needs the experimental results and will be discussed in next chapter. On the other hand, some conclusions could be made up by comparing the reconstruction results from Table.3.3.

During the next chapter real experimental data will be replaced in the simulation and the effectiveness of the simulation will be evaluated.

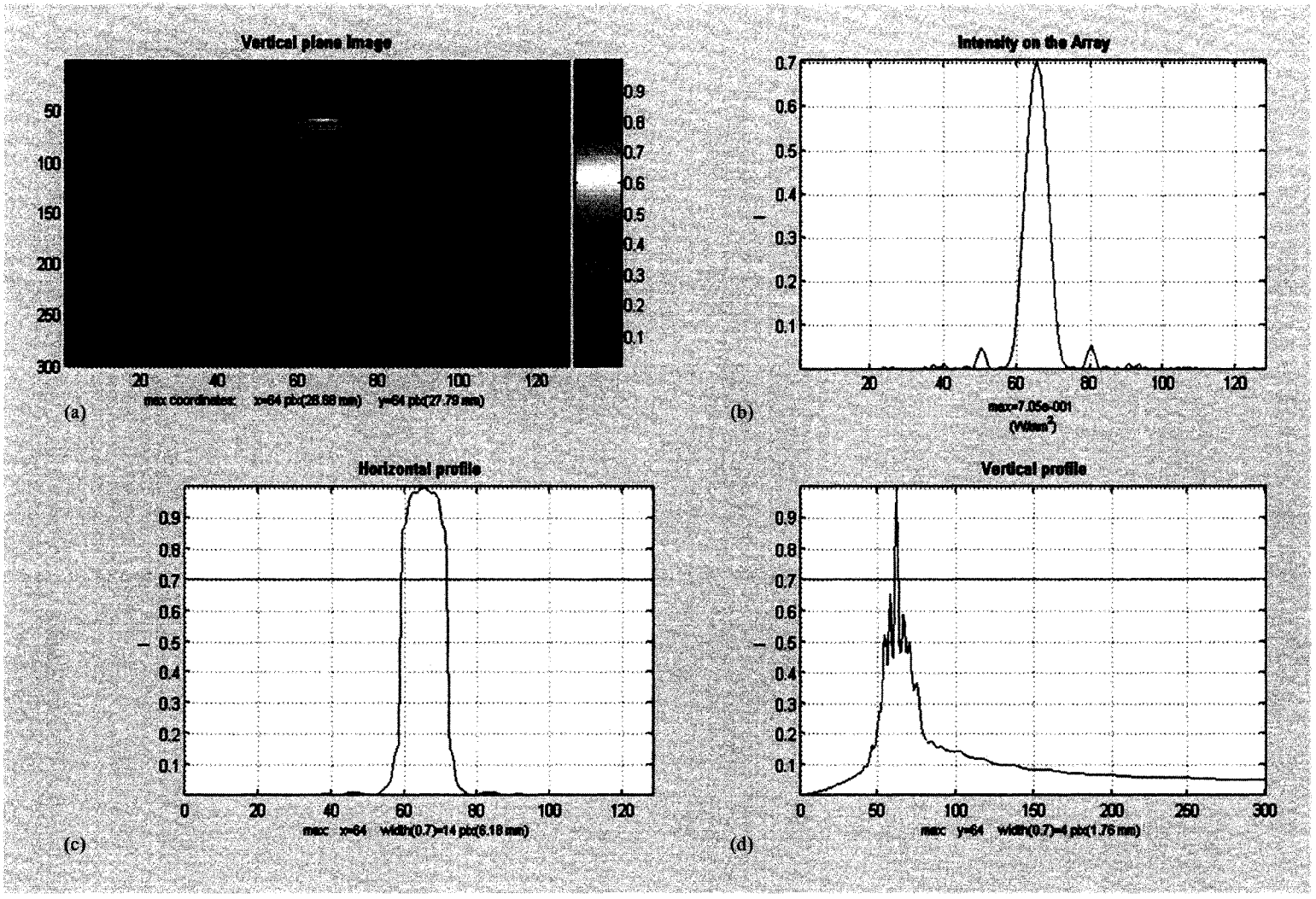

Fig.3.12 (a) Reconstructed image of the reversed field ***in absence*** of the scattering medium using the same Intensity distribution in Fig.3.4.a. the original static object had been placed at $x_{io}=62\lambda/2-67\lambda/2$ and $y_o=64\ \lambda/2$. the reconstructed image also showed a major peak exactly at the same place. (b) Intensity distribution in Fig.3.4.a (c) Horizontal Profile of the major peak in Vertical Plane Image. (d) Vertical Profile of the major peak in Vertical Plane Image. Peak's widths in both x and y direction are also mentioned at the bottom.

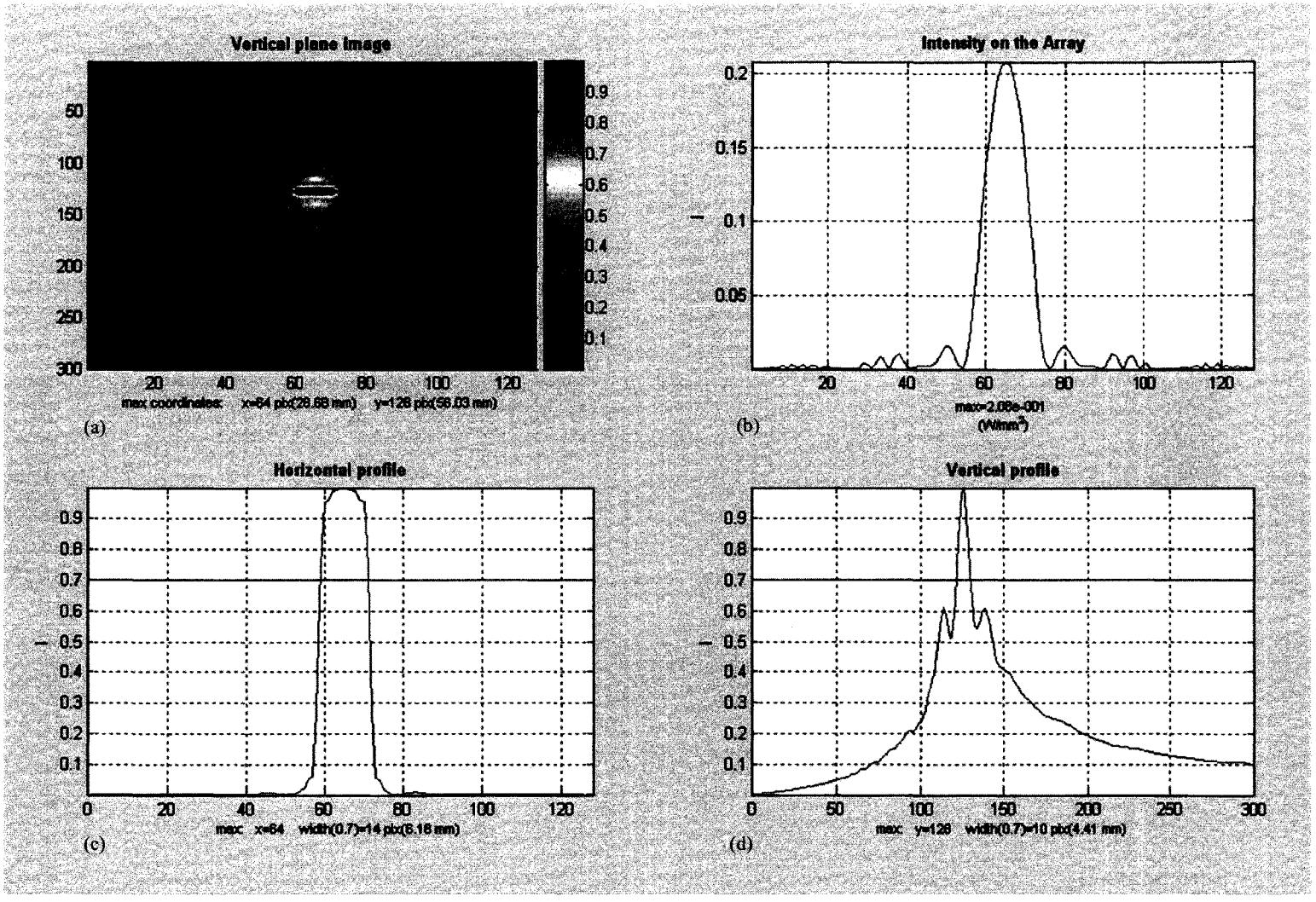

Fig.3.13 (a) Reconstructed image of the reversed field ***in absence*** of the scattering medium using the same Intensity distribution in Fig.3.4.b. the original static object had been placed at $x_{io}=62\lambda/2\text{-}67\lambda/2$ and $y_o=128\ \lambda/2$. the reconstructed image also showed a major peak exactly at the same place. (b) Intensity distribution in Fig.3.4.b (c) Horizontal Profile of the major peak in Vertical Plane Image. (d) Vertical Profile of the major peak in Vertical Plane Image.

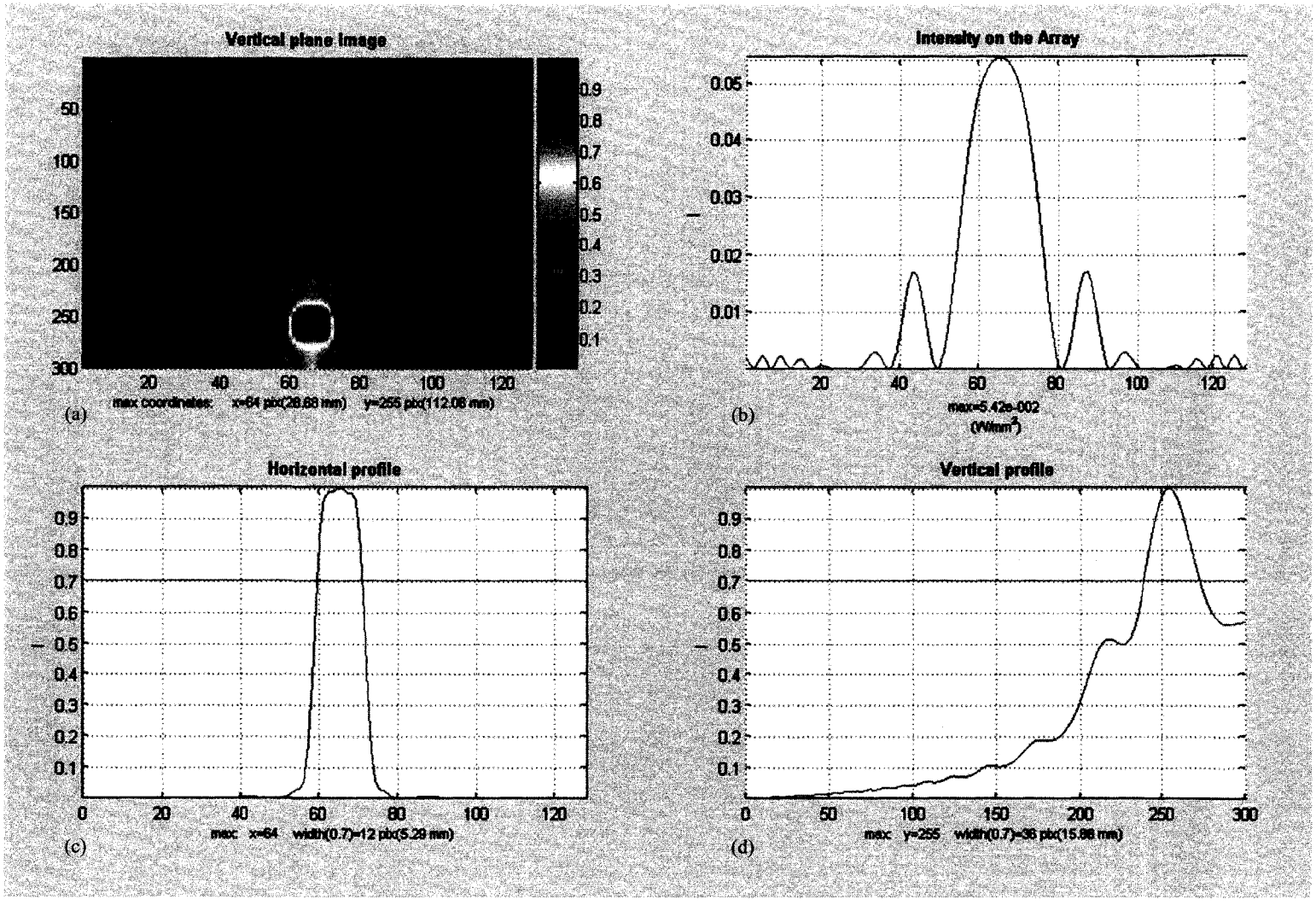

Fig.3.14 (a) Reconstructed image of the reversed field ***in absence*** of the scattering medium using the same Intensity distribution in Fig.3.4.c. the original static object had been placed at $x_{io}=62\lambda/2-67\lambda/2$ and $y_o=256\ \lambda/2$. The reconstructed image also showed a major peak exactly at the same place. (b) Intensity distribution in Fig.3.4.b (c) Horizontal Profile of the major peak in Vertical Plane Image. (d) Vertical Profile of the major peak in Vertical Plane Image.

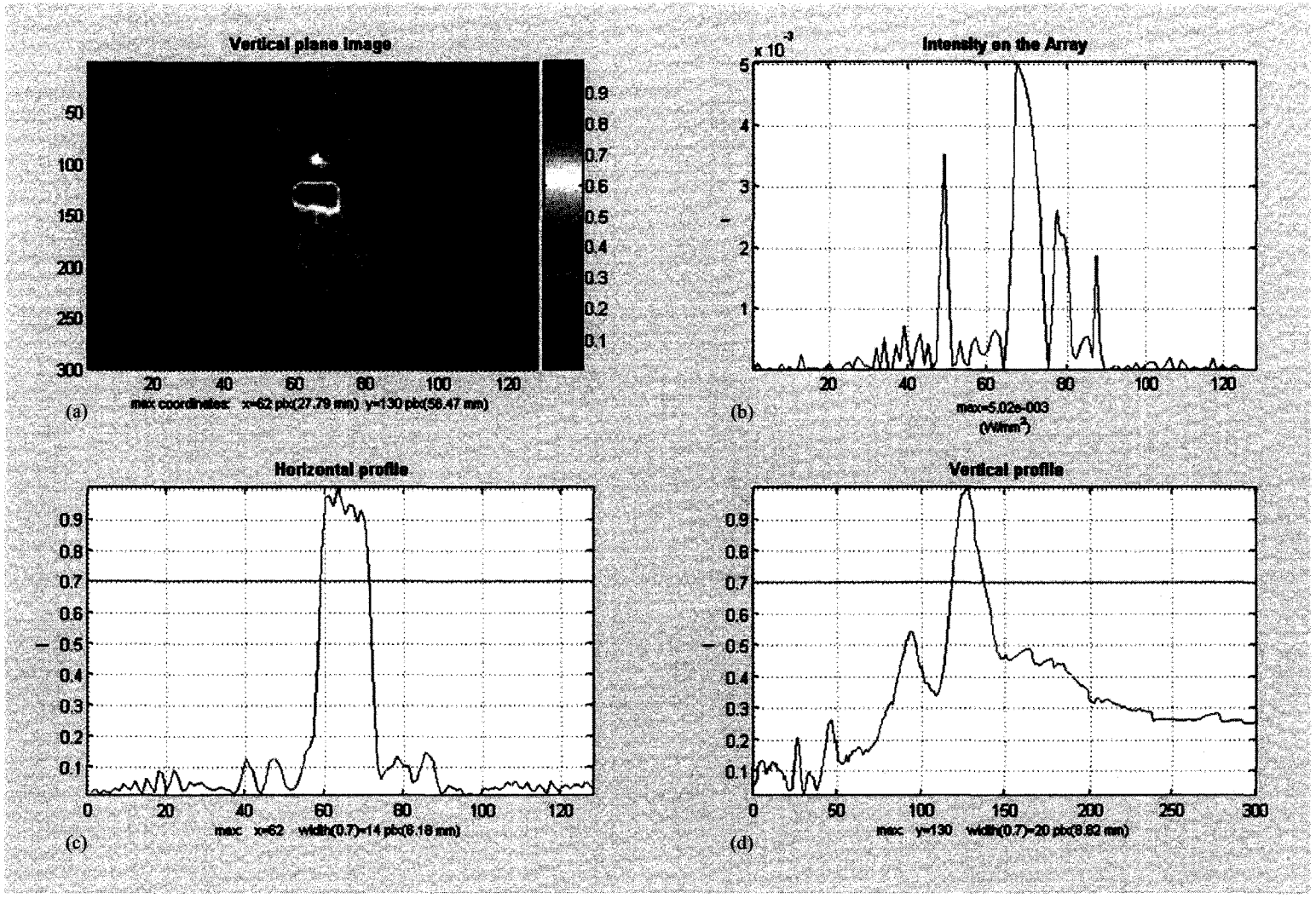

Fig.3.15 (a) Reconstructed image of the reversed field ***in presence*** of the scattering medium for the same Intensity distribution in Fig.3.6.a using the ***refraction free*** algorithm. The original static object had been placed at $x_{io}=62\lambda/2\text{-}67\lambda/2$ and $y_o=128\ \lambda/2$. The reconstructed image also showed a major peak *almost* at the same place. (b) Intensity distribution in Fig.3.6.a (c) Horizontal Profile of the major peak in Vertical Plane Image. (d) Vertical Profile of the major peak in Vertical Plane Image. The inner layer of the scattering medium in this reconstruction was designed using ***Random phase shifting elements*** technique.

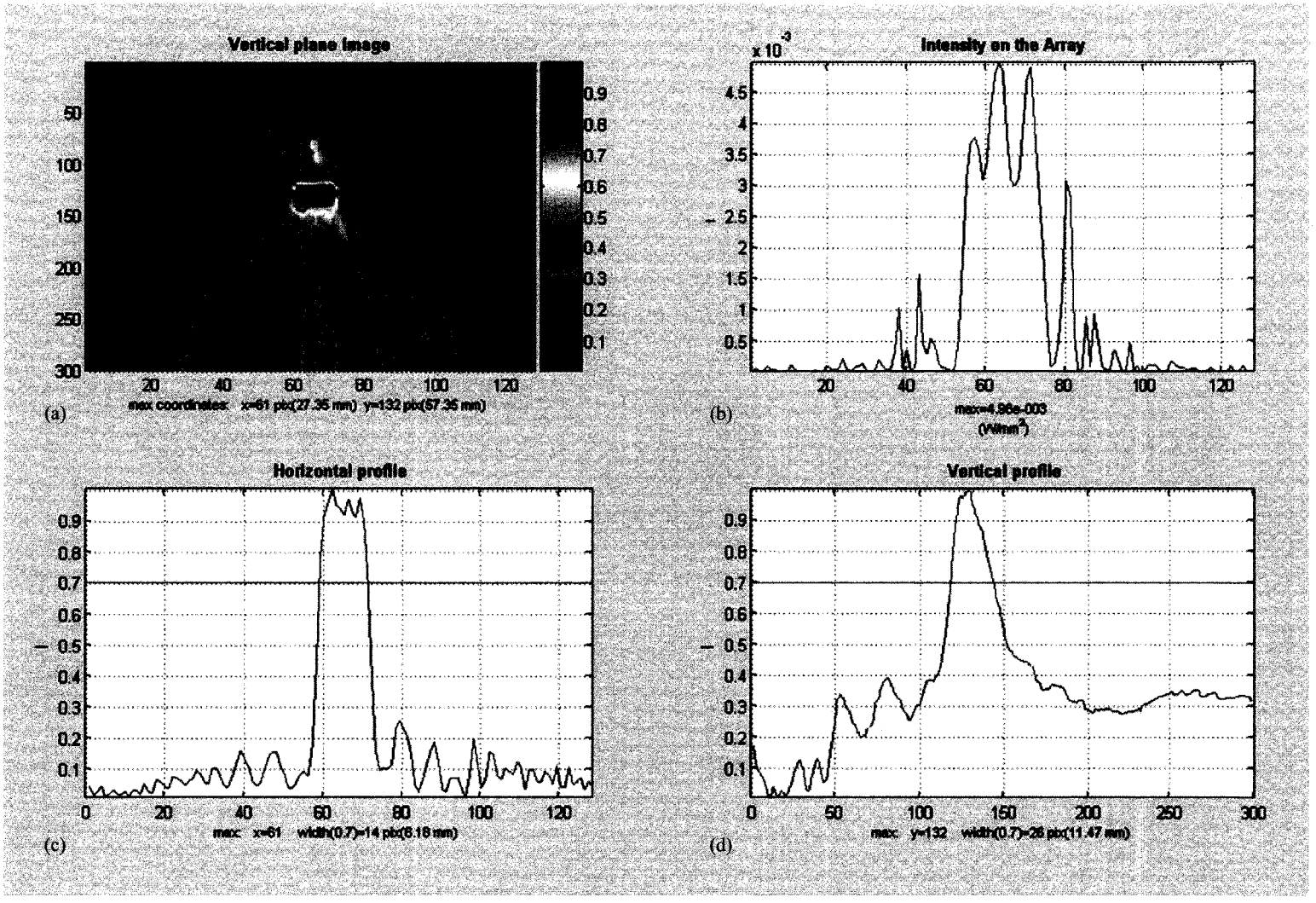

Fig.3.16 (a) Reconstructed image of the reversed field ***in presence*** of the scattering medium for the same Intensity distribution in Fig.3.6.b using the ***refraction free*** algorithm. The original static object had been placed at $x_{io}=62\lambda/2\text{-}67\lambda/2$ and $y_o=128\ \lambda/2$. The reconstructed image also showed a major peak *almost* at the same place. (b) Intensity distribution in Fig.3.6.b (c) Horizontal Profile of the major peak in Vertical Plane Image. (d) Vertical Profile of the major peak in Vertical Plane Image. The inner layer of the scattering medium in this reconstruction was designed using ***Ideal inner layer with inner curved boundary*** technique.

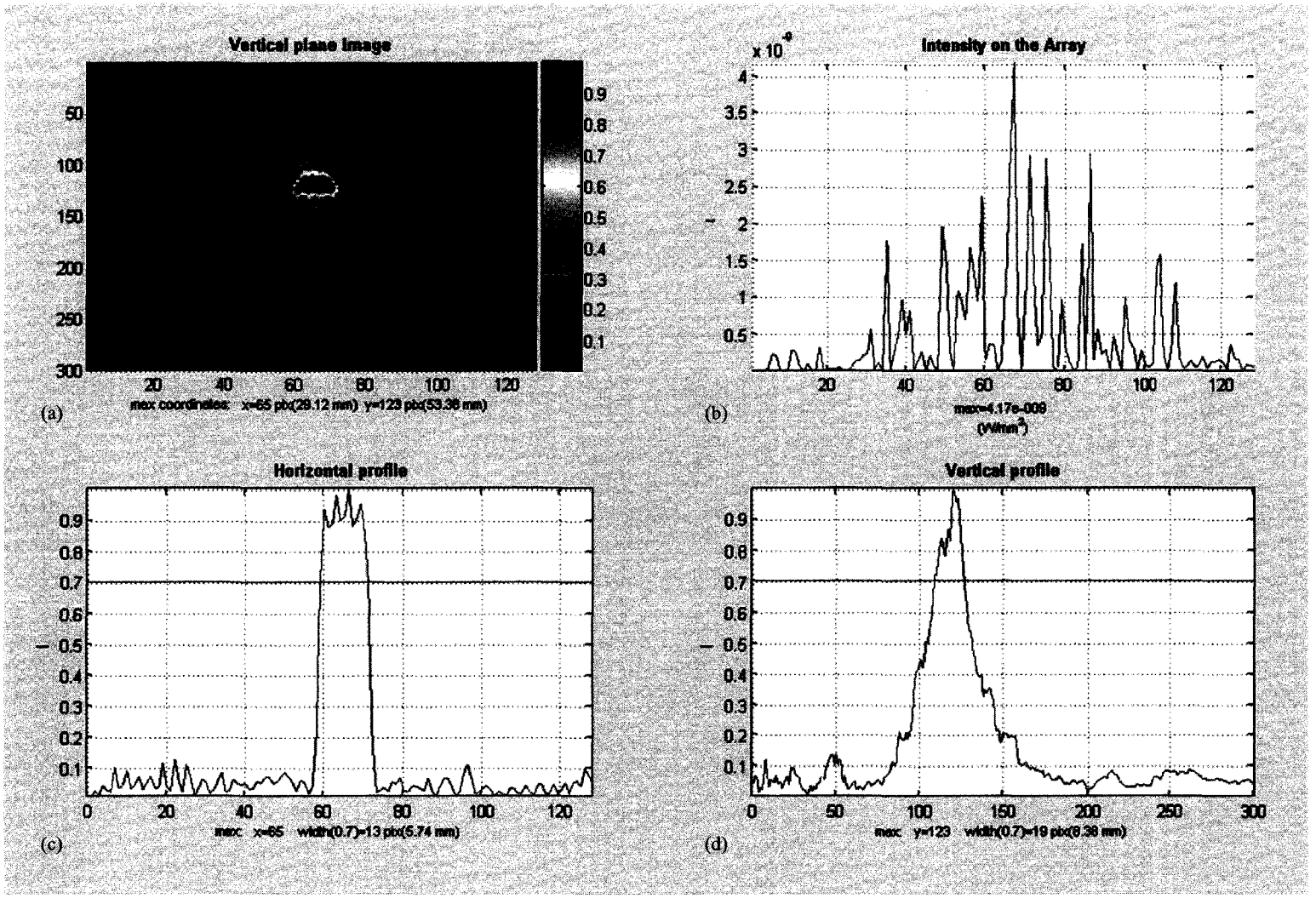

Fig.3.17 (a) Reconstructed image of the reversed field ***in presence*** of the scattering medium for the same Intensity distribution in Fig.3.8.a using the ***refraction included*** algorithm. ***Only twice reflected*** beams in each layer was inserted in the reconstruction process. The original static object had been placed at $x_{io}=62\lambda/2\text{-}67\lambda/2$ and $y_o=128\ \lambda/2$. The reconstructed image also showed a major peak a bit off the expected coordinates. (b) Intensity distribution in Fig.3.8.a (c) Horizontal Profile of the major peak in Vertical Plane Image. (d) Vertical Profile of the major peak in Vertical Plane Image. The inner layer of the scattering medium in this reconstruction was designed using ***Random phase shifting elements*** technique.

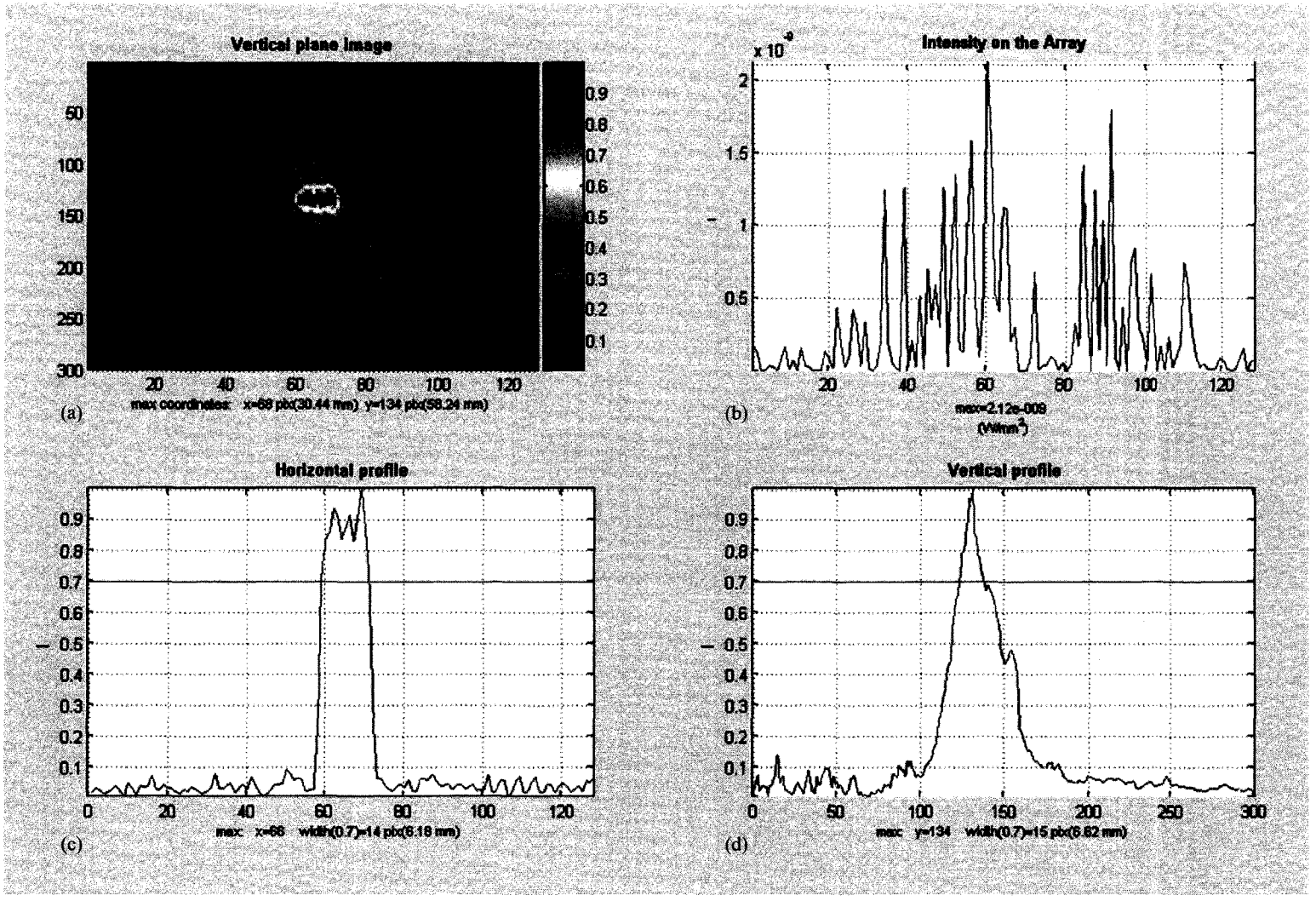

Fig.3.18 (a) Reconstructed image of the reversed field ***in presence*** of the scattering medium for the same Intensity distribution in Fig.3.8.b using the ***refraction included*** algorithm. ***Only twice reflected*** beams in each layer was inserted in the reconstruction process. The original static object had been placed at $x_{io}=62\lambda/2\text{-}67\lambda/2$ and $y_o=128\ \lambda/2$. The reconstructed image also showed a major peak a bit off the expected coordinates. (b) Intensity distribution in Fig.3.8.b (c) Horizontal Profile of the major peak in Vertical Plane Image. (d) Vertical Profile of the major peak in Vertical Plane Image. The inner layer of the scattering medium in this reconstruction was designed using ***Ideal inner layer with inner curved boundary*** technique.

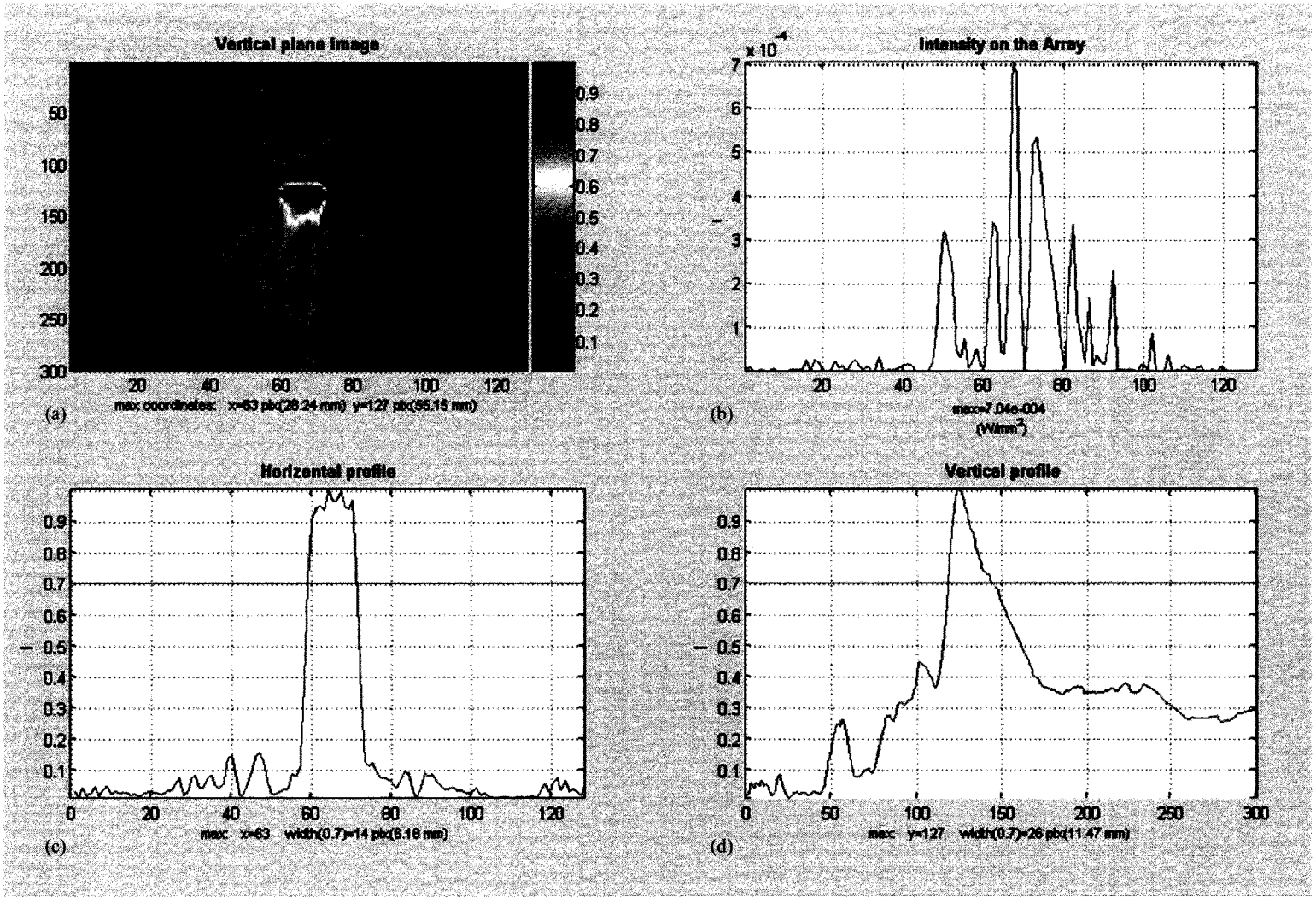

Fig.3.19 (a) Reconstructed image of the reversed field ***in presence*** of the scattering medium for the same Intensity distribution in Fig.3.9.a using the ***refraction included*** algorithm. ***Only all way transmitted*** beams in each layer was inserted in the reconstruction process. The original static object had been placed at $x_{io}=62\lambda/2\text{-}67\lambda/2$ and $y_o=128\ \lambda/2$. The reconstructed image also showed a major peak *almost* at the same place. (b) Intensity distribution in Fig.3.9.a (c) Horizontal Profile of the major peak in Vertical Plane Image. (d) Vertical Profile of the major peak in Vertical Plane Image. The inner layer of the scattering medium in this reconstruction was designed using ***Random phase shifting elements*** technique.

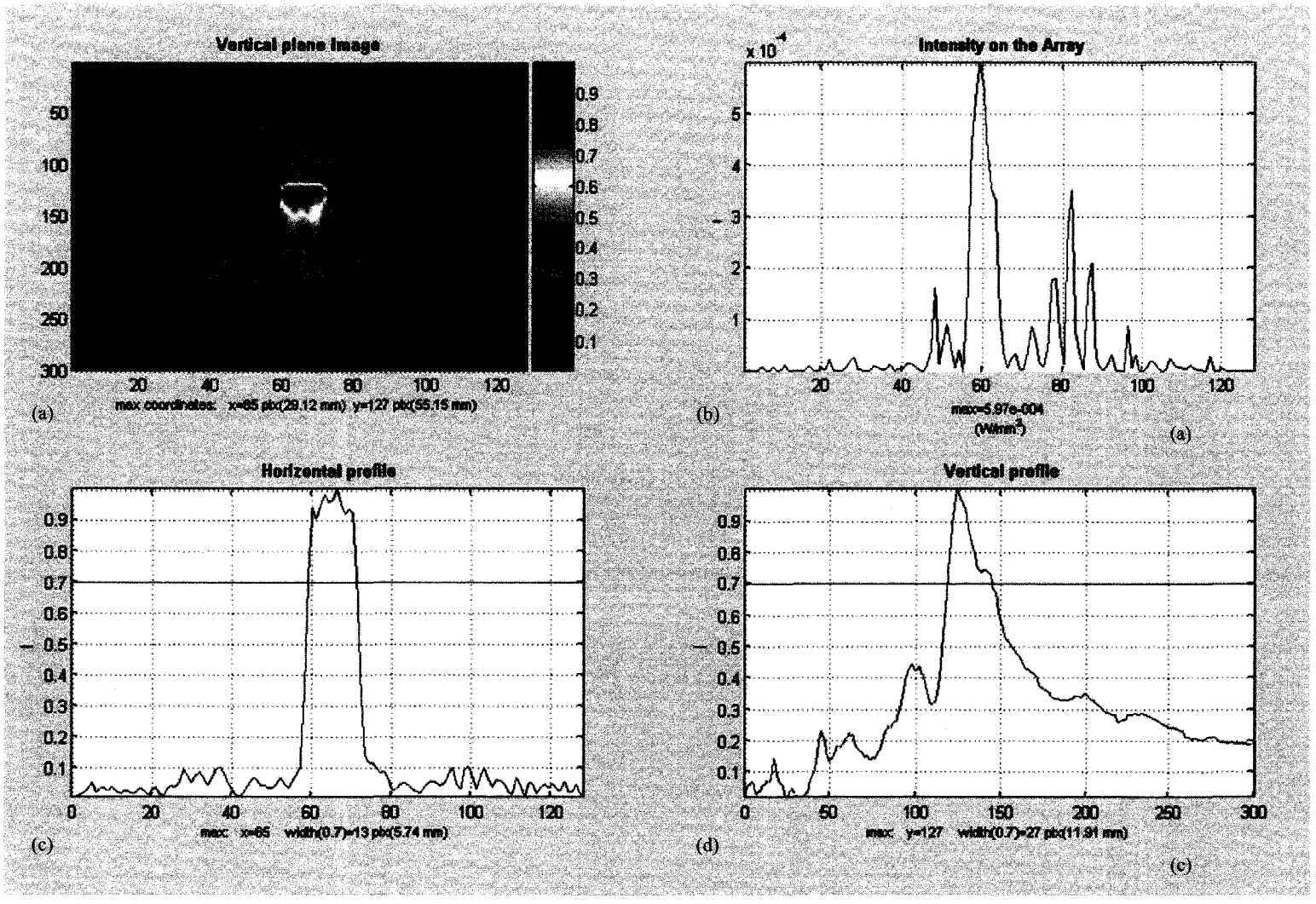

Fig.3.20 (a) Reconstructed image of the reversed field ***in presence*** of the scattering medium for the same Intensity distribution in Fig.3.9.b using the ***refraction included*** algorithm. ***Only all way transmitted*** beams in each layer was inserted in the reconstruction process. The original static object had been placed at $x_{io}=62\lambda/2\text{-}67\lambda/2$ and $y_o=128\ \lambda/2$. The reconstructed image also showed a major peak *almost* at the same place. (b) Intensity distribution in Fig.3.9.b (c) Horizontal Profile of the major peak in Vertical Plane Image. (d) Vertical Profile of the major peak in Vertical Plane Image. The inner layer of the scattering medium in this reconstruction was designed using ***Ideal inner layer with inner curved boundary*** technique.

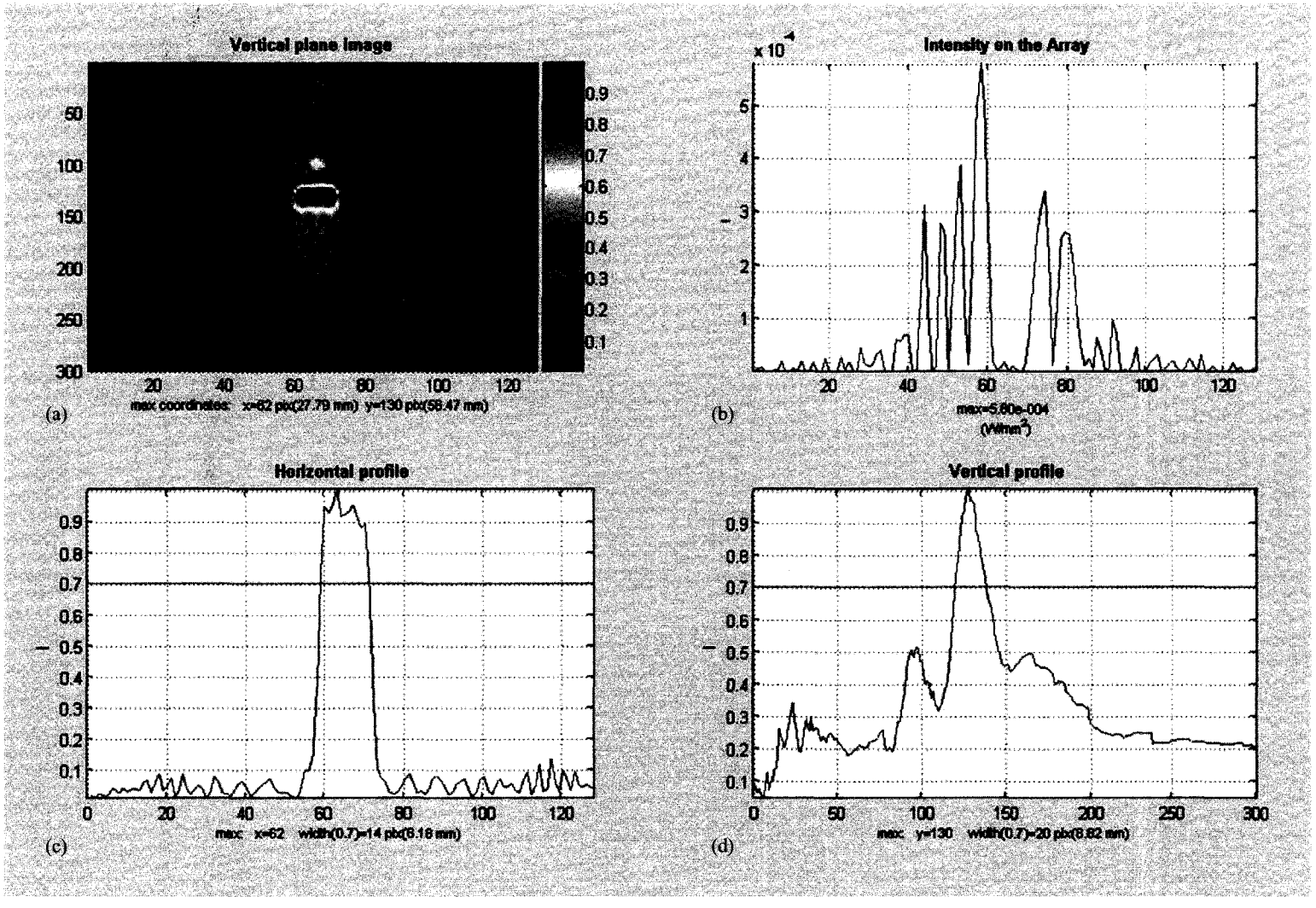

Fig.3.21 (a) ***Final*** Reconstructed image of the reversed field ***in presence*** of the scattering medium for the same Intensity distribution in Fig.3.10.a using the ***refraction included*** algorithm. The original static object had been placed at $x_{io}=62\lambda/2\text{-}67\lambda/2$ and $y_o=128\ \lambda/2$. The reconstructed image also showed a major peak at the same place. (b) Intensity distribution in Fig.3.10.a (c) Horizontal Profile of the major peak in Vertical Plane Image. (d) Vertical Profile of the major peak in Vertical Plane Image. The inner layer of the scattering medium in this reconstruction was designed using ***Random phase shifting elements*** technique.

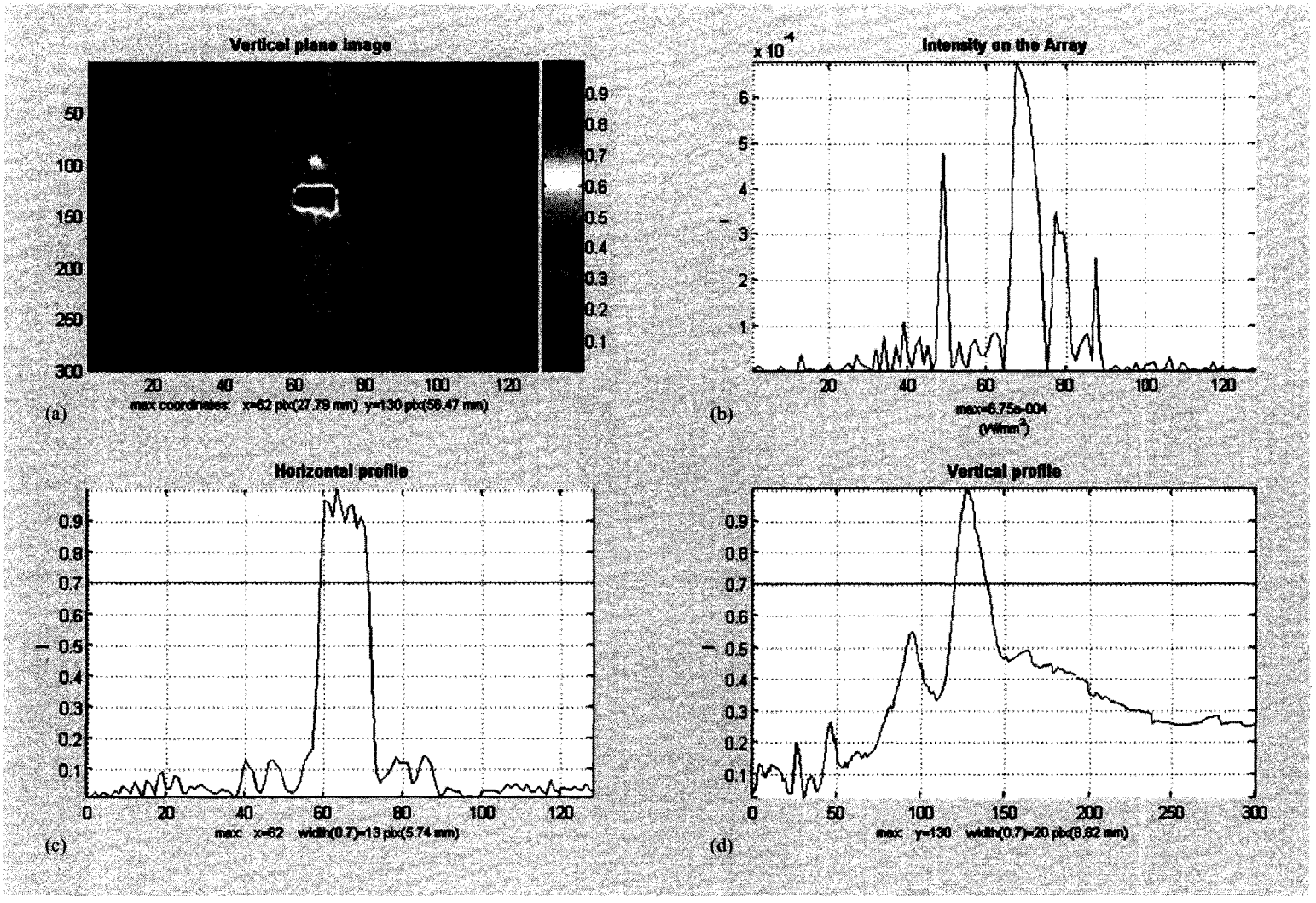

Fig.3.22 (a) ***Final*** Reconstructed image of the reversed field ***in presence*** of the scattering medium for the same Intensity distribution in Fig.3.10.b using the ***refraction included*** algorithm. The original static object had been placed at $x_{io}=62\lambda/2\text{-}67\lambda/2$ and $y_o=128\ \lambda/2$. The reconstructed image also showed a major peak at the same place. (b) Intensity distribution in Fig.3.10.b (c) Horizontal Profile of the major peak in Vertical Plane Image. (d) Vertical Profile of the major peak in Vertical Plane Image. The inner layer of the scattering medium in this reconstruction was designed using ***Ideal inner layer with inner curved boundary*** technique.

Chapter 4

EXPERIMENT

4.1. Phantom Preparation

As mentioned in the previous chapter, the effectiveness of the simulation in image reconstruction reveals itself when the estimated intensity distribution is replaced by real experimental data from an actual array of receivers. In order to set up the experimental apparatus the first step was to make an appropriate phantom as a representative for the scattering medium. As a matter of fact, since the curved inner layer has a much more distorting effect on the transmitted field than the other two flat layers (due to their plane interfaces), the validity of the simulation could be examined by either a single or a multiple layered structure as the scattering medium. For this reason a single layered phantom was designed with an irregular surface on one side. From an acoustical point of view, it was crucial to find or synthesize a material whose main acoustic parameters (sound velocity, density, and sound attenuation) were close to those of a real skull bone. To do this, mixtures of different metal powders in epoxy foundation were chosen to be used in fabrication process. This selection was made based on the fact that it was possible to manipulate the mixture's acoustical properties by changing the mass and volume ratio between the components, i.e. powder and epoxy. Fig.4.1 shows some of the test samples after they were dried and polished on their surfaces.

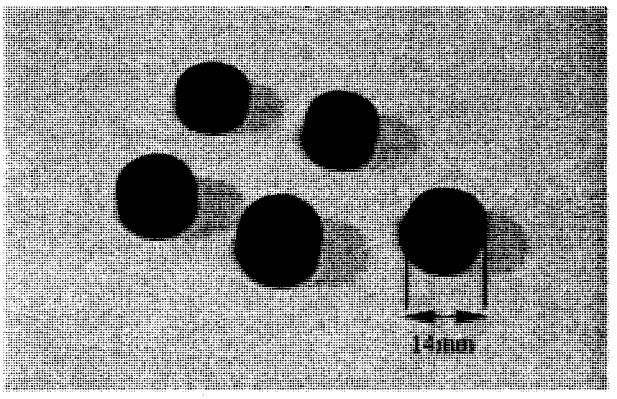

Fig.4.1. Test samples in final phantom fabrication process.

After each sample was made, a series of experiments were conducted to measure its acoustical properties. In fact, also like the other studies, it was almost impossible to find a mixture with exactly the same acoustical properties as a real skull bone. It was inevitable that at least one of the main aforementioned parameters differed from its real value; but, as the future plan of the project was to replace the home made scattering medium with *ex-vivo* skull bones, it could not be an issue. The results of the measurements on the test samples are presented in Table.4.1.

Table4.1. Acoustical properties and measurement results for test samples.

Sample (an epoxy with powder)	m_{powder}/m_{total}	d, mm	A_0/A, dB	c, km/s	ρ, g/cm^3	Z	T	α, dB/cm
Epoxy "Leco"+ $W_{12\mu m}$								
1	0.15	3.5	5.5	2.40	1.30	3.12	0.877	12.5
2	0.20	3.3	6.0	2.43	1.35	3.28	0.860	14.0
3	0.175	3.7	5.5	2.30	1.35	3.11	0.89	12.0
4	0.25	3.55	5.5	2.24	1.40	3.14	0.875	12.0
5	0.30	3.55	6.0	2.43	1.45	3.52	0.838	12.6
Epoxy "Abocast"+$Ti_{50\mu m}$	0.3	18.5	13.5	2.36	1.89	4.48	0.82	24.13
Epoxy "EpoxyCure"+$SiC_{20\mu m}$								
S1	0.33	7.95	7.0	2.90	1.47	4.26	0.77	6.0
S2	0.25		6.0		1.38			
S3	0.20	7.00	5.5	2.78	1.33	3.7	0.82	5.4
S4	0.11	6.76	5.0	2.74	1.26	3.45	0.845	5.2
Epoxy "EpoxyCure"+$BC_{20\mu m}$								
B0	0.6-0.9	1.12	8.0	3.47	1.60	5.55	0.67	40.4
B1	0.33	8.15	10		1.38			10
Epoxy+$W_{12\mu m}$	0.30	8.70	10	2.13	1.62	3.45	0.845	10.0
Hyps		7.4			1.8(wet)			
Plastic		5-6	10.6	2.27	1.25		0.905	15-19
errors	±0.01	±0.1	±0.5	3%	±0.02	3.5%		10%

The parameters in Table 4.2 were measured in the following manner:

m_{powder}/m_{total} :

mass ratio: powder mass in the specimen to the total mass of specimen; (Measured by weighing on a digital scale)

ρ (density):

measured with a balance using a submersion technique

d (thickness of each specimen):

measured with a micrometer

A_0/A (signal amplitude ratio):

A_0: without the sample, A: with the sample; measured with an oscilloscope

Parameters A_0/A and Δt were measured by placing and removing the sample between the transmitter (plane ultrasonic transducer) and the receiver (needle hydrophone) in a water tank.

the calculated parameters:

c: Sound velocity;

Z: Acoustical impedance ($Z = \rho c$);

T: Signal transmission coefficient through the two boundaries of each sample (due to the impedance mismatch);

α: Sound attenuation; Calculated by subtracting the losses due to the impedance mismatch.

Compared to the acoustical properties of a real skull bone (Table 1.1), an average sound velocity and density of the skull bone was satisfied by the test sample fabricated from *Epoxy Abocast* and $Ti_{50\mu m}$ powder. Therefore a single layer phantom in large scale was made at the time from the best matching compound (Epoxy+$Ti_{50\mu m}$ powder). Fig4.2

shows the final phantom layer fabricated in our lab. It was polished on the flat side and machined on the curved side so that the scratches were not comparable to the wavelengths (in water and sample itself). Furthermore, as the attenuation of the mentioned compound was different from the one for a real skull, its measured attenuation (2413dB/m) was replaced in the simulation instead of the one for a typical real skull bone at a frequency of 1.7MHz (~3400dB/m).

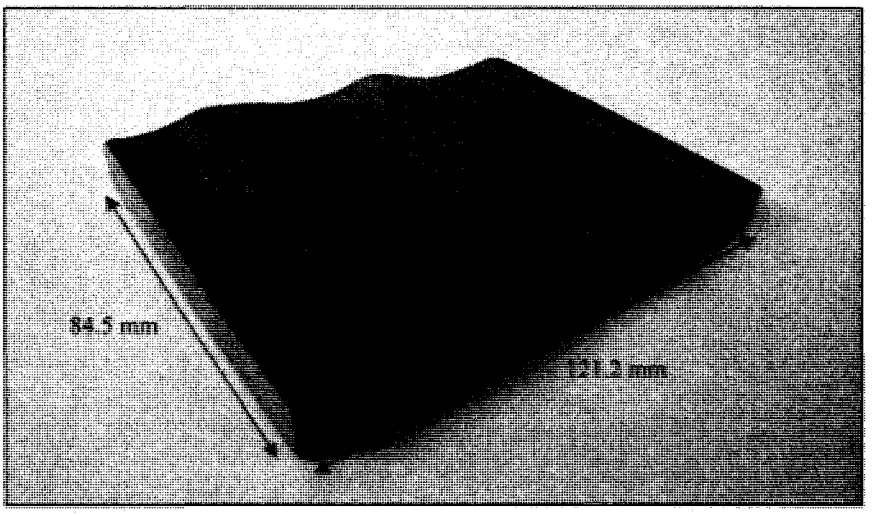

Fig.4.2. Final phantom layer fabricated from **Epoxy** and $\mathbf{Ti_{50\mu m}}$ powder.

4.2. Instrumentation

In order to setup the experimental apparatus, a linear array of receivers with 128 flat point receivers (each 3.2mm in diameter) sited in 0.44mm steps was used. A 4-Axis X-Sel scanner was programmed and used to position the array of receivers. The scanner had a positioning accuracy of 1μm. Moreover, a water tank from acrylic glass and two holders were fabricated in order to site the point source transducer and the phantom layer at any desired distance in the water tank. Tap water which was allowed to stand for at least 4 days was used during the measurements and data acquisition process. Unless will be mentioned, the acoustical properties of the parts were the same as declared in Table 3.1. The transducer used in the apparatus was a small flat transducer driven at a frequency of

1.7MHz and a diameter of 5.5 millimeters. It behaved like an extended source in the near field and a point source in the far field (>6cm from the source). The Final layout of the experimental apparatus used to obtain intensity distribution on a real array of 128 receivers is illustrated schematically in Fig.4.3. A program was generated in LABVIEW environment to control the X-Sel scanner. The program sent the initial signal to trigger the transducer through an ADC (Analog to Digital Converter). The signal was then inverted by an inverter and sent to the U-Tex UT Pulsar. The acoustical pulse was then generated by the pulsar and was sent to the transducer. The field was then received by the array of receivers (the multiplexer switched between the receivers 32 times through 4 channels to cover the whole array). At the end the receiving signals were amplified and sent to the computer to be analyzed.

Pictures of the linear array of 128 receivers and final experimental setup are also shown in Fig.4.4 and Fig.4.5 respectively.

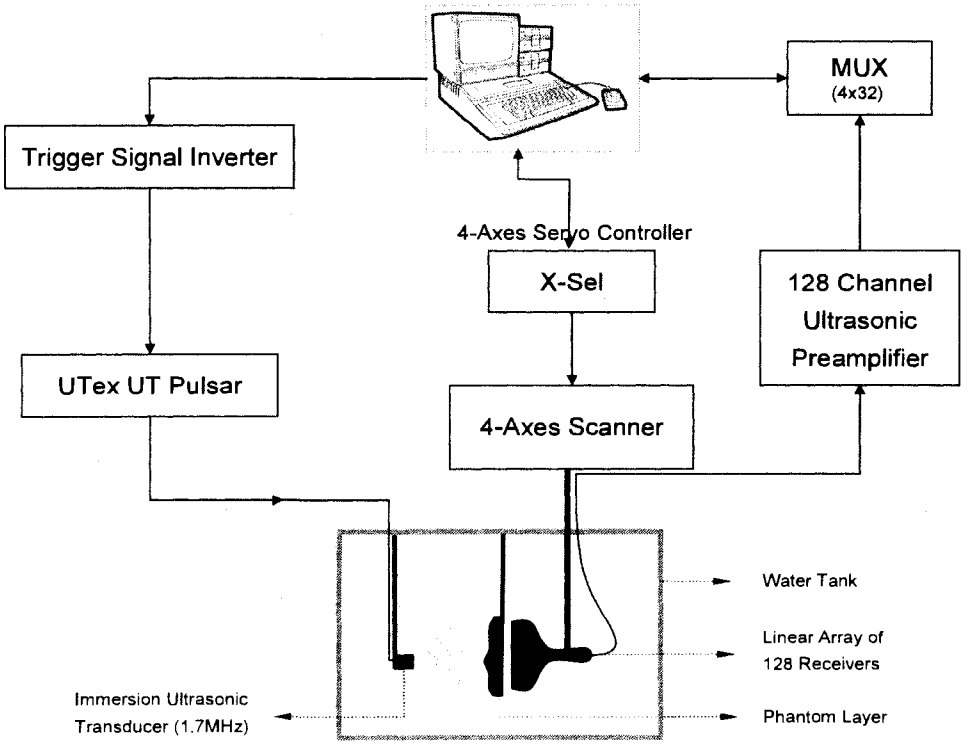

Fig.4.3. experimental configuration used to obtain acoustical field distribution on the linear array of 128 receivers.

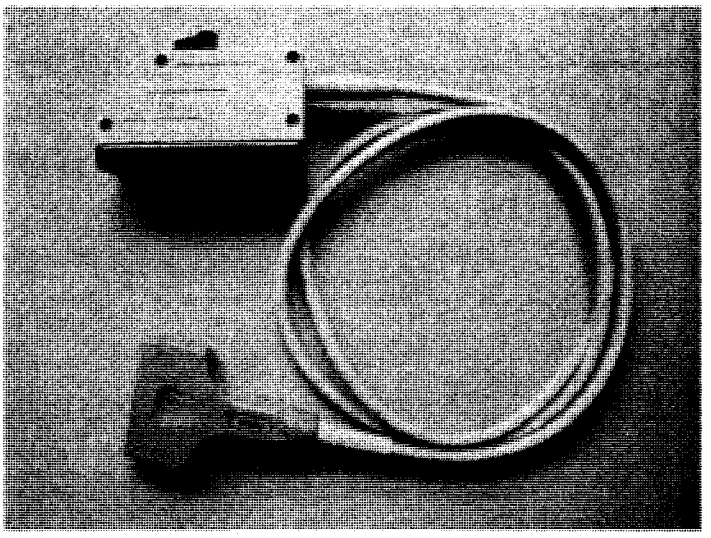

Fig.4.4. Linear array of 128 flat point receivers (each 3.2mm in diameter) sited in 0.44mm steps.

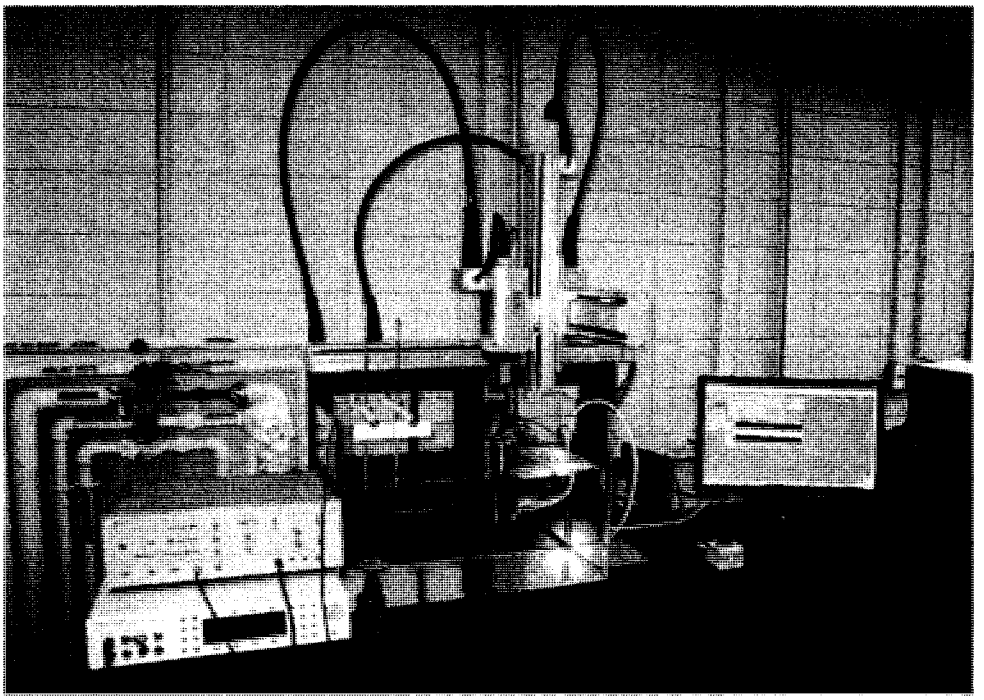

Fig.4.5. A picture of the experimental setup used in data acquisition for the simulation.

To find the acoustical field distribution on the array of receivers, during all data collections, the source was placed at the middle but different distances from the array of receivers in both the absence and presence of the phantom layer. At each distance the data was collected at least five times to make sure the distribution was comparatively stable. The distances between the three main parts of the experimental setup (transducer, phantom and receiving array) are tabulated in Table 4.2. All the distances were measured using the *pulse-echo* measuring technique [40]. During the measurement of the distances, pulses with an initial amplitude of 100V, a pulse rate of 4 kHz, a pulse width of 30ns, and a frequency of 10MHz were applied to the transducer.

Table4.2. distances between the experimental setup parts.

	Phantom Layer		Focal point of the source	
	In the absence of the phantom layer	In the presence of the phantom layer	In the absence of the phantom layer	In the presence of the phantom layer
Normal distance from the array of receivers	8.21mm	8.34mm	30.3 mm, 60.2 mm and 90.4 mm	30.1 mm, 60.4 mm and 60.4 mm

4.3. Results (data acquisition and image reconstruction)

4.3.1. In the absence of the phantom layer

In the absence of the phantom layer, the field distribution on the array of receivers was almost symmetric as expected. After reaching the array of receivers, the field's amplitude was detected by each receiver and the results were saved as a 1 by 128 element matrix to be used in the reconstruction part of the simulation. Fig.4.6 shows the results at the three mentioned distances (Table 4.2).

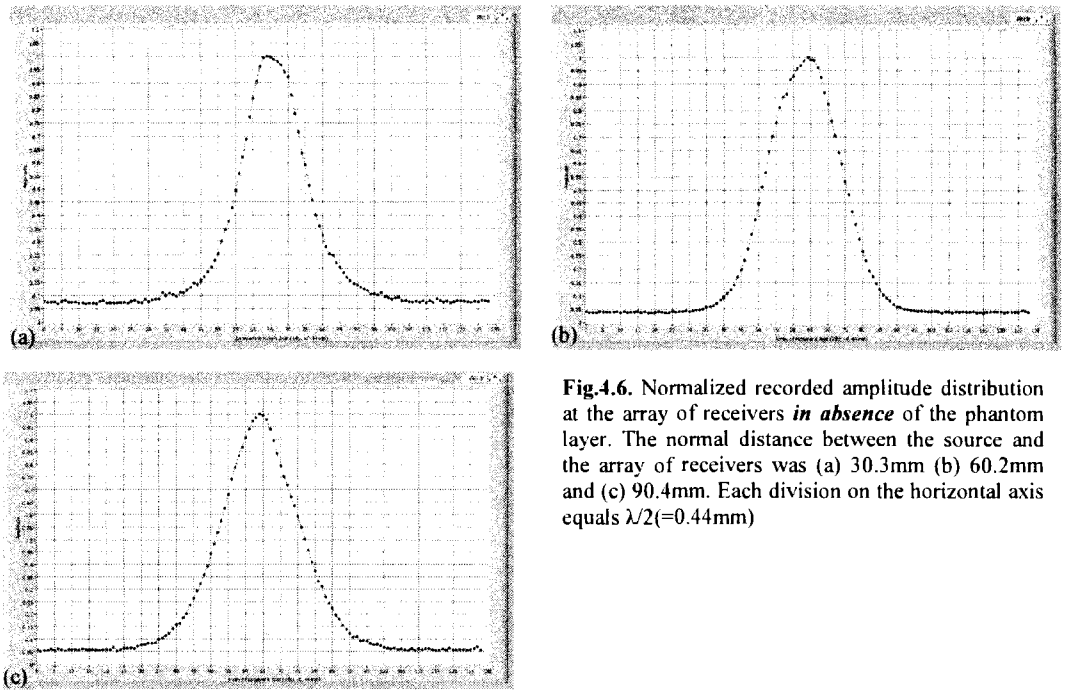

Fig.4.6. Normalized recorded amplitude distribution at the array of receivers ***in absence*** of the phantom layer. The normal distance between the source and the array of receivers was (a) 30.3mm (b) 60.2mm and (c) 90.4mm. Each division on the horizontal axis equals $\lambda/2$(=0.44mm)

After inserting the matrices in the code, the simulation was then executed to do the reconstruction. The results are shown in figures 4.7, 4.8 and 4.9. Table 4.3 compares the original and reconstructed positions of the point source. As expected, the reconstructed coordinates are very close to the original ones. A maximum deviation of 2 pixles (0.88mm) was observed between the original and reconstructed coordinates which was an acceptable error for our purpose. At this point, the experimental results supported the theory and simulation.

Table4.3. Original and reconstructed coordinates of the point source ***in absence*** of the phantom layer. 1pix=$\lambda/2$=0.44mm.

Distance from the array of receivers	Original Position	Reconstructed Position
30.3 mm	x = 64 pix y = 68 pix	x = 64 pix y = 69 pix
60.2 mm	x = 64 pix y = 136 pix	x = 64 pix y = 134 pix
90.4 mm	x = 64 pix y = 204 pix	x = 64 pix y = 203 pix

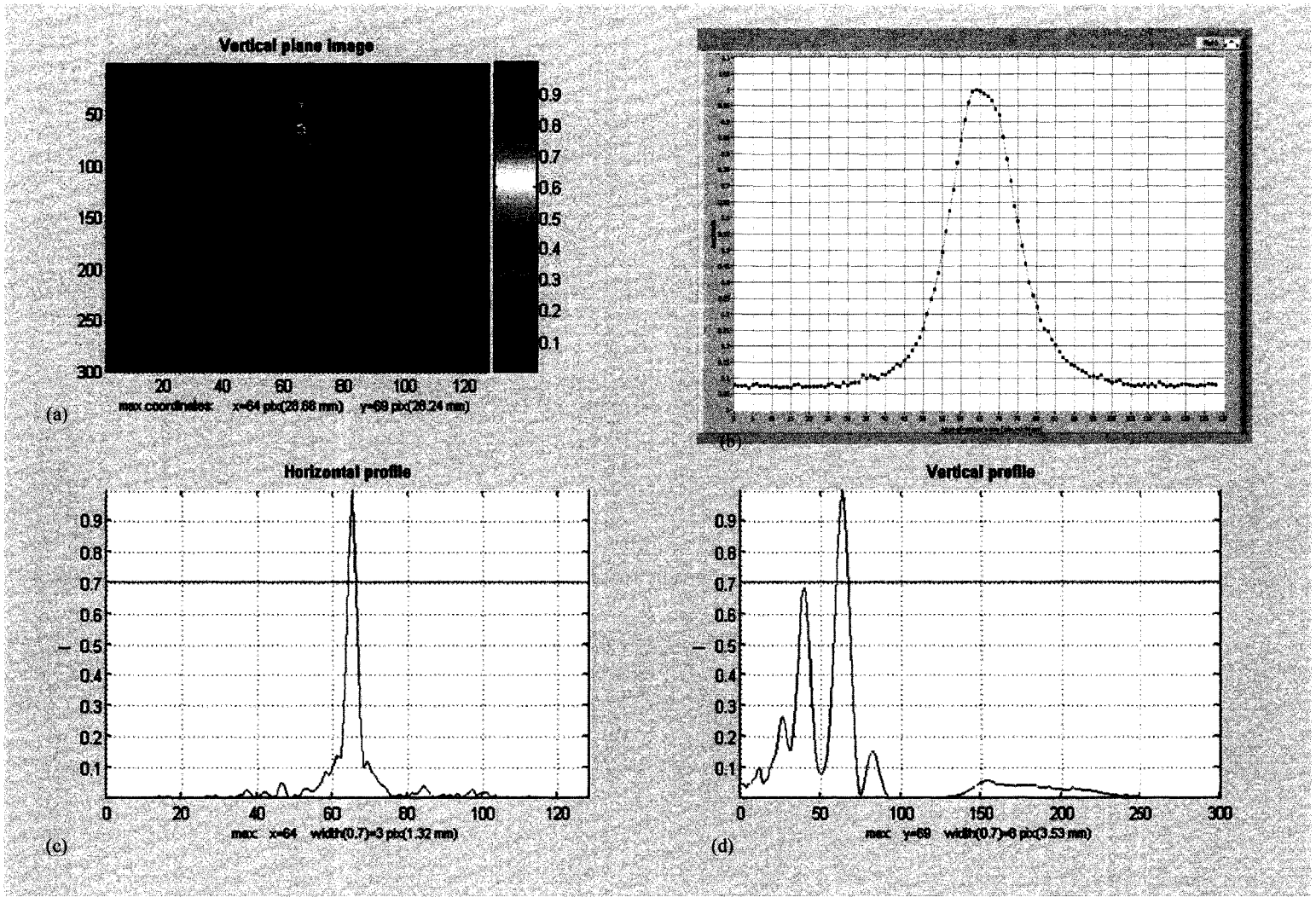

Fig.4.7. Image reconstruction ***in absence*** of the phantom layer. The original point source had been placed at $x_{io}=64\lambda/2(64pixels)$ *and* $y_o=68\ \lambda/2(68pixels)$. (a) Normalized vertical plane image of the reconstructed field. (b) Intensity distribution taken from Fig.4.6.a. (c) Horizontal Profile of the major peak in vertical plane image. (d) Vertical Profile of the major peak in vertical plane image.

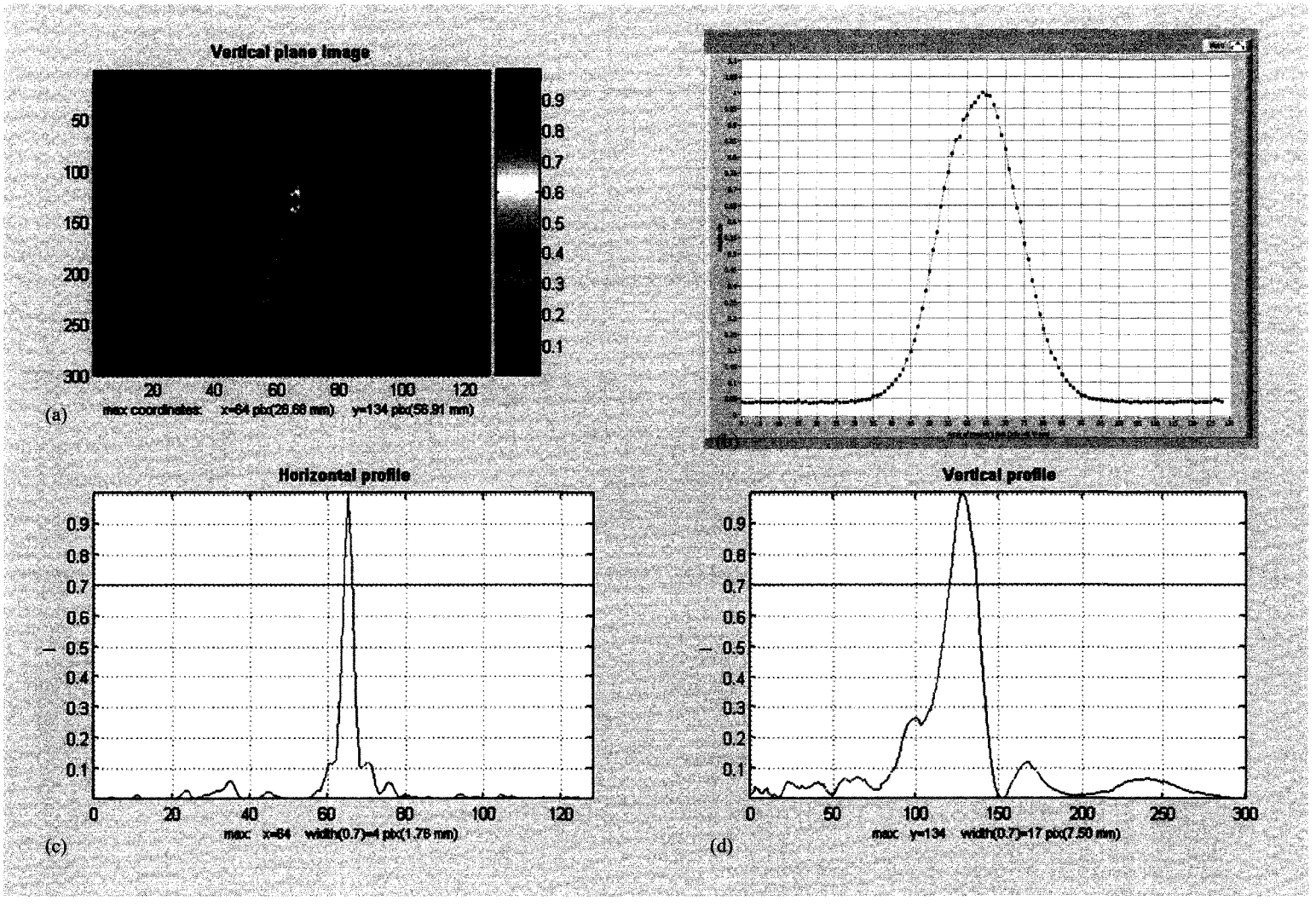

Fig.4.8. Image reconstruction ***in absence*** of the phantom layer. The original point source had been placed at $x_{io}=64\lambda/2(64pixels)$ *and* $y_o=136\,\lambda/2(136pixels)$. (a) Normalized vertical plane image of the reconstructed field. (b) Intensity distribution taken from Fig.4.6.b. (c) Horizontal Profile of the major peak in vertical plane image. (d) Vertical Profile of the major peak in vertical plane image.

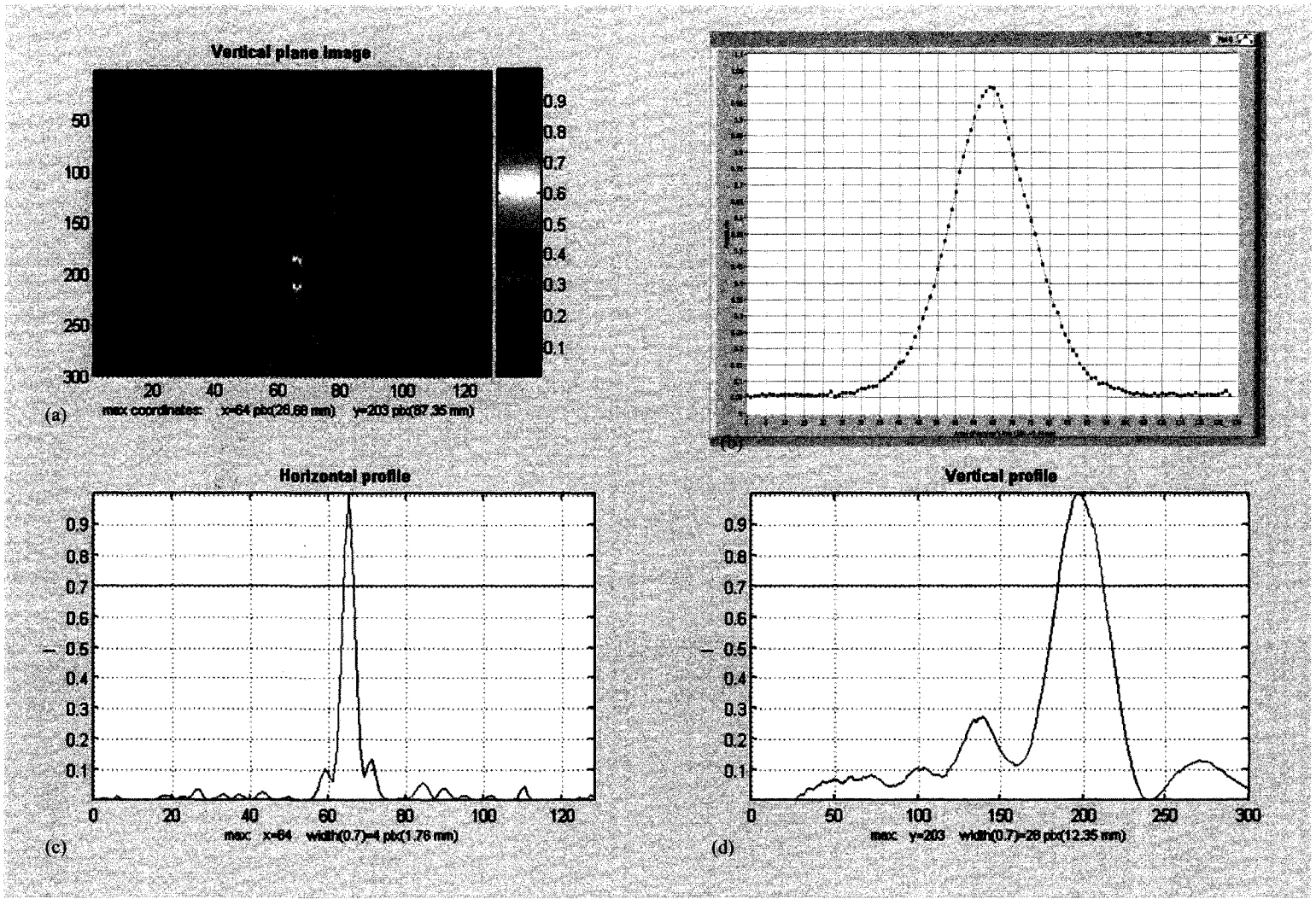

Fig.4.9. Image reconstruction ***in absence*** of the phantom layer. The original point source had been placed at $x_{io}=64\lambda/2(64pixels)$ *and* $y_o=204\ \lambda/2(204pixels)$. (a) Normalized vertical plane image of the reconstructed field. (b) Intensity distribution taken from Fig.4.6.c. (c) Horizontal Profile of the major peak in vertical plane image. (d) Vertical Profile of the major peak in vertical plane image.

4.3.2. In the presence of the phantom layer

After collecting data in the absence of the scattering medium, the phantom layer was then applied to the setup (at a distance of 8mm from the array of receivers). Again according to Table.4.2 the small transducer was put at the mentioned distances and both the amplitude and phase distribution obtained and saved as 1 by 128 element matrices to be used in the program. Amplitude distributions at the three distances are shown in Fig.4.10.

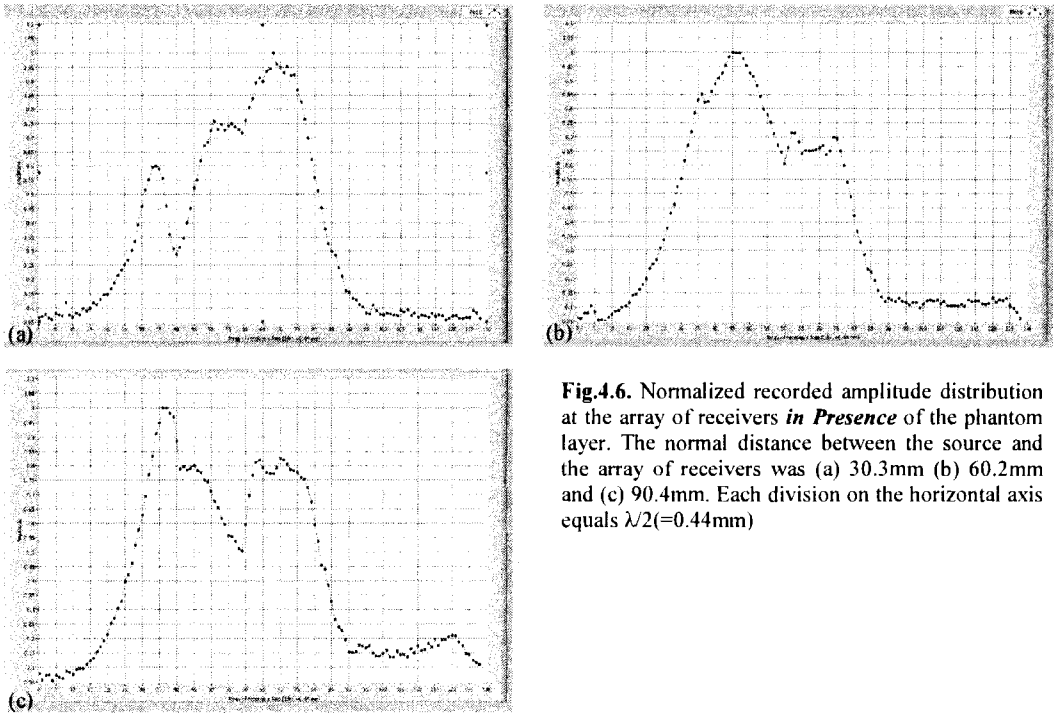

Fig.4.6. Normalized recorded amplitude distribution at the array of receivers ***in Presence*** of the phantom layer. The normal distance between the source and the array of receivers was (a) 30.3mm (b) 60.2mm and (c) 90.4mm. Each division on the horizontal axis equals $\lambda/2$(=0.44mm)

The next step was to replace all physical and acoustical properties of the simulated scattering medium with the ones of the real phantom layer. From the physical point of view, three layers of the simulated scattering medium should be changed to one layer; moreover, the randomly curved boundary of the inner layer in the simulation also needed to be substituted by the exact curve of the boundary of the fabricated phantom layer (Fig.4.2). To get the curvature of the phantom layer first a B-Scan was taken from the phantom when the transducer faced to its flat surface. The experimental configuration of

the scan and the B-Scan itself are shown in Fig.4.11.a and Fig.4.11.b respectively. As can be seen in Fig.4.11.b, the back surface and the curved one showed maximum reflections and therefore in the B-Scan image they had higher amplitudes (white lines).

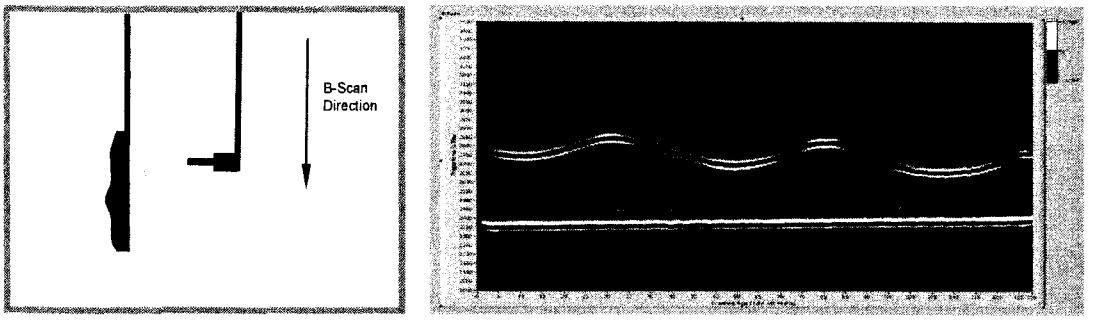

Fig.4.11. (a) schematic configuration of the B-Scan setup. (b) The B-Scan taken from the phantom layer in the shown direction. The white lines show the front and back surfaces of the phantom. Each division along the horizontal axis equals 0.44mm ($\lambda/2$).

To replace the curvature in the simulation, the time difference between the two lines (flat and curved surfaces) was obtained from 128 intervals (each $\lambda/2$=0.44 in size) and saved as the y coordinates of distribution of the points in a 1 by 128 element matrix. The matrix was then processed in MATLAB to fit the best curve into the points. The fitted curve was used as the inner boundary of the simulated phantom layer in the simulation.

After all aforementioned steps, the simulation code was ready to process the inserted data and reconstruct the image plane related to each intensity distribution. The distances in which the data collected were tried to be the same as last part (see Table 4.2). It was obvious that between the two inner layer design techniques, explained in chapter 3, only the *Ideal inner layer with inner curved boundary* technique was applicable in the experiment part. On the other hand, for image plane reconstruction, both *refraction free* and *refraction included* algorithms were used to see how they are comparable to each other. It was expected that the *refraction included* algorithm which was the last and most comprehensive algorithm developed would give the most accurate reconstruction results, i.e. the reconstructed coordinates be closer to the original ones, compared to *refraction free* algorithm. The results of the *refraction free* algorithm are shown in Fig.4.12,

Fig.4.13 and Fig.4.14. The results for the *refraction included* algorithm are also shown in Fig.4.15, Fig.4.16 and Fig4.17.

As can be distinguished by comparing the two set of above mentioned figures, the *refraction free* algorithm showed not to provide satisfactory results. This can be observed from the *vertical image planes* in Fig.4.12, Fig.4.13 and Fig.4.14 which either do not contain a significant maximum or the peaks are not happening at the acceptable coordinates. This showed us that the *refraction free* algorithm was not a reliable algorithm in our image reconstruction. Furthermore, the disability of the algorithm could also be explained due to the fact that the phantom layer was too thick that refraction had a considerable effect on the passing through beams and it was not allowed to be neglected.

On the other hand, due to Fig.4.15, Fig.4.16 and Fig4.17 the *refraction included* algorithm successfully reconstructed the source's positions. A comparison has been made between the original and reconstructed coordinates of the point source in Table 4.4.

Table4.4. Original and reconstructed coordinates of the source ***in presence*** of the phantom layer based on the comprehensive ***refraction included*** algorithm. 1pix=$\lambda/2$=0.44mm.

Distance from the array of receivers	Original Position	Reconstructed Position
30.1 mm	x = 64 pix y = 68 pix	x = 64 pix y = 69 pix
60.4 mm	x = 64 pix y = 136 pix	x = 64 pix y = 138 pix
90.3 mm	x = 64 pix y = 204 pix	x = 64 pix y = 205 pix

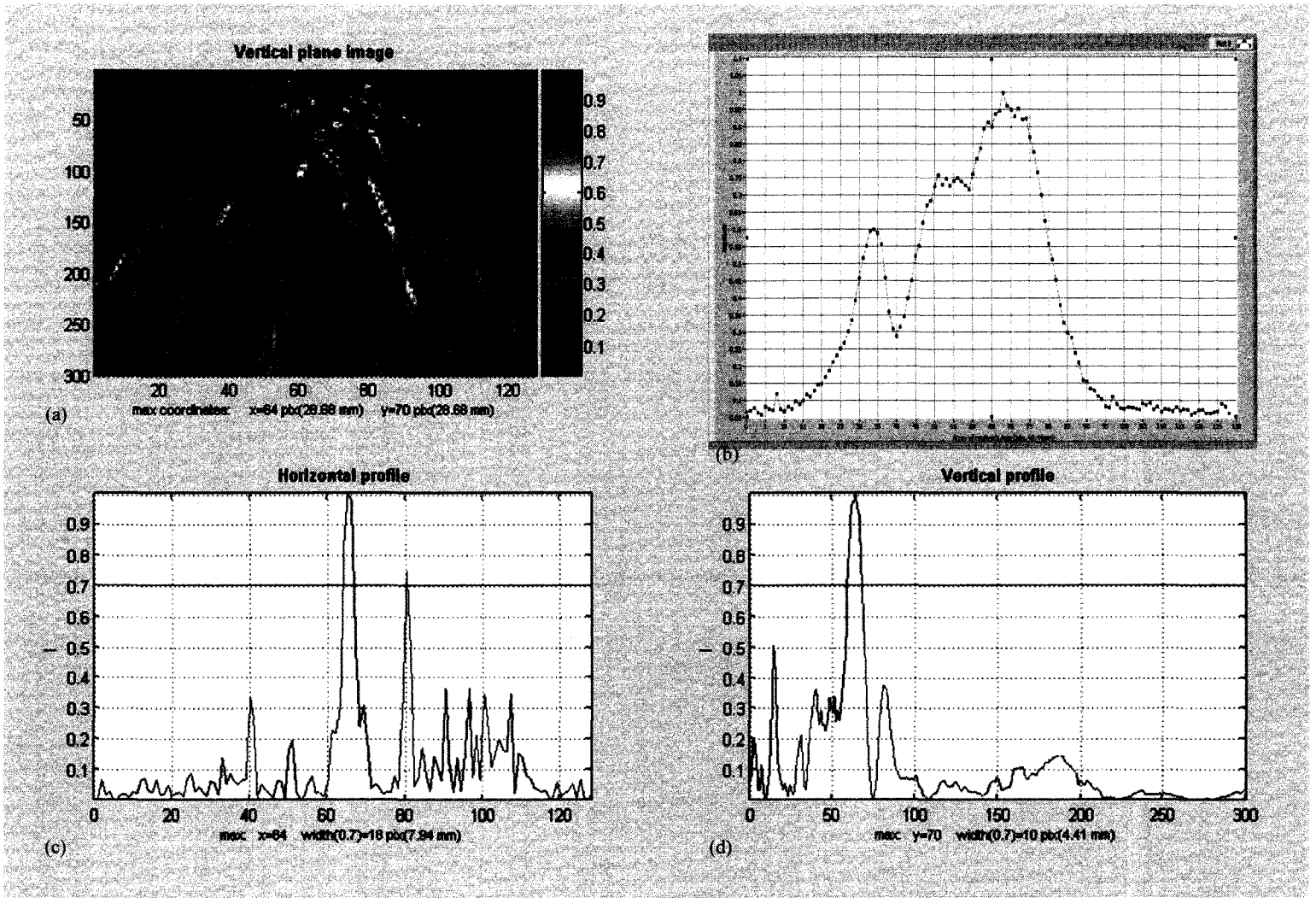

Fig.4.12. Image reconstruction ***in presence*** of the phantom layer based on the ***refraction free*** algorithm. The original point source had been placed at $x_{io}=64\lambda/2(64pixels)$ *and* $y_o=128\ \lambda/2(128pixels)$. (a) Normalized vertical plane image of the reconstructed field. (b) Intensity distribution in Fig.3.10.b. (c) Horizontal Profile of the major peak in vertical plane image. (d) Vertical Profile of the major peak in vertical plane image.

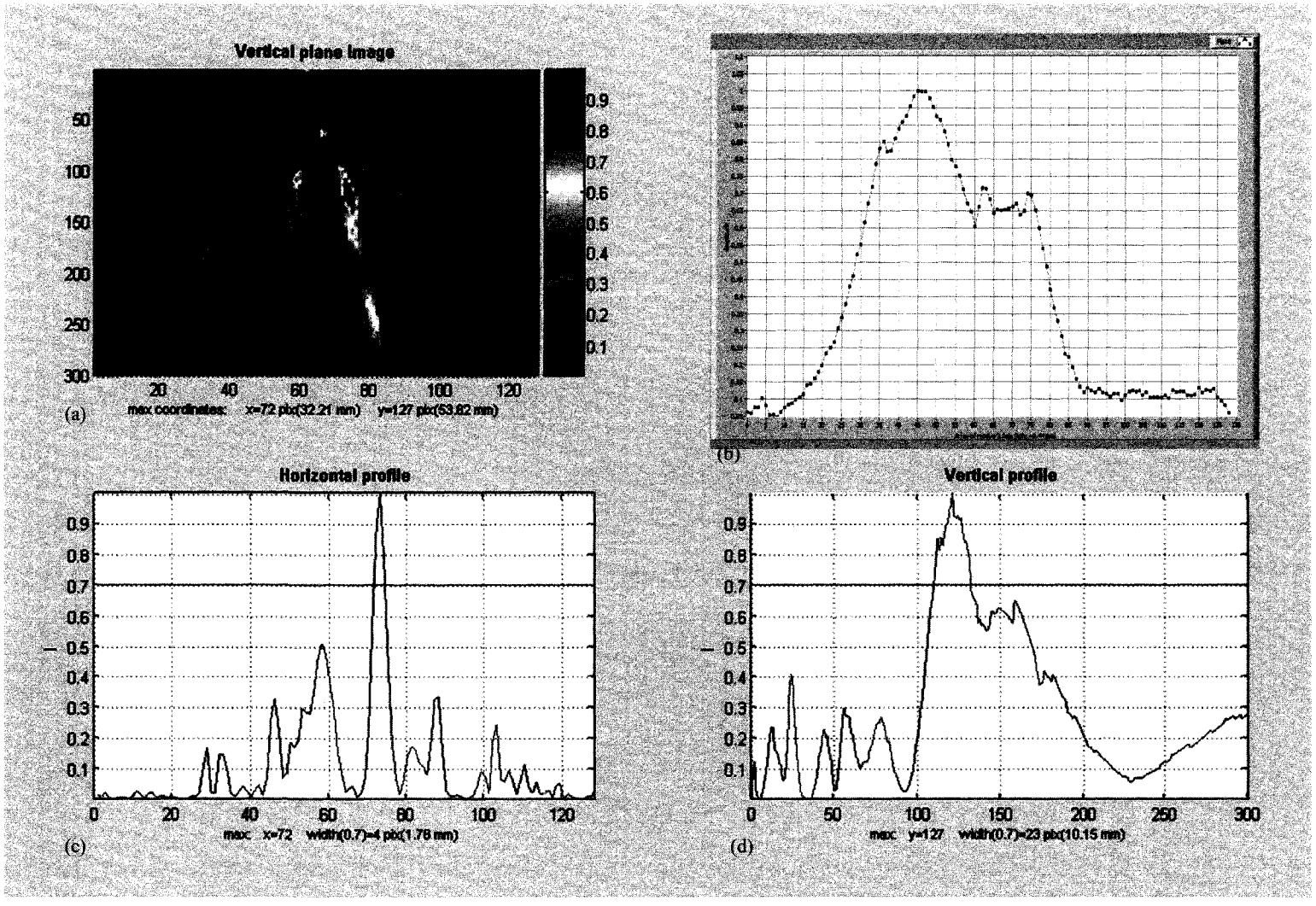

Fig.4.13. Image reconstruction ***in presence*** of the phantom layer based on the ***refraction free*** algorithm. The original point source had been placed at x_{io}=*64λ/2(64pixels) and* y_o=*128 λ/2(128pixels)*. (a) Normalized vertical plane image of the reconstructed field. (b) Intensity distribution in Fig.3.10.b. (c) Horizontal Profile of the major peak in vertical plane image. (d) Vertical Profile of the major peak in vertical plane image.

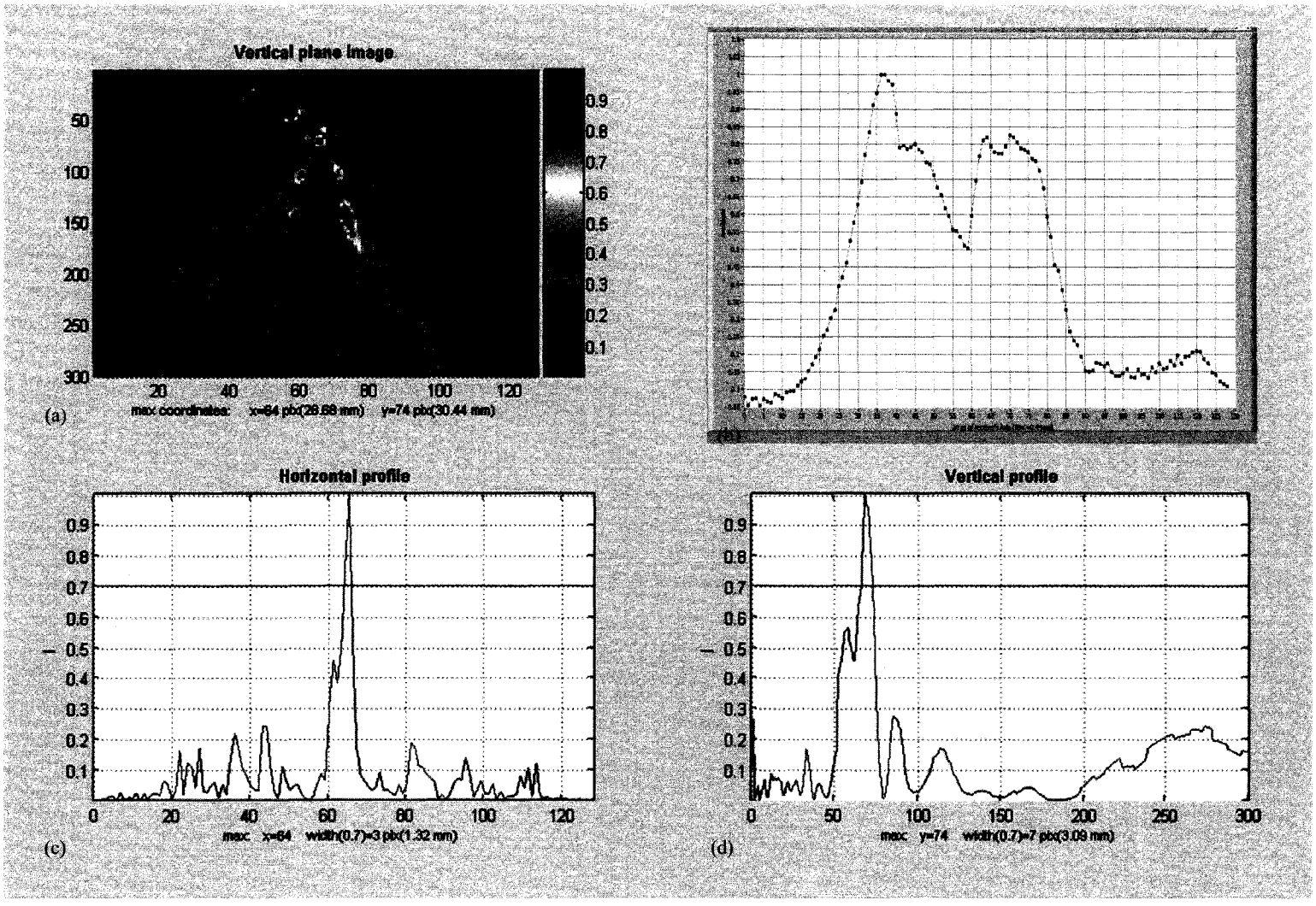

Fig.4.14. Image reconstruction ***in presence*** of the phantom layer based on the ***refraction free*** algorithm. The original point source had been placed at $x_{io}=64\lambda/2(64pixels)$ *and* $y_o=128\ \lambda/2(128pixels)$. (a) Normalized vertical plane image of the reconstructed field. (b) Intensity distribution in Fig.3.10.b. (c) Horizontal Profile of the major peak in vertical plane image. (d) Vertical Profile of the major peak in vertical plane image.

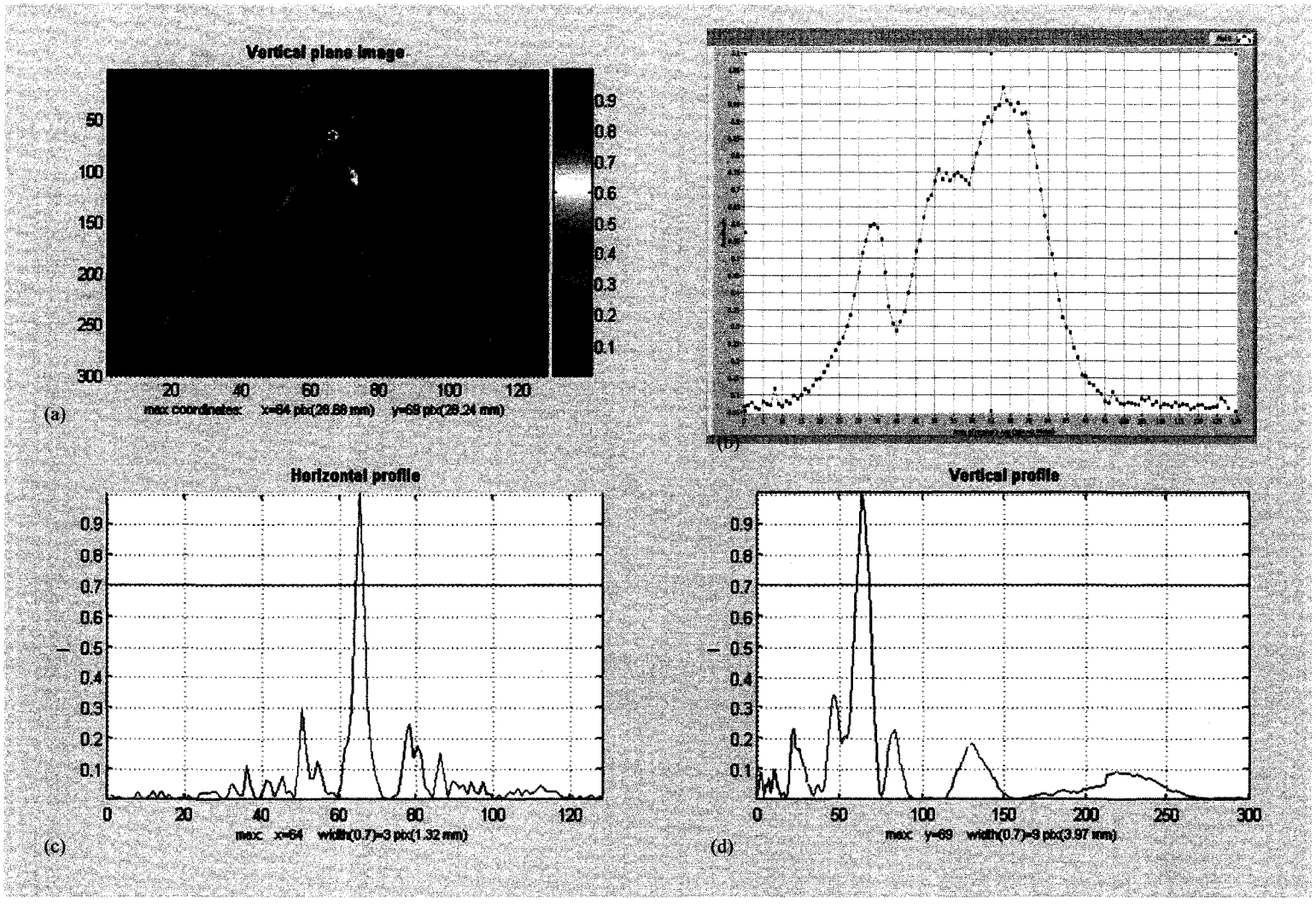

Fig.4.15. Image reconstruction ***in presence*** of the phantom layer based on the ***refraction included*** algorithm. The original point source had been placed at $x_{io}=64\lambda/2(64pixels)$ *and* $y_o=128\ \lambda/2(128pixels)$. (a) Normalized vertical plane image of the reconstructed field. (b) Intensity distribution in Fig.3.10.b. (c) Horizontal Profile of the major peak in vertical plane image. (d) Vertical Profile of the major peak in vertical plane image.

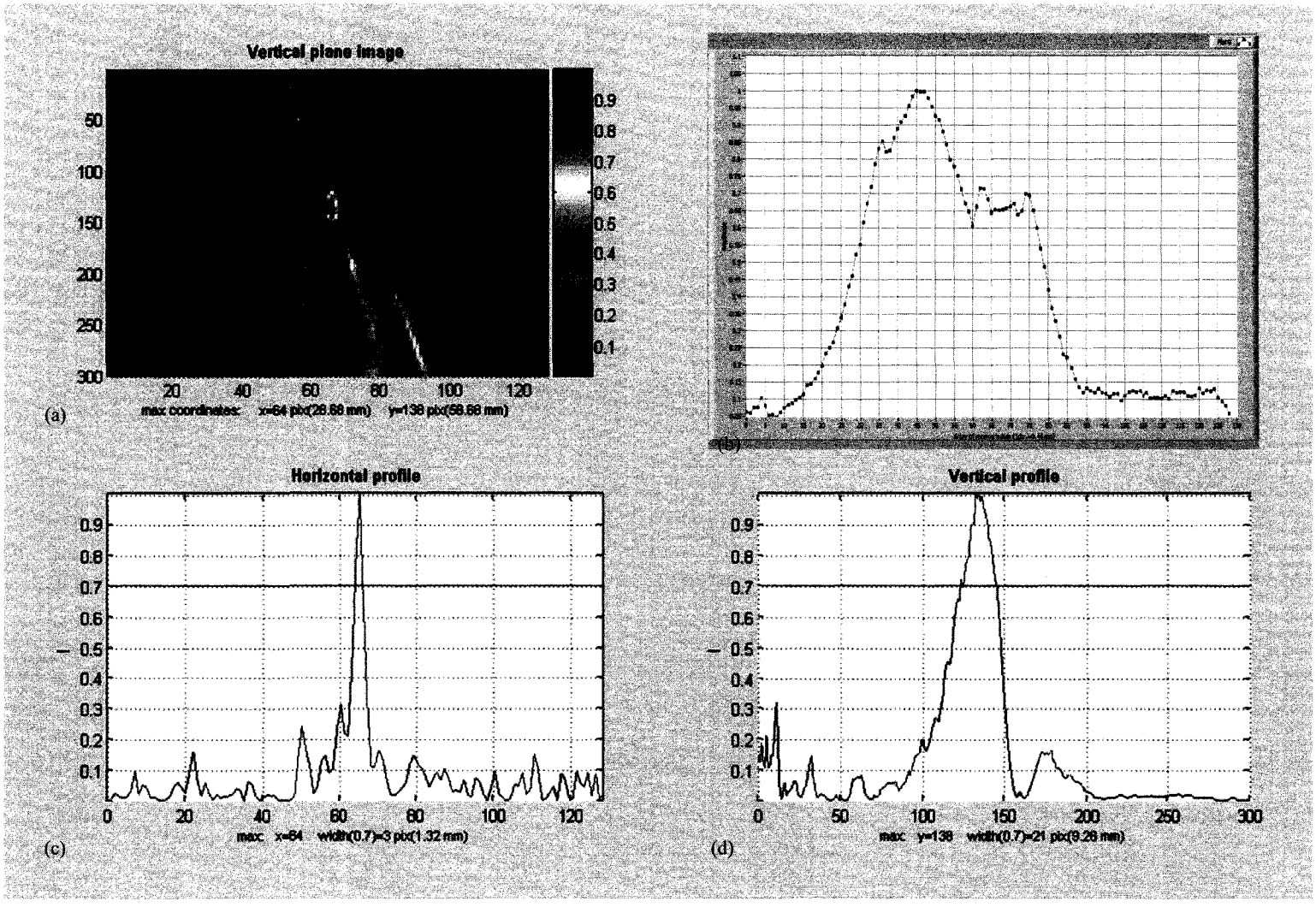

Fig.4.16. Image reconstruction ***in presence*** of the phantom layer based on the ***refraction included*** algorithm. The original point source had been placed at *xio=64λ/2(64pixels) and* y_o*=128 λ/2(128pixels).* (a) Normalized vertical plane image of the reconstructed field. (b) Intensity distribution in Fig.3.10.b. (c) Horizontal Profile of the major peak in vertical plane image. (d) Vertical Profile of the major peak in vertical plane image.

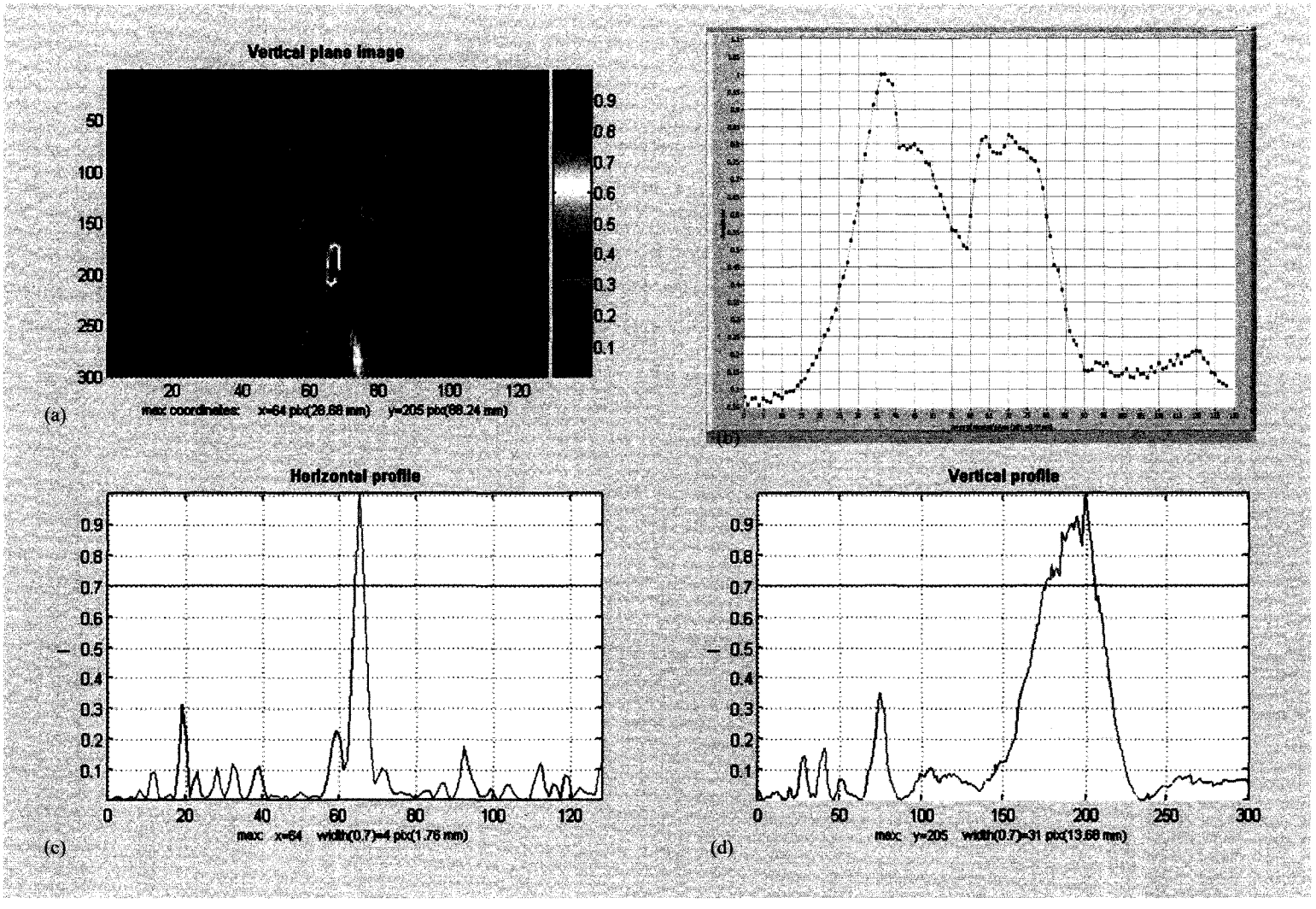

Fig.4.17. Image reconstruction ***in presence*** of the phantom layer based on the ***refraction included*** algorithm. The original point source had been placed at $x_{io}=64\lambda/2(64pixels)$ *and* $y_o=128\ \lambda/2(128pixels)$. (a) Normalized vertical plane image of the reconstructed field. (b) Intensity distribution in Fig.3.10.b. (c) Horizontal Profile of the major peak in vertical plane image. (d) Vertical Profile of the major peak in vertical plane image.

4.4. Conclusion

To conclude the results of the experiment part it should be mentioned that although both the *refraction free* and *refraction included* algorithms gave satisfactory results in the simulation part (chapter 3), and they both predicted the static object's position with an acceptable accuracy, the *refraction free* algorithm showed to be non-practical as it was not able to reconstruct the real position of the static object. As explained in the previous section, this could be explained by the fact that refraction plays an important role during data acquisition and it can not be neglected in real circumstances, specifically when the scattering object is really thick.

Chapter 5

CONCLUSION AND FUTURE WORK

A new noninvasive image reconstruction algorithm through a simplified human skull phantom has been developed. The final program was able to predict the initial position of a source of ultrasound placed behind the homemade phantom layer.

A thorough review of the other research groups studies were made before the basics of the algorithm being created. According to the reviewed materials, the majority of articles concerning matched-filtering process were devoted to the therapeutic effect of ultrasound or ultrasound surgery. There are considerably less articles discussing ultrasonic brain structure imaging through the intact skull. This was most likely due to the fact that ultrasound therapy required rather low frequencies (not higher than 1 MHz), which effectively could reduce spatial resolution.

During this study it has been tried to develop a method based on the Matched Filtering Method, to predict the effect of a simplified skull bone-like scattering medium, through both simulation and experiment, and then try to compensate for that distortion to finally reconstruct the initial acoustical field.

In chapter 3, a theoretical and mathematical basis has been developed to execute all possible distortion calculations and to first predict the intensity distribution of a scattering object, placed at different distances from the array of receivers in either the absence or the presence of the scattering medium. Secondly the calculated intensity distributions were used to find information about the original position of the object. Meanwhile, different algorithms and techniques were suggested and their results were compared at the end of the chapter. At that point the image planes reconstructed showed a high accuracy (<0.44mm) in absence of the scattering medium. Both the refraction free and

refraction included algorithms were also showed to give acceptable results although the comprehensive refraction included results were still the most accurate.

During chapter 4, the calculated phase and intensity distributions were replaced by real measured phase and amplitude distributions on a real array of receivers. In the case that the phantom layer had not been applied to the apparatus, the intensity distribution showed to be fairly symmetric as expected, an also the reconstruction results were of high accuracy. But in the case that the phantom layer had been applied, of course, the real receiving signals had been refracted by the phantom layer from their original direction. Therefore, it was predictable that *refraction free* algorithm would not work as proper as the *refraction included* one. After running the program, the *refraction free* algorithm did not give satisfactory results as the maxima were not happened in the close vicinity of the original coordinates. On the other hand, the comprehensive *refraction included* algorithm showed to be a practical algorithm with high enough accuracy for our purpose.

As the future work, as continuity of 'Brain Project', our research group is planning to make more realistic circumstances in both the simulation and experiment. From the experimental point of view, a hemisphere-like non-homogenous phantom has planned to be made. The program then needs to be developed to simulate the mentioned phantom and replace it with the current flat one. Also instead of a transducer as a reflector, a real scattering object is planned to be used.

References

1. G.T.Clement, K. Hynynen. Micro-receiver guided transcranial beam steering. IEEE Trans. Ultrason. Ferroelectr. Freq. Control. V.49, N4, pp. 447-453, 2002.

2. G.T.Clement, K. Hynynen. A non-invasive method for focusing through the human skull. Phys.Med.Biol. V.47, pp.1219-1236, 2002.

3. K. Hynynen, G.T.Clement, N.McDannold, N. Vykhodseva, R.King, P.J.White, S.Vitek, F.A.Jolesz. 500-element ultrasound phased array system for noninvasive focal surgery of the brain: a preminary rabbit study with ex vivo human skulls. Magnetic resonance in medicine. V.52, pp.100-107, 2004.

4. M.Fink. Time reversal of ultrasonic fields – Part I: Basic principles. IEEE Trans. Ultrason. Ferroelectr. Freq. Control. V.39, N5, pp.555-566, 1992

5. F. Wu, J.-L. Thomas, M.Fink. Time reversal of ultrasonic fields – Part II: Experimental results. IEEE Trans. Ultrason. Ferroelectr. Freq. Control. V.39, N5, pp. 567-578, 1992.

6. D.Cassereau, M.Fink. Time reversal of ultrasonic fields – Part III: Theory of the closed time-reversal cavity. IEEE Trans. Ultrason. Ferroelectr. Freq. Control. V.39, N5, pp.579-592, 1992,

7. J.-L. Thomas, M.Fink. Ultrasonic beam focusing through tissue inhomogeneities with a time reversal mirror: application to transskull therapy. IEEE Trans. Ultrason. Ferroelectr. Freq. Control. V.43, N6, pp. 1122-1129, 1996.

8. M.Tanter, J.-L.Thomas, M.Fink. Focusing and steering through absorbing and aberrating layers: application to ultrasonic propagation through the skull. J.Acoust.Soc.Am.V.103, pp.2403-2410, 1998.

9. M.Tanter, J.-L.Thomas, M.Fink. Time reversal and inverse filter. J.Acoust.Soc.Am.V.108, pp.223-234, 2000.

10. S.V.Baykov, A.M.Molotilov, V.D.Svet. Physical and technological aspects of ultrasonic imaging of brain structures through thick skull bones: 1.Theoretical and model studies. Acoust. Physics. V.49 (3), pp.276-284, 2003.

11. S.V.Baykov, L.V.Babin, A.M.Molotilov, S.I.Neiman, V.V.Riman, V.D.Svet, A.I.Selyanin. Physical and technical aspects of ultrasonic imaging through thick skull bones: 2.Experimental studies. Acoust. Physics. V.49 (4), pp.389-395, 2003.

12. J.-L.Aubry, M.Tanter, M.Pernot, J.-L.Thomas, M.Fink. Experimental demonstration of noninvasive transskull adaptive focusing based on prior computed tomography scans. J.Acoust.Soc.Am.V.113 (1), pp.84-93, 2003.

13. M.Pernot, J.-F.Aubry, M.Tanter, J.-L.Thomas, M.Fink. High power transcranial beam steering for ultrasonic brain therapy. Phys.Med.Biol. V.48, pp.2577-2589, 2003.

14. S.A.Goss, L.A.Frizell, J.T.Kouzmanoff, J.M.Barich, J.M.Jang. Sparse random ultrasound phased array for focal surgery. IEEE Trans. Ultrason. Ferroelectr. Freq. Control. V.43, pp.1111-1121, 1996.

15. J.Sun, K. Hynynen. Focusing of ultarsound through a human skull. J.Acoust.Soc.Am.V.104, pp.1705-1715, 1998.

16. J.Sun, K. Hynynen. The potential of transskull ultarsound therapy and surgery using the maximum available skull surface area. J.Acoust.Soc.Am.V.105, pp.2519-2517, 1999.

17. K. Hynynen, J.Sun. Trans-skull ultrasound therapy: the feasibility of using image-derived skull thickness information to correct the phase distortion. IEEE Trans. Ultrason. Ferroelectr. Freq. Control. V.46, N6, pp. 752-755, 1999.

18. G.T.Clement, P.J.White, K. Hynynen. Enhanced ultrasound transmission through the human skull using shear mode conversion. J.Acoust.Soc.Am.V.115(3), pp.1356-1364, 2004.

19. G.T.Clement, J.Sun, T.Giesecke, K. Hynynen. A hemisphere array for no`n-invasive ultrasound brain theraphy and surgery. Phys.Med.Biol. V.45, pp.3707-3719, 2000.

20. M.Hayner, K.Hynynen. Numerical analysis of ultrasonic transmission and absorbtion of oblique plane waves through the human skull. J.Acoust.Soc.Am.V.110 (6), pp.3319-3330, 2001.

21. C.W.Connor, G.T.Clement, K. Hynynen. A unified model for the speed of sound in cranial bone based on genetic algorithm optimization. Phys.Med.Biol. V.47, pp.3925-3944, 2002.

22. G.T.Clement, P.J.White, K. Hynynen. Investigation of a large area phased array for focused ultrasound surgery through the skull. Phys.Med.Biol. V.45, pp.1071-1083, 2000.

23. M.Fink, M.Tanter, J.-L.Thomas. Overcoming the Diffraction limit a Time-Reversed Mirror and a Novel Acoustic Sink. Phys. Rev. Lett., V.89, pp 124-301, 2002.

24. V.D. Svet. Acoustical Holography. Leningrad. Rumb, 187 pp., 1976.

25. N. Cesbron. A 3-D Underwater Acoustic Camera. Underwater System Design, Vol.16, N2, March –April, 1994.

26. P.Alais. Development of underwater frontal imaging sonar. Concept of a 3-D imaging system. Acoustical Imaging, V.18, Plenum Press Santa Barbara, 1989.

27. Atlases of anatomy. Giunti Editorial Group, Florence, 2005.

28. Gerard J. Tortora. Principles of Human Anatomy. John Wiley & Sons, Inc., 2002.

29. F.J.Fry, J.E.Barger. Acoustical properties of the human skull. //JASA, 1978, V.63, N5, pp.1576-1590.

30. S.A.Gross, R.L.Johnston, F.Dunn. Comprehensive compilation of empirical ultrasonic properties of mammalian tissues. //JASA, 1978, V64, N2, pp.423-457.

31. S.A.Gross, R.L.Johnston, F.Dunn. Compilation of empirical ultrasonic properties of mammalian tissues. II . //JASA, 1980, V68, N1, pp.93-108.

32. M.R.Bailey, V.A.Khokhlova, O.A.Sapozhnikov, S.G.Kargl, and L.A.Crum. Physical Mechanisms of the Therapeutic Effect of Ultrasound. //Acoustical Physics, 2003, V.49, N4, pp.437-464.

33. R.G. Maev, E. Malyarenco, Ultrasound Imaging of Brain Structures and Blood Vessels Through thick skull bones. Report I, ONR S&T 6.1 Program Review: Stress Physiology, May 2007.

34. R.G. Maev, E. Malyarenco, Ultrasound Imaging of Brain Structures and Blood Vessels Through thick skull bones. Report II, ONR S&T 6.1 Program Review: Stress Physiology, July 2008.

35. B. A. Auld, *Acoustic Fields and Waves in Solids, Volume II,* (Krieger, Malabar, 1990), pp.1-14.

36. B. A. Auld, *Acoustic Fields and Waves in Solids, Volume II,* (Krieger, Malabar, 1990), pp.21-57.

37. J. David, N. Cheeke, *Fundamentals and applications of Ultrasonic Waves,* (CRC Press LLC, 2002), pp.77-84.

38. J. David, N. Cheeke, *Fundamentals and applications of Ultrasonic Waves,* (CRC Press LLC, 2002), pp.91-97.

39. J. David, N. Cheeke, *Fundamentals and applications of Ultrasonic Waves,* (CRC Press LLC, 2002), pp.45-74.

40. Emmanuel P. Papadakis, *Ultrasonic instruments and devices,*(Academic Press 1999), pp.62-65

Appendix A:

Image reconstruction Program ***in absence*** of the scattering medium
(As an example of the whole code)

```
N=128;
f=1700000;
c1=1500;
%ct2=2300;
%cl2=2500;
%cl3=2700;
%ct2=0.0000001;
cl2=1500;
cl3=1500;
D1=1000;
D2=1000;
D3=1000;
% D1=1000;
% D2=2500;
% D3=2700;
Z1=D1*c1;
% Zt2=D2*ct2;
Zl2=D2*cl2;
Zl3=D3*cl3;
lambda1=c1/f;
lambdal2=cl2/f;
% lambdat2=ct2/f;
lambdal3=cl3/f;
k1=2*pi/lambda1;
kl2=2*pi/lambdal2;
% kt2=2*pi/lambdat2;
kl3=2*pi/lambdal3;
UI0=0;
UR0=1;
arr_dx=lambda1/2;
arr_x=N*lambda1/2;
M=128;
z=M*lambda1;
d1=0;
d2=0;
d3=0;
% d1=lambda1/2;
% d2=8*lambda1;
% d3=20*lambda1;
Implane_dx=lambda1/2;
%xo=Implane_dx*N/2;
% theta=atan(xo/z);
layer=zeros(1,N)*pi/2;
 %layer=rand(1,N)*pi;
dx_layer=10*lambda1/2;
source_d=1;
X=zeros(300,1);
```

```
phase=zeros(300,1);
ampl=zeros(300,1);
X_arr=zeros(N,1);
ampl_arr=zeros(N,1);
phase_arr=zeros(N,1);
ampl_re1=zeros(N,1);
ampl_im1=zeros(N,1);
ampl_mn_t=zeros(N,300);

for n=1:1:N
   X_arr(n,1)=n;
end



for i=1:1:N
   xi=(i-1)*arr_dx;
      ampl_re=0;
      ampl_im=0;

  for nu=-source_d:1:source_d
      xo=(N/2+nu)*Implane_dx;



      if xi>xo
         Theta=atan((xi-xo)/z);
         x1=(z-d3)*tan(Theta);
         r1=sqrt(x1^2+(z-d3)^2);
         kr1=k1*r1;

         x2=(d3-d2)*tan(Theta);
         r2=sqrt(x2^2+(d3-d2)^2);
         kr2=k12*r2;

         x3=(d2-d1)*tan(Theta);
         r3=sqrt(x3^2+(d2-d1)^2);
         kr3=k13*r3;

         x4=(d1)*tan(Theta);
         r4=sqrt(x4^2+(d1)^2);
         kr4=k1*r4;

         xlayer=x1+xo;
         m=floor(xlayer/dx_layer);
         ph=layer(1,m+1);

         r=r1+r2+r3+r4;
         kr=kr1+kr2+kr3+kr4;
         ampl_re=ampl_re+(UR0*cos(kr+ph)-UI0*sin(kr+ph));
         ampl_im=ampl_im+(UI0*cos(kr+ph)+UR0*sin(kr+ph));
```

```
      else

         Theta=atan((xo-xi)/z);
         x1=(z-d3)*tan(Theta);
         r1=sqrt(x1^2+(z-d3)^2);
        kr1=k1*r1;

         x2=(d3-d2)*tan(Theta);
         r2=sqrt(x2^2+(d3-d2)^2);
         kr2=kl2*r2;

         x3=(d2-d1)*tan(Theta);
         r3=sqrt(x3^2+(d2-d1)^2);
         kr3=kl3*r3;

         x4=(d1)*tan(Theta);
         r4=sqrt(x4^2+(d1)^2);
         kr4=k1*r4;

         xlayer=xo-x1;
         m=floor(xlayer/dx_layer);
         %ph=layer(1,m+1);
         ph=0;
         r=r1+r2+r3+r4;
         kr=kr1+kr2+kr3+kr4;
         ampl_re=ampl_re+(UR0*cos(kr+ph)-UI0*sin(kr+ph));
         ampl_im=ampl_im+(UI0*cos(kr+ph)+UR0*sin(kr+ph));


      end
end

      phase_arr(i,1)=atan(ampl_im/ampl_re);
      %att=exp(-3400*(r2+r3)-180*r1);
      att=1;

ampl_arr(i,1)=((att*((abs(sqrt(ampl_re^2+ampl_im^2))*cos(phase_arr(i,1)))/(r*10)))^2)/(pi*
64*12);
      ampl_re1(i,1)=ampl_re;
      ampl_im1(i,1)=ampl_im;

  end




subplot(2,2,2);
max_intensity=max(ampl_arr,[],1);
plot(X_arr,ampl_arr)
%plot(X_arr,phase_arr)
title('\bf{Intensity on the Array}','fontsize',10)
```

```
xlabel(['max=',num2str(max_intensity,'%7.2e\n'),' (W/mm^2)'],'fontsize',8)

ylabel('I')
grid on;
max(ampl_arr)
axis tight;




  for nu=-source_d:1:source_d
      xo=(N/2+nu)*Implane_dx;
      z=M*lambda1;

for i=1:1:N
   xi=(i-1)*arr_dx;


      if xi>xo
         Theta=atan((xi-xo)/z);
         x1=(z-d3)*tan(Theta);
         r1=sqrt(x1^2+(z-d3)^2);
         kr1=k1*r1;

         x2=(d3-d2)*tan(Theta);
         r2=sqrt(x2^2+(d3-d2)^2);
         kr2=kl2*r2;

         x3=(d2-d1)*tan(Theta);
         r3=sqrt(x3^2+(d2-d1)^2);
         kr3=kl3*r3;

         x4=(d1)*tan(Theta);
         r4=sqrt(x4^2+(d1)^2);
         kr4=k1*r4;

         xlayer=x1+xo;
         m=floor(xlayer/dx_layer);
         ph=layer(1,m+1);

         r=r1+r2+r3+r4;
         kr=kr1+kr2+kr3+kr4;
         ampl_re=(UR0*cos(kr+ph)-UI0*sin(kr+ph));
         ampl_im=(UI0*cos(kr+ph)+UR0*sin(kr+ph));

      else

         Theta=atan((xo-xi)/z);
         x1=(z-d3)*tan(Theta);
```

```
        r1=sqrt(x1^2+(z-d3)^2);
       kr1=k1*r1;

        x2=(d3-d2)*tan(Theta);
        r2=sqrt(x2^2+(d3-d2)^2);
        kr2=kl2*r2;

        x3=(d2-d1)*tan(Theta);
        r3=sqrt(x3^2+(d2-d1)^2);
        kr3=kl3*r3;

        x4=(d1)*tan(Theta);
        r4=sqrt(x4^2+(d1)^2);
        kr4=k1*r4;

        xlayer=xo-x1;
        m=floor(xlayer/dx_layer);
        %ph=layer(1,m+1);
        ph=0;
        r=r1+r2+r3+r4;
        kr=kr1+kr2+kr3+kr4;
        ampl_re=(UR0*cos(kr+ph)-UI0*sin(kr+ph));
        ampl_im=(UI0*cos(kr+ph)+UR0*sin(kr+ph));


    end


    phase_arr(i,1)=atan(ampl_im/ampl_re);
    %att=exp(-3400*(r2+r3)-180*r1);
    att=1;

ampl_arr(i,1)=(att*((abs(sqrt(ampl_re^2+ampl_im^2))*cos(phase_arr(i,1)))/(r*1000)))^2;
    ampl_re1(i,1)=ampl_re;
    ampl_im1(i,1)=ampl_im;


end
```

```
X_implane=zeros(N,1);
%phase_implane=zeros(N,1);
%ampl_implane=zeros(N,1);
amplitude_re=0;
amplitude_im=0;
%z=22*lambda1;
ampl_mn=zeros(N,300);
phase_mn=zeros(N,300);


for n=1:1:300
   z=(1+n)*lambda1/2;


for i=1:1:N
   xi=(i-1)*Implane_dx;
   X_implane(i,1)=i;



   for j=1:1:N
      xj=(j-1)*arr_dx;
      UR_xj=ampl_re1(j,1);
      UI_xj=ampl_im1(j,1);

      if xi>xj
         Thetaij=atan((xi-xj)/z);
         x1=d1*tan(Thetaij);
         r1=sqrt(x1^2+d1^2);
         kr1=k1*r1;

         x2=(d2-d1)*tan(Thetaij);
         r2=sqrt(x2^2+(d2-d1)^2);
         kr2=kl2*r2;

         x3=(d3-d2)*tan(Thetaij);
         r3=sqrt(x3^2+(d3-d2)^2);
         kr3=kl3*r3;

         x4=(z-d3)*tan(Thetaij);
         r4=sqrt(x4^2+(z-d3)^2);
         kr4=k1*r4;

         xlayer=xj+x1+x2+x3;
   %xlayer=xi-x4;
         m=floor(xlayer/dx_layer);
         ph=layer(1,m+1);
         %ph=0;
```

```
        r=r1+r2+r3+r4;
        kr=kr1+kr2+kr3+kr4;
        att_inv=exp(3400*(r2+r3)+180*r4);
        amplitude_re=amplitude_re+(UR_xj*cos(-kr-ph)-UI_xj*sin(-kr-ph))/1;
        amplitude_im=amplitude_im+(UI_xj*cos(-kr-ph)+UR_xj*sin(-kr-ph))/1;


        %phase_implane(j,1)=phase_implane(j,1)+atan(ampl_im/ampl_re);

%ampl_implane(j,1)=phase_implane(j,1)+abs(sqrt(ampl_re^2+ampl_im^2))*cos(phase_im
plane(j,1));

    else

        Thetaij=atan((xj-xi)/z);
        x1=d1*tan(Thetaij);
        r1=sqrt(x1^2+d1^2);
        kr1=k1*r1;

        x2=(d2-d1)*tan(Thetaij);
        r2=sqrt(x2^2+(d2-d1)^2);
        kr2=kl2*r2;

        x3=(d3-d2)*tan(Thetaij);
        r3=sqrt(x3^2+(d3-d2)^2);
        kr3=kl3*r3;

        x4=(z-d3)*tan(Thetaij);
        r4=sqrt(x4^2+(z-d3)^2);
        kr4=k1*r4;

        xlayer=xj-(x1+x2+x3);
%xlayer=xi+x4;
        m=floor(xlayer/dx_layer);
        ph=layer(1,m+1);
        %ph=0;

        r=r1+r2+r3+r4;
        kr=kr1+kr2+kr3+kr4;
        %UR_xi=1;
        %UI_xi=1;
        att_inv=exp(3400*(r2+r3)+180*r4);
        amplitude_re=amplitude_re+(UR_xj*cos(-kr-ph)-UI_xj*sin(-kr-ph))/1;
        amplitude_im=amplitude_im+(UI_xj*cos(-kr-ph)+UR_xj*sin(-kr-ph))/1;

    end
  end

        phase_mn(i,n)=atan(amplitude_im/amplitude_re);
        %att_inv=exp(3400*(r2+r3)+180*r4);
```

```
ampl_mn(i,n)=(abs(sqrt(amplitude_re^2+amplitude_im^2))*cos(phase_mn(i,n)))^2;
        amplitude_re=0;
        amplitude_im=0;
end
end

   ampl_mn_t=ampl_mn_t+ampl_mn;
   end


k=max(ampl_mn_t,[],1);
l=max(k);
ampl_mn_t=ampl_mn_t/l;

%plot(X_implane,ampl_implane)
%plot(X_implane,phase_implane)
% title('Reverse Field Reconstruction on Image-Plane (no difraction, no layer)')
%xlabel('N')
%ylabel('Amplitude (dB)')
%surf(ampl_mn)

%center=[100,32,0]
%rotate(h,[0,0,1],center);

f=0;
for i=1:N
   for n=1:300
      if ampl_mn_t(i,n)>f
         f=ampl_mn_t(i,n);
         max2=n;
         max1=i;
      end
   end
end

max1;
max2;
max1_mm=max1*lambda1/2*1000;
max2_mm=max2*lambda1/2*1000;


subplot(2,2,1);
surf(ampl_mn_t);
%set(gca,'ydir','reverse')
view(2)
title('\bf{Vertical plane image}','FontSize',10)
ylabel(['max coordinates:     x=',int2str(max1-1),' pix(',num2str(max1_mm,'%7.2f'),' mm)
y=',int2str(max2+1),' pix(',num2str(max2_mm,'%7.2f'),' mm)'],'fontsize',8)
 %axis([0 200 0 128]);
axis tight;
colorbar;
view(90,90)
```

```
%axis equal


shading flat;




subplot(2,2,3);

%------%h=horizontal
%------%v=vertical

ampl_h=zeros(N,1);

for i=1:N
   ampl_h(i,1)=ampl_mn_t(i,max2);
end

plot(X_implane,ampl_h);
title('\bf{Horizontal profile}','fontsize',10)
line([0 N],[0.7 0.7],'Color','red');

for i=1:N-1
   if i<max1
     if ampl_h(i,1)<0.7 && ampl_h(i+1,1)>=0.7
       wid_1=i;
     end
   else
      if ampl_h(i,1)>=0.7 && ampl_h(i+1,1)<0.7
         wid_2=i;
      end
   end
end

width_h=wid_2-wid_1+1;
width_h_mm=width_h*lambda1/2*1000;

xlabel(['max:  x=',int2str(max1-1),'   width(0.7)=',int2str(width_h),'
pix(',num2str(width_h_mm,'%7.2f'),' mm)'],'fontsize',8)
ylabel('I')
grid on
axis tight



subplot(2,2,4);

ampl_v=zeros(300,1);

for i=1:300
```

```
   ampl_v(i,1)=ampl_mn_t(max1,i);
end

Y=ones(300,1);

for i=1:300
   Y(i,1)=i-1;
end

plot(Y,ampl_v);
title('\bf{Vertical profile}','fontsize',10)
line([0 300],[0.7 0.7],'Color','red');

for i=1:300
   if i<max2
      if ampl_v(i,1)<0.7 && ampl_v(i+1,1)>=0.7
         wid_1=i;
      end
   else
      if ampl_v(i,1)>=0.7 && ampl_v(i+1,1)<0.7
         wid_2=i;
      end
   end
end

width_v=wid_2-wid_1+1;
width_v_mm=width_v*lambda1/2*1000;

xlabel(['max:  y=',int2str(max2+1),'   width(0.7)=',int2str(width_v),'
pix(',num2str(width_v_mm,'%7.2f'),' mm)'],'fontsize',8)
ylabel('I')
grid on
axis tight
```

Vita Auctoris

Kiyanoosh Shapoori was born in 1983 in Tehran, Iran. He received his Bachelor of Science degree in Physics from the University of Tehran in 2006. After graduation he immigrated to Canada and is currently a candidate for the degree of Master of Science in Physics at the University of Windsor.